National Library of Canada
Bibliothèque nationale du Canada

Canadian Theses Service
Service des thèses canadiennes

Ottawa, Canada
K1A 0N4

## NOTICE

The quality of this microform is heavily dependent upon the quality of the original thesis submitted for microfilming. Every effort has been made to ensure the highest quality of reproduction possible.

If pages are missing, contact the university which granted the degree.

Some pages may have indistinct print especially if the original pages were typed with a poor typewriter ribbon or if the university sent us an inferior photocopy.

Reproduction in full or in part of this microform is governed by the Canadian Copyright Act, R.S.C. 1970, c. C-30, and subsequent amendments.

## AVIS

La qualité de cette microforme dépend grandement de la qualité de la thèse soumise au microfilmage. Nous avons tout fait pour assurer une qualité supérieure de reproduction.

S'il manque des pages, veuillez communiquer avec l'université qui a conféré le grade.

La qualité d'impression de certaines pages peut laisser à désirer, surtout si les pages originales ont été dactylographiées à l'aide d'un ruban usé ou si l'université nous a fait parvenir une photocopie de qualité inférieure.

La reproduction, même partielle, de cette microforme est soumise à la Loi canadienne sur le droit d'auteur, SRC 1970, c. C-30, et ses amendements subséquents.

NL-339 (r. 88/04) c

Canada

UNIVERSITY OF ALBERTA

# THIN FILM MICROSTRUCTURE EFFECTS IN VLSI METALLIZATION

by

R. Niall Tait

A thesis submitted to the Faculty of Graduate Studies and Research in partial fulfillment of the requirements for the degree of Doctor of Philosophy.

Department of Electrical Engineering

Edmonton, Alberta

Spring, 1992

National Library of Canada
Bibliothèque nationale du Canada

Canadian Theses Service
Service des thèses canadiennes

Ottawa, Canada
K1A 0N4

The author has granted an irrevocable non-exclusive licence allowing the National Library of Canada to reproduce, loan, distribute or sell copies of his/her thesis by any means and in any form or format, making this thesis available to interested persons.

L'auteur a accordé une licence irrévocable et non exclusive permettant à la Bibliothèque nationale du Canada de reproduire, prêter, distribuer ou vendre des copies de sa thèse de quelque manière et sous quelque forme que ce soit pour mettre des exemplaires de cette thèse à la disposition des personnes intéressées.

The author retains ownership of the copyright in his/her thesis. Neither the thesis nor substantial extracts from it may be printed or otherwise reproduced without his/her permission.

L'auteur conserve la propriété du droit d'auteur qui protège sa thèse. Ni la thèse ni des extraits substantiels de celle-ci ne doivent être imprimés ou autrement reproduits sans son autorisation.

ISBN 0-315-73042-0

Canada

UNIVERSITY OF ALBERTA

RELEASE FORM

NAME OF AUTHOR: **Robert Niall Tait**

TITLE OF THESIS: **Thin Film Microstructure Effects in VLSI Metallization**

DEGREE: **Doctor of Philosophy**

YEAR THIS DEGREE GRANTED: **1992**

Permission is hereby granted to the University of Alberta Library to reproduce single copies of this thesis and to lend or sell such copies for private, scholarly or scientific research purposes only.

The author reserves all other publication and other rights in association with the copyright in the thesis, and except as hereinbefore provided neither the thesis nor any substantial portion thereof may be printed or otherwise reproduced in any material form whatever without the author's prior written permission.

(SIGNED) .....R.N.Tait.....

PERMANENT ADDRESS:

11651 - 73 Ave.

Edmonton, Alberta

T6G 0E3

DATED ...March 23..... 19.92

THE UNIVERSITY OF ALBERTA

FACULTY OF GRADUATE STUDIES AND RESEARCH

The undersigned certify that they have read, and recommend to the Faculty of Graduate Studies and Research for acceptance, a thesis entitled **Thin Film Microstructure Effects in VLSI Metallization** submitted by **Robert Niall Tait** in partial fulfillment of the requirements for the degree of **Doctor of Philosophy**.

.....

Dr. M.J. Brett, Supervisor

.....

Dr. R.P.W. Lawson

.....

Dr. C.E. Capjack

.....

Dr. A.M. Robinson

.....

Dr. E.P. Lozowski

.....

Prof. A.R. Neureuther
Dept. EECS, Univ. of Calif., Berkeley

Date ..... March 3 1992 .....

## Abstract

The use of thin film technology continues to grow in many areas of manufacturing. With this growth has come the realization that an understanding of film microstructure is essential to predicting the optical, magnetic and electrical characteristics of films. This thesis is concerned with the microstructure observed in thin metal films produced by evaporation or sputtering, and the effects this structure can have on performance and failure of metallization layers. SIMBAD, a ballistic deposition model of thin film growth is presented and is applied to the simulation of thin films for metallization applications. A brief survey of approaches to thin film modeling is presented, followed by a description of how ballistic deposition accurately reproduces the essential properties of thin film microstructure. A derivation of the expected functional form for column structure angle as a function of deposition angle is used to show the shortcomings of the empirically derived tangent rule, and an explanation of structural anisotropy in the film plane is given based on a 3-D ballistic deposition simulation. Most importantly, films deposited over topography are studied, and the predictions of density variation provided by simulations are verified through measurements of density and etch rate for these films. Finally, the potential for expansion of SIMBAD to model a variety of processes is demonstrated by modeling the plasma etching process.

## Acknowledgement

Sincere thanks are due to my supervisor, Dr. M.J. Brett, for his direction and encouragement throughout the course of this work. His talent for knowing when and how hard to push a student to get a job done was especially valuable.

Other people working on the SIMBAD project deserve recognition. Tom Smy and Steve Dew have provided a wealth of ideas, and solved many programming problems more quickly and elegantly than I possibly could.

There are a number of people who have provided valuable input into the project. George Braybrook deserves recognition for providing the outstanding photographs which are so critical to this thesis. Ken Westra's comments and experimental advice were greatly appreciated. Dr. E.P. Lozowski must be acknowledged as the driving force behind the hailstone simulation work, and for his service on the examining committee. The students and staff of the Materials and Devices Lab all deserve mention, but in particular Alan Mitchell, Glen Fitzpatrick, and Graham MacKinnon have been indispensible in aiding and advising on experimental work in the lab. Finally, the financial support of the Alberta Microelectronic Centre is gratefully acknowledged.

## Table of Contents


Chapter 1: Introduction ..... 1

1.1 Metallization ..... 1
1.1.1 Evaporation ..... 3
1.1.2 Sputtering ..... 4
1.1.3 Chemical Vapour Deposition ..... 4

1.2 Thin Film Microstructure ..... 6

1.3 Thin Film Modeling ..... 10

Chapter 2: Modeling and SIMBAD ..... 11

2.1 Topography Simulation ..... 11

2.2 Continuum Models ..... 11

2.3 Molecular Dynamics ..... 12

2.4 Ballistic Aggregation ..... 13

2.5 SIMBAD ..... 14
2.5.1 Simulation Basics ..... 14
2.5.2 Simulation Algorithm ..... 17

2.6 Simulation and Reality ..... 18

Chapter 3: Simulating Basic Film Properties ..... 22

3.1 Film Structure and Density ..... 22

3.2 Column Angles ..... 25
3.2.1 Column Angle Theory ..... 25
3.2.1.1 Films with No Relaxation ..... 26
3.2.1.2 Films with Relaxation ..... 29
3.2.1.3 Column Spacing $a$ ..... 30
3.2.1.4 Results ..... 31

3.3 Dimensionality ..... 32

3.4 Column Anisotropy ..... 36
3.4.1 Anisotropy in Sputtered Titanium ..... 36
3.4.2 Anisotropy Results ..... 38

3.5 Conclusions ..... 42

Chapter 4: Deposition over Topography ..... 43
4.1 Evaporated Films ..... 43
4.1.1 Film Structure ..... 43
4.1.2 Film Density ..... 45
4.2 Sputtered Films ..... 48
4.2.1 Film Deposition and Etching ..... 48
4.2.2 Film Structure and Density ..... 50

Chapter 5: Etching ..... 53
5.1 Wet Etching ..... 53
5.1.1 Density Measurements ..... 53
5.1.2 Etch Rate Measurements ..... 56
5.1.2 Simulation Results ..... 59
5.2 Plasma Etching ..... 61
5.2.1 Experimental Work ..... 62
5.2.2 Simulation ..... 63
5.2.3 Results and Discussion ..... 65

Chapter 6: Conclusions ..... 68
6.1 Application ..... 68
6.2 Originality ..... 68
6.3 Future Work ..... 69

References ..... 71

Appendix 1: SIMBAD rec4 ..... 79
A1.1 Use of rec4 ..... 79
A1.2 The rec4 Program ..... 81

Appendix 2: 3-D Simulation ..... 82
A2.1 Use of the 3-D Program ..... 82
A2.2 The 3-D Algorithm ..... 83
A2.3 Program Listing ..... 85

Appendix 3: Optical Coatings....98
A3.1 Evaporated Films....98
A3.2 Sputtered Films....100
A3.3 Applications....102
A3.4 Conclusion....104

Appendix 4: Nodule Growth....105
A4.1 Nodule growth....105
A4.2 Results....105

Appendix 5: Simulating Giant Hailstone Structure....109
A5.1 Hailstone Growth with SIMBAD....109

# List of Tables

Chapter 1: Introduction ..... 1
Table 1.1 Desired properties of metallization materials..... 2
Table 1.2 Characteristics of evaporation and sputtering ..... 5

## List of Figures


Chapter 1: Introduction ..... 1
Figure 1.1 Problems in metallization. ..... 3
Figure 1.2 A sputtering system. ..... 5
Figure 1.3 Sputtered Mo film exhibiting columnar microstructure. ..... 7
Figure 1.4 The tangent rule with experimental data. ..... 7
Figure 1.5 Structure zone models. ..... 9

Chapter 2: Modelling and SIMBAD ..... 11
Figure 2.1 Feature resolution and simulation dimensions for film growth models. ..... 16
Figure 2.2 Deposition and relaxation model used in SIMBAD ..... 16
Figure 2.3 Interaction range in film deposition. ..... 18
Figure 2.4 Evidence of the fractal nature of film microstructure. ..... 19

Chapter 3: Simulating Basic Film Properties ..... 22
Figure 3.1 Change in column structure with increasing diffusion distance ..... 23
Figure 3.2 Density variation with deposition angle for evaporation simulations. ..... 24
Figure 3.3 Density variation with deposition angle for sputtering simulations. ..... 24
Figure 3.4 Experimental density variation with deposition angle ..... 25
Figure 3.5 Geometry of the column growth problem. ..... 27
Figure 3.6 Growth with shadowing due to both neighbors ..... 27
Figure 3.7 Growth with shadowing from one neighbor. ..... 29
Figure 3.8 Determining column spacing $a$ ..... 30
Figure 3.9 Column spacing from simulations and theory. ..... 31
Figure 3.10 Simulated, experimental and theoretical column angles. ..... 32
Figure 3.11 Simulated density variation with deposition angle for 2-D and 3-D models. ..... 34
Figure 3.12 Density plot of a film deposited over a trench using a 3-D on-lattice simulation ..... 34
Figure 3.13 Density plots of films deposited over trenches using the 2-D off-lattice simulation (top), and the 2-D on-lattice simulation. ..... 35
Figure 3.14 Anisotropies in film microstructure. ..... 37
Figure 3.15 Film plane anisotropy in sputtered Ti. ..... 39
Figure 3.16 Film plane anisotropy simulations ..... 40
Figure 3.17 Column shape measurements. ..... 41

Chapter 4: Deposition over Topography ..... 43
Figure 4.1 $MgF_2$ evaporated at 5° onto an oxide line ..... 44
Figure 4.2 $MgF_2$ evaporated at 40° onto an oxide line ..... 44
Figure 4.3 SIMBAD simulation of a film evaporated at 5° ..... 46
Figure 4.4 SIMBAD simulation of a film evaporated at 40° ..... 47
Figure 4.5 Confirmation of density predictions in sputtered Mo. ..... 49
Figure 4.6 SIMBAD simulation and density plot of a sputtered film ..... 51

Chapter 5: Etching ..... 53
Figure 5.1 Density of sputtered tungsten ..... 55
Figure 5.2 Resistivity of sputtered tungsten ..... 55
Figure 5.3 Etch rate for obliquely deposited W in $K_3Fe(CN)_6$ and NaOH ..... 57
Figure 5.4 Wet etching of W deposited over a trench. ..... 58
Figure 5.5 Angular distribution used for sputtering simulations ..... 59
Figure 5.6 SIMBAD simulation of deposition and wet etching of sputtered W ..... 60
Figure 5.7 Plasma etching of W deposited over a trench. ..... 64
Figure 5.8 Plasma etching simulation of W deposited over a trench. ..... 66
Figure 5.9 Effect of reaction coefficient on etch rates. ..... 67

Chapter 6: Conclusions ..... 68

References ..... 71

Appendix 1: SIMBAD rec4 ..... 79
Figure A1.1 The simulation grid ..... 81

Appendix 2: 3-D Simulation ..... 82
Figure A2.1 The array used for the 3-D simulation. ..... 84

Appendix 3: Optical Coatings ..... 98
Figure A3.1 Density of evaporated $MgF_2$ films ..... 99
Figure A3.2 Refractive index of evaporated $MgF_2$ films. ..... 99
Figure A3.3 Refractive index vs. density for evaporated $MgF_2$ films. ..... 101
Figure A3.4 Refractive index vs. density for sputtered $SiO_2$ films. ..... 101
Figure A3.5 SIMBAD simulation and density plot of sputtered $SiO_2$ for a waveguide detector coupler. ..... 103

Appendix 4: Nodule Growth ..... 105
Figure A4.1 Nodule in $MgF_2$ with no seed visible. ..... 106
Figure A4.2 A nodular defect in $MgF_2$ with a visible seed. ..... 106
Figure A4.3 Fracture in a $MgF_2$ film containing nodular defects. ..... 108

Figure A4.4 SIMBAD density profile of a nodular defect.....108

Appendix 5: Simulating Giant Hailstone Structure.....109
Figure A5.1 Simulation of giant hailstone. .....110
Figure A5.2 Section of a giant hailstone.....110

## List of Symbols

| | |
|---|---|
| VLSI | Very Large Scale Integration |
| RF | Radio Frequency |
| DC | Direct Current |
| 2-D | Two Dimensional |
| 3-D | Three Dimensional |
| CVD | Chemical Vapour Deposition |
| LPCVD | Low Pressure CVD |
| SEM | Scanning Electron Microscope |
| TEM | Transmission Electron Microscope |
| $\alpha$ | Angle of Deposition Flux |
| $\beta$ | Column Angle |
| $T_m$ | Melting Temperature of Film Material |
| $T_s$ | Substrate Temperature |
| $\rho$ | Average Density |
| $\rho(x,y)$ | Local Density |
| $R_a$ | Radius of Particles in Case a |
| $r_a$ | Separation of Particles in Case a |
| $N_a$ | Number of Atoms in a Particle in Case a |
| M | Mass of a Particle |
| $\frac{\rho N_a}{M}$ | Number Density |
| $V_{1a}$ | Volume |
| $\Phi_a$ | Potential Energy |
| $f$ | Scale Factor |
| $\gamma_1, \gamma_2$ | Angles Defining Flux Region |
| d | Disc Diameter |
| a | Disc Spacing |

| | |
|---|---|
| $b$ | $\frac{1}{2}$ Width of Flux Region |
| $D$ | Capture Diameter |
| $\delta$ | Disc Diameter for Films With Relaxation |
| $d$ | Diffusion Length |
| $\rho(t)$ | Density at Time t |
| $\rho_o$ | Density at Time 0 |
| $c$ | Etch Constant |
| $r$ | Etch Rate |
| $i,j$ | Location Indices |
| $k$ | Time Index |
| $n_f$ | Film Refractive Index |
| $n_v$ | Void Refractive Index |
| $n_b$ | Bulk Refractive Index |
| $p$ | Packing Fraction |

# Chapter 1: Introduction

The technique of thin film fabrication by condensation of vapour onto a surface has been used for over a century.[1] Since that time thin films have grown steadily in technological importance. For most of that period the main application was in optical coatings,[2] but in the last 30 years the rapid development and miniaturization of integrated electronics has been stimulating interest in improving thin film technology.[3,4]

The utility of films for microelectronics is due to their high purity and the possibility of forming very fine pattern features using photolithography and etching. These films are used for conducting regions within the device, for electrical insulation, and for protection from the environment. The deposition process used must be safe, reproducible, and inexpensive, and must generate films with uniform properties over each device and over all wafers processed. To accomplish this the film structure must be controlled and reproducible.

It is now known that the microstructure produced during the condensation of material from vapour strongly modifies the properties of thin films from those of the bulk material.[4,5] For deposition onto substrates at a temperature well below the melting point of the film material, the solidification process occurs far from equilibrium. The nonequilibrium conditions are manifested in residual stress and the incorporation of impurities and voids. The porous, voided structure is ubiquitous in vapour-deposited thin films, appearing in metallic, semiconducting, and insulating thin films of crystalline and amorphous materials.[6]

The structure, generally referred to as columnar, shows common features in all films and influences film properties in every instance. Because of this, an understanding of formation of columnar structure is essential to development of microelectronics technology. This is particularly true as device sizes move into the sub-micron region, and the microstructure dimension becomes significant relative to the feature size and begins to affect device performance.[7] A reasonably fast and inexpensive method for studying microstructure in films on geometries used in integrated circuit design is through the use of computer simulation of thin film growth. A model which reproduces the salient microstructural features observed in real films, yet is simple and efficient, must be chosen and verified.

## 1.1 Metallization

Several applications of thin films in microelectronics have been mentioned. Metallization, the process of forming connections between devices in an integrated circuit, will be the focus of this study. There are many material properties required of interconnect systems,[8] and these are outlined in Table 1.1. Most of these are self explanatory, but a couple deserve further comment.

Electromigration is the movement of lead material in the direction of electron flow due to momentum transfer from electrons to metal ions.[9-11] It is found to occur when current density is very high ($10^5$ - $10^6$ A/cm$^2$), which is often the case in IC

Table 1.1. Desired properties of metallization materials

1. Low resistivity
2. Easy to form
3. Easy to etch for pattern generation
4. Stable in oxidizing ambients
5. Mechanically stable; good adherence, low stress
6. Smooth surface
7. Stable throughout processing, including high temperature sintering, dry or wet oxidation, passivation, and metallization
8. No reaction with other materials
9. No contamination of devices or apparatus
10. Good device characteristics and lifetimes
11 Low contact resistance
12 Low electromigration

leads. The effect is reduced by addition of small amounts of another metal, such as 1-2% copper in aluminum leads. The movement of material can result in the growth of hillocks rising above the rest of the metal surface. Also caused by stress relaxation, they can grow to the point of puncturing interlevel insulation. Another threat to insulation is the reaction of the metal with silicon or silicon dioxide. Aluminum forms an alloy with silicon, and as a result aluminum spikes can form which may penetrate insulation or junctions.[12] This problem can be partially remedied by adding a small percentage of silicon to aluminum interconnects, or by using a barrier layer. A section of a device is shown in Figure 1.1 to illustrate the geometry and some of the problems mentioned here. All these problems are aggravated by the trend towards higher device density, closer spacing, narrower leads, and shallower junctions. There are also metallization problems independent of material properties, which will be outlined here.

As circuits become more complex, large portions of surface area must be devoted to interconnection, and in many cases this becomes the limiting factor in determining chip size. Lead routing becomes complicated, and multilevel interconnection becomes necessary. As layers of metal and insulator are built up, surface contours become more uneven. Planarization processes have been developed which maintain a more even surface by filling holes, but these are generally multi step processes which seldom completely planarize the surface.[13] As a result films must often be deposited over topography varying from gentle slopes, to overhangs which are virtually impossible to cover. Usually steps with sharp angle sidewalls are used to minimize area. A conformal covering is important to device reliability, so step coverage is often quoted as a measure of metallization quality.[14] Step coverage is defined as the ratio of film thickness on a step sidewall to thickness at the top of the step. For most metallization processes, the metal surface evolution is determined by

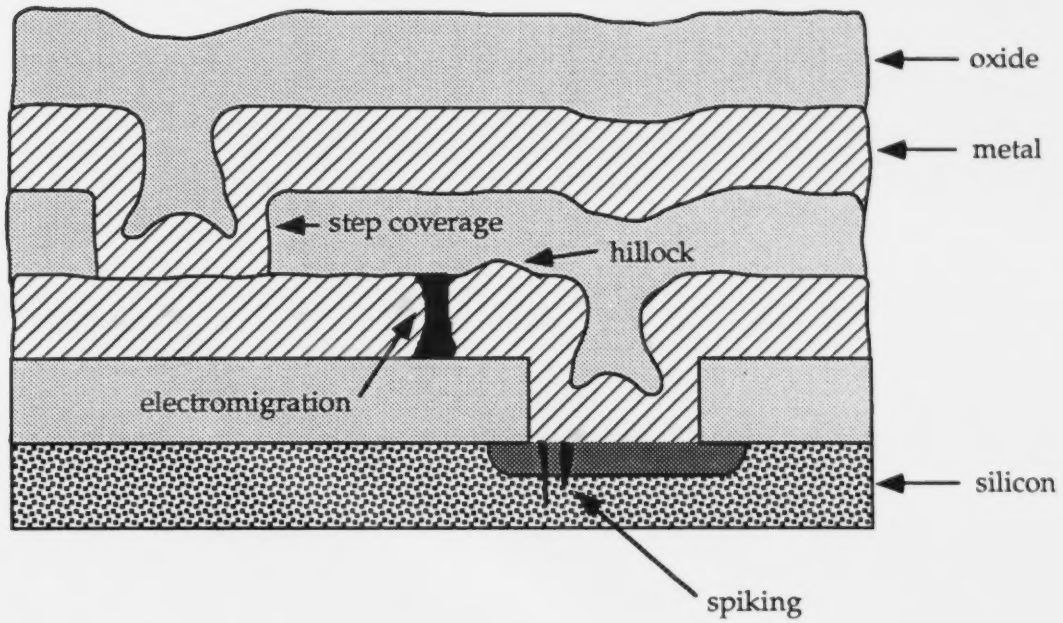


Figure 1.1. Problems in metallization.

geometrical shadowing of material from the deposition source, but this work will show that the surface evolution is not the only quantity of interest when determining the quality of interconnects. The significance of the internal microstructure of metallization films due to commonly used materials, deposition processes, and geometries will be shown in this thesis.

Aluminum is the most common material for low resistance contacts and interconnects. It has high conductivity, makes good contact to silicon, is easy to evaporate or sputter, and adheres well to silicon dioxide. However, it exhibits only modest resistance to electromigration and tends to grow spikes which puncture interlevel oxide and doped wells. These drawbacks have led to the use of gold, platinum, titanium, molybdenum, tungsten, tungsten-titanium alloys, and palladium. Also, polysilicon and refractory metal silicides are used for gate and interconnect metallization.[7] Columnar microstructure is observed in all these materials, particularly in the refractory metals due to their high melting point. The columnar growth is encouraged by the low temperature deposition processes most commonly used.[15]

### 1.1.1 Evaporation

Evaporation is the oldest and simplest deposition process.[18] The vacuum equipment is essentially the same for evaporating any material, but there are several evaporant sources available. One method applicable to metals only uses a filament heater. A wire of the metal to be deposited is wrapped around the filament, and as it heats the metal wets the filament surface and evaporates. The filament material must

obviously have a higher melting temperature than the evaporant, and must not alloy with it. A simple variation is to use a filament in the form of a boat which allows the use of powder or chunk material and does not require wetting. Neither of these sources holds sufficient material to allow sequential evaporations in a system without breaking vacuum to replenish the supply of evaporant. Also, filaments have a limited life. A source which avoids these problems uses large water-cooled crucibles heated in a small region by an electron beam. Inductively-heated crucibles are occasionally used for electrically conducting evaporants.

For multiple-component films, such as aluminum with a small amount of copper or silicon, evaporation becomes very difficult. Different vapour pressures for the materials requires the use of separate sources with independently controlled deposition rates. Sputtering from a target of the desired alloy is more commonly used.

### 1.1.2 Sputtering

Sputtering is a fundamentally different process from evaporation, although the results can be very similar. A comparison of the two processes is provided in Table 1.2. In sputtering the source of coating material, usually referred to as the target, is placed in a vacuum chamber. A glow discharge is ignited above the target in a low pressure (1-100 mTorr) atmosphere usually of a heavy inert gas such as argon. With a negative bias on the target, ions bombard the surface and cause ejection of target material due to momentum transfer. The ejected material forms a film on a nearby substrate. A variety of geometries can be used, but the planar magnetron using confinement of the plasma by a magnetic field is now the most common. The equipment is shown schematically in Figure 1.2.

Alloys of materials such as Al/Cu, Al/Cu/Si, or Ti/W are usually deposited by sputtering.[20] The target must be of high purity and uniform composition to produce consistent high quality films. Pure metals are easily obtained, but alloys and brittle materials are more difficult to produce. An advantage of sputtering over other deposition processes is that virtually any material can be used. Metals, even low vapour pressure, high melting point ones such as Mo, W, or Pt, are easily deposited. Insulators require sputtering with an RF plasma. Some compounds can be formed by introducing a reactive gas into the vacuum chamber.[19] Sputtering also provides superior step coverage when compared to evaporation.[20,21] Evaporated material comes from a small source, and as a result step sidewalls present a small area to the source and receive less material flux than horizontal sections. The more distributed source and scattering of material deposited by sputtering result in more uniform coverage. However, the higher working pressure can also result in film contamination, and this prevented the use of sputtering for metallization until systems were improved.[20]

### 1.1.3 Chemical Vapour Deposition

Chemical vapour deposition (CVD) provides better coverage than either sputtering or evaporation.[20] However, although CVD of many metals is possible, its application to semiconductor processing is fairly recent.[22,23] The process involves introduction of the desired film material to the deposition chamber in the form of gaseous compounds. A chemical reaction is stimulated by heat or a plasma, with the

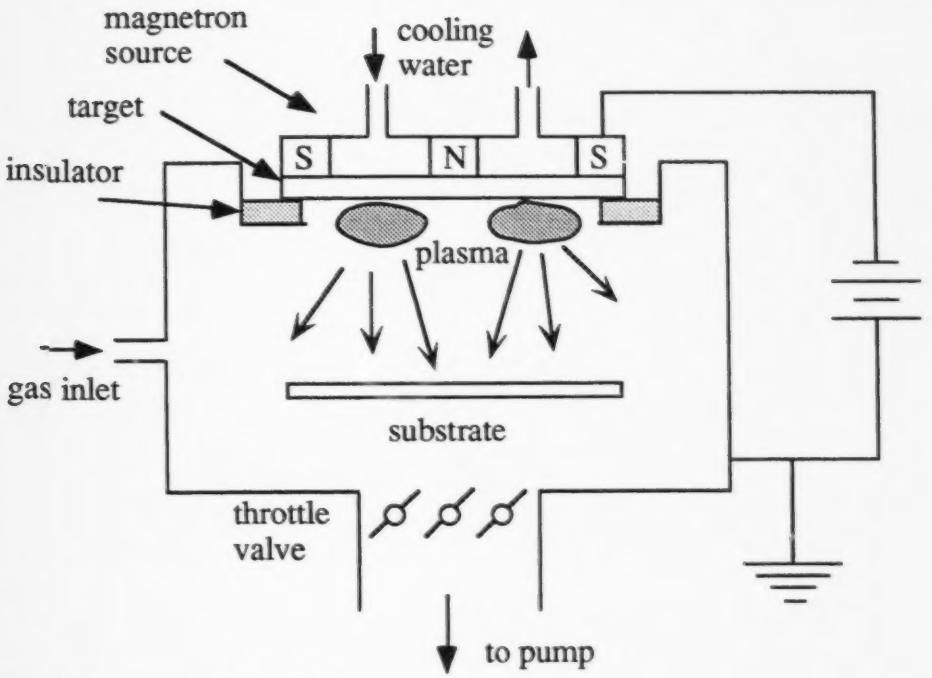


Figure 1.2. A sputtering system.

Table 1.2. Characteristics of evaporation and sputtering

| EVAPORATION | SPUTTERING |
|---|---|
| **1. Vapour production** | |
| thermal | ion bombardment with momentum transfer |
| low kinetic energy (~0.1eV) | high kinetic energy (1-40 eV) |
| few or no charged particles produced | positive and negative ions as well as reflected primary ions produced |
| **2. Vapour transport** | |
| high or ultra-high vacuum | high working gas pressures (1-100 mTorr) |
| few collisions (mean free path » source-substrate distance) | collisions affect energy and angular distributions |
| **3. Condensation** | |
| surfaces are unaffected by incident atoms | ions and energetic neutrals strongly influence surface |
| low residual gas incorporation | working gas can be included in films |

substrate acting as a catalytic surface. Most metals of interest for metallization can be deposited using this technique, but frequently the deposition temperature is too high to be useful, adhesion is poor, or the film is not of satisfactory electrical or surface quality.[20] The two most frequently studied materials are aluminum and tungsten, both using low pressure systems at a few hundred degrees Centigrade. A rough surface and the lack of a process to co-deposit copper or another electromigration-resistant material have inhibited commercial usage of the aluminum low pressure CVD (LPCVD) process. High quality tungsten layers are easily produced, although secondary reactions result in high resistance contacts.

All three of these deposition processes result in some form of film microstructure, although the structure in evaporated and sputtered films tends to be more pronounced due to the low processing temperatures and fairly low pressures. For large features and planar films the microstructure is not a problem, but for linewidths or topographies small enough that the microstructure scale is significant relative to the feature size, the columnar structure can seriously affect film properties.

## 1.2 Thin Film Microstructure

The columnar microstructure being discussed is generally considered to be a manifestation of the nonequilibrium conditions under which condensation of a film occurs. For a vapour-deposited film, the condensation rate is much greater than the evaporation rate at the substrate. In comparison, for the freezing of liquid to form a solid the freezing and melting rates are nearly identical unless the liquid is supercooled. It is the low diffusion distances associated with the rapid condensation that is responsible for the existence of the microstructure.[5]

The structure consists of a network of low density material that surrounds an array of parallel columnar regions of higher density material. There have been many reports of this structure in the past 30 years, with observations made by scanning (SEM) and transmission (TEM) electron microscopy, and by small angle electron and X ray scattering.[24] The effect of the microstructure has been observed in magnetic, optical, electrical, and mechanical properties of films.[25,26] Characteristic structure is clearly shown in Figure 1.3, an SEM micrograph of a thick molybdenum film sputtered over a line of silicon dioxide. The columns are uniform, extending through the entire thickness of the film. Their orientation is determined by the angle of incidence of the vapour flux, but is not equal to that angle.

The effect of vapour incidence angle upon the column angle is generally expressed in terms of the tangent rule. Determined experimentally for evaporated aluminum,[4] the rule relates the angle $\beta$ between the columns and the substrate normal to the angle $\alpha$ between the vapour flux and the substrate normal, by the expression

$$2 \tan \beta = \tan \alpha \qquad 1.1$$

This states that the columns are oriented closer to the substrate normal than the vapour flux. The angle of incidence effect provides a quantitative test for possible microstructure formation mechanisms. It has proven accurate for many materials evaporated at low substrate temperatures, but it is certainly not universally applicable. Very little data agrees at deposition angles above about 60 °, and agreement becomes worse as substrate temperatures are increased.[29,30] Column angle data from an assortment of sources is shown in Figure 1.4.

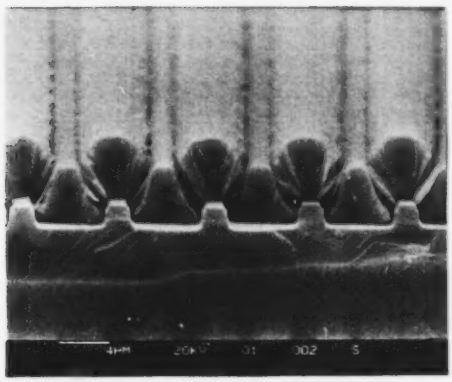

Figure 1.3. Sputtered Mo film exhibiting columnar microstructure.

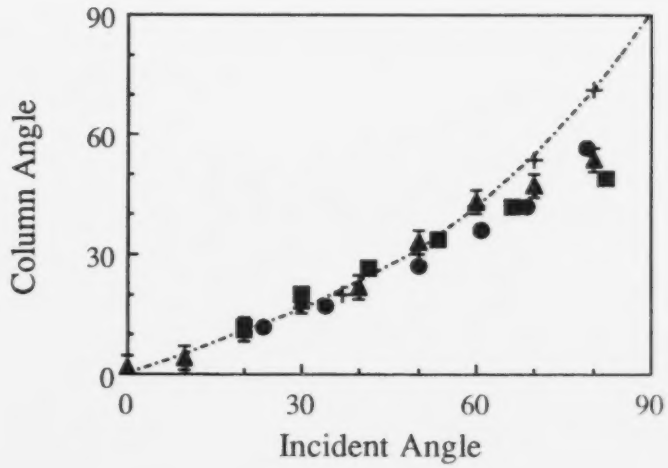


Figure 1.4. The tangent rule with experimental data. ▲ $MgF_2$ measured, + Al ref. 4, ● Al ref. 107, ■ Ge ref. 107.

Increasing substrate temperature increases the diffusion of deposited atoms, and will eventually eliminate not just the angular dependence of the column growth, but the existence of column structure as well. Column formation is observed most readily in high melting point elements, compounds of high binding energy, and easily-oxidized metals in the presence of oxygen. This indicates that the growth of columns is related to low diffusion distance of deposited atoms, although the precise dependence is not known.

The relationship between substrate temperature and diffusion distance has been used to qualitatively classify microstructure. A scheme known as the Structure Zone Model was developed by Movchan and Demchisin to identify three distinct microstructure types based on substrate temperature.[6] Normally temperature is given in terms of the ratio $T_s/T_m$ where $T_s$ is the substrate temperature and $T_m$ is the melting temperature of the film material, and is sometimes referred to as the reduced temperature. This model was developed through studies of a number of evaporated materials. For evaporation at substrate temperatures below about 30% of the melting temperature of the film material, the microstructure is controlled by low diffusion rates and self-shadowing. This leads to an open, porous column structure, and it is classified as zone 1. At substrate temperatures between about 30 and 45% of $T_m$, the structure is more dense due to increased surface and grain boundary diffusion, which overcome the shadowing effects. This zone 2 structure is still columnar, but the voids between columns are small. At even higher temperatures, zone 3 growth is observed. In this region bulk diffusion and grain growth occurs, resulting in a film consisting of symmetric rather than columnar grains.

Of course columnar structure also occurs in sputtered films, but due to the larger number of parameters it is more difficult to classify. Thornton took the descriptive model used for evaporation, and extended it to include the effect of the working gas pressure.[15-17] The pressure affects scattering of both film material vapour and neutral gas atoms, moderating energy and affecting diffusion of deposited material. The most significant change from the evaporation model is the addition of zone T, an intermediate structure between zone 1 and 2 and consisting of a dense array of fibrous grains. The structure is attributed to the atomic peening effect of energetic neutral gas atoms. The models for both evaporation and sputtering are shown in Figure 1.5.

These models identify shadowing and diffusion as universal factors in the formation of film microstructure. There are clearly other material and process-dependent factors. Diffusion distance is very difficult to measure, but it will be related to binding energy or diffusion energy and impurity content. Shadowing will be determined by the surface morphology and the angular distribution of incident material. For evaporation, this is a fixed angle, since the source is small and the pressure low. For sputtering, scattering and a more distributed source can lead to a number of possible distributions. At pressures commonly used for these processes the distribution is determined mainly by the geometry of the target substrate system. Although all these effects have been identified as contributing factors in microstructure formation, the exact influence of each one is unknown. Because of this, modeling of the film growth process is very instructive in understanding the film structure.

a)

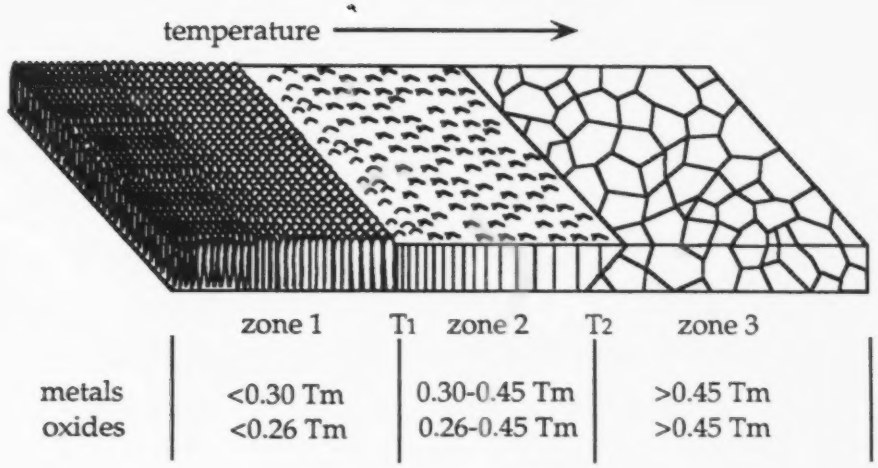


b)

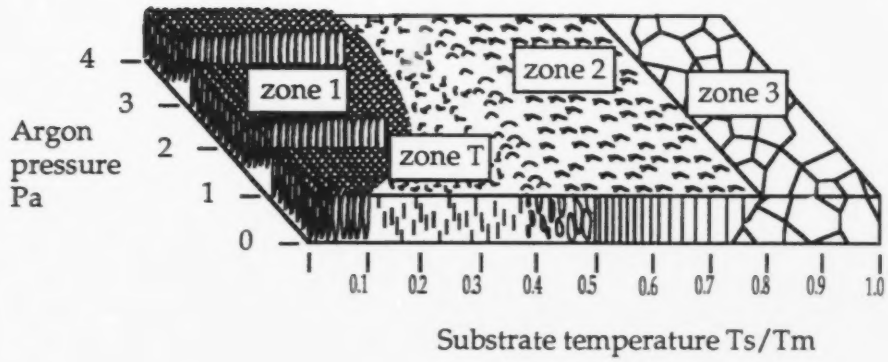


Figure 1.5. Structure zone models proposed by a) Movchan and Demchishin and b) Thornton.

## 1.3 Thin Film Modeling

Modeling of film growth can provide a quick and economical method of investigating the effects of deposition parameters and geometries on film characteristics. Due to the technological importance and the interesting structural formations of thin films, a number of approaches to modeling the growth process have been suggested. These will be thoroughly covered in the next chapter. Before considering the possible models, it is necessary to define a working philosophy which identifies the desirable and achievable characteristics for a metallization simulation.

This application will be concerned mainly with the behavior of metal films deposited over steps and vias. Metal leads on flat substrates are not immune to microstructure problems, particularly as line widths approach the grain size in many films. However, it is the structure of films used in interconnects and contacts between levels that will be studied here. The important microstructure-determining parameters have been experimentally determined, as mentioned above. Clearly a reasonable model will include these parameters.

The question that remains concerns the choice of observable characteristics which can be used to measure the success of the model. The simplest test is the qualitative appearance of the film, but more quantitative observations are desirable. Step coverage has been used as a measure of interconnect quality, but it is independent of microstructure. As previously mentioned, the behaviour of the column structure as a function of the angle of incidence of the film material is a good test for proposed models. Electrical and optical properties are easily measured quantities that should also provide tests for a model, but they are indirect tests. The characteristic of a film most directly related to the column structure is the density, sometimes referred to as the void fraction. This can then be related to other measurable quantities empirically or by simple theoretical considerations.[29,31]

In order to quickly identify metallization problems for films deposited over topography by physical vapour deposition, a modeling technique will be chosen which minimizes computational requirements, yet incorporates essential microstructure-determining parameters. Results will be verified by observations of step coverage, microstructure, and density.

# Chapter 2: Modeling and SIMBAD

There are a number of approaches to the simulation of thin film growth, from which the most appropriate for this application must be chosen. These range from efficient models which have a limited set of parameters, to remarkably complicated and computation-intensive approaches which include parameters which are of minor importance in determining the general features of column structure. Since this work is aimed at metallization simulation, it will begin by describing the existing process simulation model. The requirement that microstructure be represented suggests a number of techniques that could be applied to a new metallization model. The advantages of each will be considered.

## 2.1 Topography Simulation

Process simulation of IC fabrication technology is often used to rapidly and economically explore process effects. There are many two dimensional (2-D) topography simulators which generate the time evolution of the surface profile. Among the first of these, and still pre-eminent is SAMPLE. This program is widely available from The University of California at Berkeley, and extensive development has made it highly successful in simulating not only film deposition, but also lithography, etching and thermal processing.[32-34] Recently SAMPLE-3D has been developed for full three dimensional (3-D) simulation of etching and deposition.[35] Most of the other simulators, including SPEEDIE[36] and DEPICT,[37] use variations and improvements on the basic algorithms used in the original SAMPLE. These programs and others like them are frequently referred to as string advancement algorithms, and they currently dominate the field of topography simulation.

This type of simulation represents a surface as a series of short segments. The calculation considers a series of points, each representing the center of a segment. For deposition, the position of each point evolves according to a calculation of the flux reaching that segment. At any time the surface can be reconstructed from the position of the points, but only the surface profile or step coverage is determined. Such a model includes shadowing effects due to the surface topography only, but assumes an otherwise homogeneous film. SAMPLE-3D can allow for variable film density based on the angle between the substrate and the vapour flux,[35] but to include complete microstructure effects an alternative model must be chosen.

## 2.2 Continuum Models

A number of models for the formation of columnar structure in thin films have been developed based on a continuum approach.[38-43] These models ignore atomic scale effects, justified by the disparate length scales of columnar structure and lattice spacing. For all but the thinnest films the column diameter is several hundred atomic diameters. In general the models calculate surface evolution based on conservation of material from deposition and surface diffusion. The initial surface must have some

irregularity. Local shadowing is then accounted for in the algorithm, and the irregularities grow to form columns as the surface evolves.

These models are attractive due to their elegance and computational efficiency. Deposition conditions are controlled by defining equation constants and an incident flux distribution. Because of the speed of the calculation, large regions can be simulated on a macroscopic scale, averaging out the detailed motion of individual atoms. A simulation space several micrometers on a side is necessary to model a structure which would typically be used for metallization , and continuum models can easily accommodate this.

Unfortunately, the deterministic approach which makes these models efficient has some drawbacks. The nucleation and growth of a thin film is generally conceptualized as a stochastic atomistic process. The fact that columnar microstructure is observed in films on substrates smooth down to an atomic scale indicates that the dependence of continuum microstructure models on initial surface irregularities is a crude representation. An obvious conclusion is that these models provide an adequate representation of film growth, but they do not provide an acceptable approach to film nucleation, the initial critical stages of growth. Monte Carlo type simulations are most suitable for nucleation studies.[44]

A model which shares these disadvantages with the continuum approach is the geometrical cone growth model.[45] This model represents a film as a set of cones started from randomly chosen seeds. The density of seeds and growth angle are chosen to agree with experimental results. Columnar structure is assumed as a starting point for the simulation, and the only physical process represented is the competition of cones which limits the number propagating. An independent continuum model would have to be developed to cover nucleation. Discrete particle simulations are able to treat nucleation and growth as one process.

## 2.3 Molecular Dynamics

Solving classical equations of motion iteratively for a system of particles is an attractive physical approach to the study of thin film growth. Usually new particles are introduced to the simulation randomly, and are allowed to interact with a Lennard-Jones potential. Knowledge of interatomic potentials indicates this is accurate only for inert gases at temperatures below about 100 K.

The computational complexity of such a method allows consideration of only a small number of particles, far too few to represent VLSI interconnection. In spite of the small simulation size, some useful studies of the general characteristics of thin film microstructure have been completed.[46-58] The influence of particle energy and ion bombardment on microstructure have been investigated using molecular dynamics simulations.

Molecular dynamics is a very powerful technique, and it can provide direct quantitative information on film growth. However, to realize this, an accurate knowledge of interaction potentials is essential, and computational abilities must be increased to allow sufficient simulation size. Approximations to the calculations have been used to increase the number of particles simulated, but systems are still orders of magnitude too small to represent films used in practical devices.

## 2.4 Ballistic Aggregation

In order to simulate aggregations of large numbers of particles, a drastically simplified version of the molecular dynamics simulation must be used. Most thin film growth simulations have relied on a variation of the hard disc model originally used by Vold[59] and modified by Sutherland[60] for the investigation of sedimentation, and first applied to film structure by Henderson *et al.*[61,62] This model considers the random serial deposition of hard spheres onto some specified substrate surface. Periodic boundary conditions are used to minimize size effects. The spheres are assumed to travel along straight parallel lines until contact is made either with the surface or with previously deposited spheres. A sphere maintains contact with the sphere it initially strikes, and is relaxed to the nearest cradle where it contacts additional spheres.

More sophisticated versions have been developed which incorporate variable sticking coefficients and various relaxation schemes to more realistically duplicate the actual growth process. While these ballistic aggregation models are somewhat simplistic in their description of the deposition process, the qualitative similarities between modeled and real films are excellent. To prove that these similarities are not fortuitous, several quantitative comparisons have been made.

The comparisons usually used are with film densities, columnar orientation, and column periodicity. Several investigators have used autocorrelation functions to calculate average column angle and periodicity. Using this technique, the column angle and period are given by the peak values of $F(\theta)$ and $G(z)$ respectively.

$$F(\theta) = \frac{1}{L\rho(1-\rho)} \int_0^L \left[ \frac{\cos\theta}{D} \int_0^{D/\cos\theta} \{\rho(x,y) - \rho\}\, dy \right]^2 dx \qquad 2.1$$

$$G(z) = \frac{1}{L} \int_0^L \{\rho_c(x) - \rho\}\{\rho_c(x+z) - \rho\}\, dx \qquad 2.2$$

where $\rho$ is the average density, $\rho_c$ is the average density along a line parallel to the columns, L is the horizontal length of the film segment, and D is the vertical depth of the film segment. In general excellent agreement between simulations and real films is obtained for zone 1 film growth.[63-65]

While much of this work has been motivated by interest in optical thin films, ballistic deposition has also been studied as part of a family of non-equilibrium growth processes. Other processes which have been studied intensively include the Eden model and diffusion-limited aggregation.[66-72] Each of these was originally developed to study cluster growth, with applications to electrodeposition, dielectric breakdown, and mechanical failure. Diffusion-limited aggregation adds particles one by one to a growing cluster via random walk trajectories. Much of the early interest was due to the belief that the process was statistically self similar.[73-79] Although the large scale behavior of such structures is still not understood, the structures remain interesting due to their complexity, the simplicity of the process, and the diverse nature of

naturally occurring examples of such structures. These include dendritic crystal growth, dielectric breakdown, and fluid-fluid displacement in porous media.[71]

Ballistic aggregation is considered to be a special case of diffusion-limited aggregation, with particles added to a cluster through linear parallel trajectories. Self similar structure again seems to occur, although the fractal dimension of the aggregate approaches the Euclidean dimension for a sufficiently large number of particles.[70] In order to simulate a sufficient number of particles ($>10^9$), lattice models have been used. These models allow particles to come to rest only on fixed lattice sites, greatly simplifying storage and computation, but introducing some undesirable biases which will be mentioned in § 3.3.

The tremendous success of the ballistic aggregation method in predicting microstructural properties of thin films, combined with its computational simplicity, makes it a very attractive approach to thin film modeling. The problems with the method are that it is difficult to relate to physical parameters, and that tremendous numbers of particles are still needed to represent a practical thin film structure. In spite of these difficulties, ballistic aggregation presents the most promising approach to incorporation of film microstructure in metallization modeling.

## 2.5 SIMBAD

The original ballistic deposition model which formed the foundation of SIMBAD was written by Brett.[80-82] He was interested in demonstrating the effect of ion bombardment on the structure of sputtered films, and the influence of surface diffusion on the transition from zone 1 to zone 2 structure. The success of the model in predicting film morphology led Brett to the realization that such a model could be of considerable interest in determining film deposition profiles for IC technologies.

This model was subsequently applied to the determination of surface profiles and step coverage for a variety of VLSI metallization geometries. The most significant information provided by the simulation was an average density profile, which demonstrated the importance of microstructure variation in films deposited over topography.[83-85] The work was now being recognized as a possible starting point for a metallization process simulation package, and as such it required an acronym. In spite of its intrinsic charm, BALListic Simulation (BALLS) was rejected in favor of the more conservative SIMulation by BAllistic Deposition (SIMBAD).

While the model appeared very successful in its predictions, there was no direct experimental confirmation of the simulated effects, and description of the phenomenon was qualitative at best. This work will first describe the model in its basic form, as recent enhancements are the subject of other graduate projects and could become proprietary information. An explanation of the relationship between simulation and real effects will then be presented, and experimental results which confirm the usefulness of such a model will be discussed in later chapters.

### 2.5.1 Simulation Basics

Conceptually SIMBAD uses a very simple model, which becomes complex due mainly to accounting and efficiency considerations. The reasons for its popularity surely include the intuitive nature and conceptual relationship to classical atomistic

processes. This also allows expansion of the model to include more complicated processes occurring during bias sputtering and chemical vapour deposition.

This description will be limited to the most common physical vapour deposition processes of evaporation and sputtering. For such processes SIMBAD uses serial deposition of identical 2-D hard discs. Two dimensional simulations are frequently used for several reasons. The number of particles required is much smaller, which reduces computation and memory requirements compared with an equivalent 3-D simulation. Furthermore, calculations for a 2-D model are much simpler than for a 3-D model, and this further speeds computation. Of course there are valid concerns about the possible loss of important 3-D phenomena in the 2-D simulation[21,86], and these concerns will be addressed later. To further reduce the number of discs required, each disc is used to represent a statistical average of many atoms. Provided discs remain much smaller than microstructure features being modelled, this is a reasonable interpretation. This approach allows simulation of device-sized regions of film. The feature resolution and simulation size of several models are shown in Figure 2.1.

The 2-D discs used in SIMBAD are generated with an appropriate angular distribution from a fixed distance above the film. This distance is less than a mean free path at common evaporation or sputtering pressures, and all the scattering effects can be included in the angular distribution. The discs follow linear paths until they strike a previously deposited disc or the substrate. The disc is then allowed a limited amount of surface diffusion to reach a position with maximum contact with other film discs. If several sites of equal coordination number are located, the one closest to the initial impact point is chosen. This diffusion model reduces local surface curvature and frequently forms a low energy hexagonal-closest-packed arrangement. The minimization of surface curvature and energy is considered to be the most important effect of surface diffusion, equivalent to surface tension minimization.[39] Sites are searched starting with locations neighboring the disc initially struck. The search proceeds to sites in contact with discs neighboring this one, and so on until the maximum diffusion distance is reached. This approach inhibits the bridging of gaps between groups of discs, but does not prevent it. This reproduces the cohesion of islands or grains, and the observed result that surface diffusion requires less energy than grain boundary diffusion.[16] The procedure is illustrated in Figure 2.2.

The result is a columnar growth very similar to a zone 1 film. As discs are deposited, they form single layer islands on the substrate. The most energetically favorable growth sites are at the edges of these islands. When the islands have grown to a width about twice the diffusion distance, discs incident on the top of the structure may not be able to diffuse to the edges. At this stage the islands begin to grow vertically, and a columnar structure evolves.

The substrate used is represented by a series of straight line segments. This allows a desired topography to be produced and avoids imposing order due to the spacing of a disc substrate. Other inputs to the simulation include the surface diffusion distance and the incident flux distribution. The diffusion distance is a function of material, substrate temperature, and deposition rate. Although measurement has been attempted, diffusion distance is still an unknown quantity.[26,87,88] For this simulation, the distance is chosen so that the size of an individual disc is much smaller than the column width. The ratio of disc diameter to column diameter is normally chosen as about 0.1, which produces film structure similar to that found in real films,

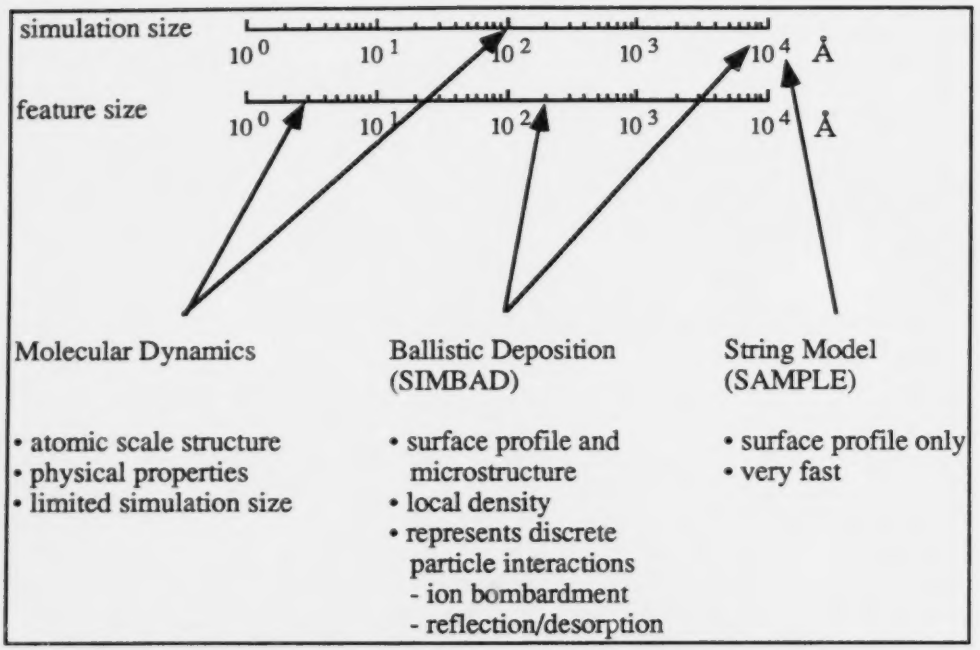


Figure 2.1. Feature resolution and simulation dimensions for film growth models.

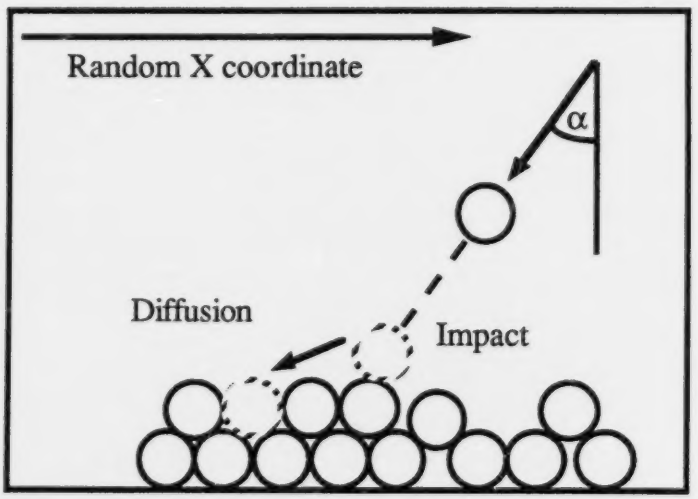


Figure 2.2. Deposition and diffusion model used in SIMBAD, where α is the deposition angle of the particle.

yet keeps computation times at a reasonable level. At this scale a single simulation disc represents about 2500 atoms. Some substrate temperature and incident energy effects could be crudely modelled by varying the diffusion distance, but to extend this model beyond zone 1 ($T_s/T_m \leq 0.3$) films would require consideration of re-evaporation and annealing of the film. Deposition rate effects are also difficult to represent with a sequential deposition, although they can also be included in the diffusion distance. Again, the model is limited to low diffusion length films which are associated with the reasonably high deposition rates (> 5Å/s) produced by evaporation and magnetron sputtering. The deposition process and parameters are determined by the incident flux distribution. The distribution represents the flux just above the substrate, so it includes the flux emitted from the source plus any scattering between the source and substrate. It therefore depends on the system geometry, the source-substrate distance, and the working gas pressure. Due to the many parameters affecting the flux distribution, it is difficult to predict analytically and measurements must be made. Given a reasonable expression for flux emitted from a point source, a Monte-Carlo simulation developed by Dew can be used to estimate the effect of scattering on the distribution.[89]

Once the deposited film has reached a desired thickness, the disc positions can be written to a file from which a plot of the film profile can be generated. The experimentally observable quantities of interest were identified earlier as microstructure, density, and step coverage. The microstructure of the simulated film can be shown using a plot of the discs. By changing random number seeds, statistical variations of the film representation can be produced. Averaging the number of discs in any region of a profile results in an average density plot. Plots are normalized to a hexagonal closest packed arrangement of discs, since this is the densest possible arrangement. The plots are displayed using a gray scale, where dark shades are used to illustrate regions of high density. The density plot is particularly well suited to identifying regions of a film in which the substrate topography has resulted in a porous, voided film. The surface profile of the film is defined as a surface of constant density, generally chosen to be 20% of the maximum density.

Despite its apparent simplicity, this model includes the essential structure-determining effects of diffusion, shadowing, and incident flux distribution. These effects are sufficient for the modeling of simple materials deposited at low reduced temperature, $T_s/T_m$ , and at reasonably high deposition rates. It provides information on film surface profiles, microstructure, and density which is relevant to microelectronics metallization and can be experimentally verified.

### 2.5.2 Simulation Algorithm

At the time of the writing of this thesis, no documentation or other information on the operation of SIMBAD exists. This shortcoming will soon be remedied, but it is worthwhile to include a description of program structure and operation in Appendix 1. Hopefully this description will be made obsolete by the documentation for the first release of SIMBAD early in 1992.

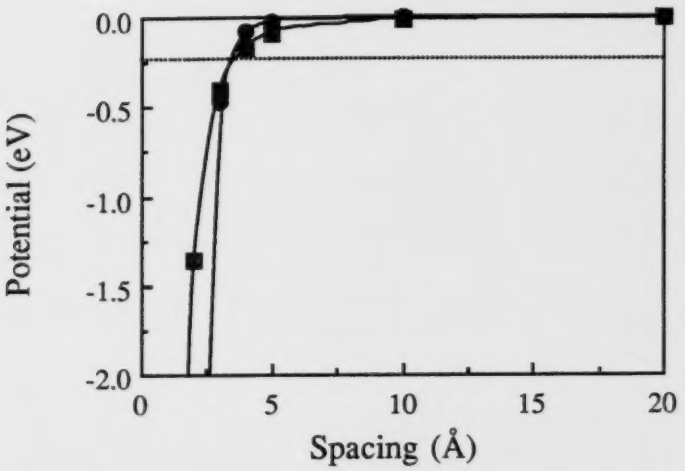


Figure 2.3. Attractive potentials for Aluminum: ■ two particles ● particle and plane. The dotted line is the thermal energy of an evaporated atom.

## 2.6 Simulation and Reality

The strongest argument for the use of a model such as this is the agreement of simulations with experimental results. For this application it is sufficient to have a model which produces observable quantities in agreement with experimental resultswithin the desired range of physical conditions. It is comforting, however, to also be able to demonstrate that the model is a physically reasonable representation of the process being simulated. A discrete model is not essential to describe the formation of microstructure in thin films, but it is intuitive and is useful when visualizing thin film growth processes.

The use of ballistic trajectories has been justified based on the absence of collisions in the simulation space, however potential interactions with the film should be considered. If a $1/r^6$ attraction is assumed between particles (Lennard-Jones), the attractive potential is insignificant relative to the thermal energy of a particle until the separation is less than about 5 Å. Figure 2.3 shows the attractive part of the potential for aluminum atoms as a function of separation, including the pair interaction and the attraction of a single particle to a semi-infinite block of identical particles. The semi infinite block of particles is a crude representation of the film. The thermal energy of an evaporated atom is included as a reference. This implies that the trajectory of an evaporated or sputtered atom will be unaffected by an attractive potential until it strikes the film.

Length scale is an awkward aspect of a model such as this. An atomistic representation of the film has already been dismissed as impractical on the scale of VLSI interconnection. Fortunately, there is evidence that thin films can be similar in terms of microstructure at least for a limited range of length scales. Figure 2.4 shows a thick aluminum film at a variety of magnifications, and implies that the structure-

magnification 16X

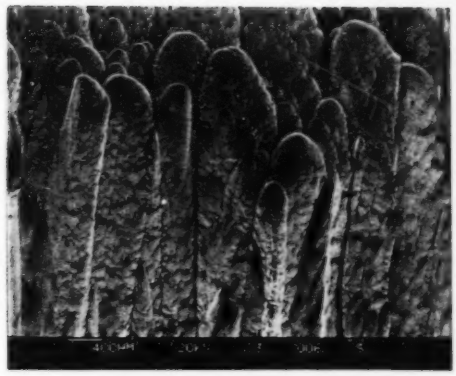

magnification 300X

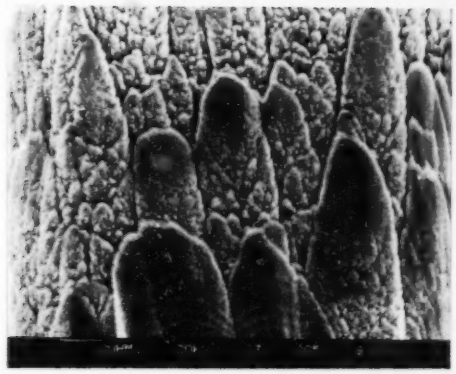

magnification 3000X

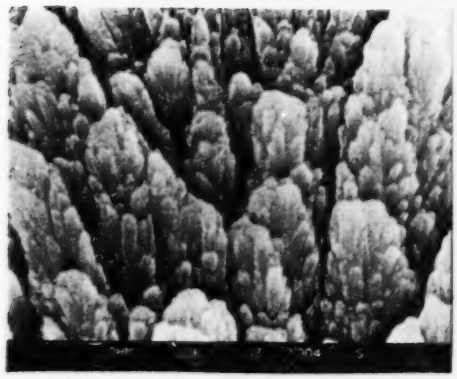

Figure 2.4. Evidence of the fractal nature of film microstructure in sputtered Al.

determining effects in thin film growth operate over a range of scales. This is because the interactions between particles of film material are similar regardless of whether the particles represent single atoms or aggregations of many atoms. This seems to be obvious for hard discs or spheres. It is also true for particles interacting with a $1/r^6$ attraction, as shown by Hiemenz and described below.[90]

Consider two spherical particles of the same composition and radius $R_a$. Assume every atom in sphere 1a attracts every atom in sphere 2a according to a $1/r^6$ law. If the material has a number density $\rho N_a/M$ atoms/cm$^3$, then there are $\rho N_a/MdV_{1a}$ atoms in a volume element of sphere 1a and $\rho N_a/MdV_{2a}$ in a volume element of sphere 2a. The number of pairwise interactions between the spheres is then $\frac{1}{2}(\rho N_a/M)^2 dV_{1a}dV_{2a}$. This number multiplied by the interaction per pair gives the incremental potential energy for the two interacting volume elements:

$$d\Phi_a = -\frac{1}{2}(\rho N_a/M)^2 r_a^{-6}\, dV_{1a}\, dV_{2a} \qquad 2.3$$

Integrating over both spheres:

$$\Phi_a = -\frac{1}{2}(\rho N_a/M)^2 \iint \frac{dV_{1a}\, dV_{2a}}{r_a^6} \qquad 2.4$$

Now consider a second set of spheres of the same material, but of larger radius, such that

$$R_b = f R_a \qquad 2.5$$

and at a separation

$$d_b = f d_a \qquad 2.6$$

Following the procedure used in case a, the interaction potential for case b is:

$$\Phi_b = -\frac{1}{2}(\rho N_a/M)^2 \iint \frac{dV_{1b}\, dV_{2b}}{r_b^6} \qquad 2.7$$

but since the scale is different by a factor $f$, this can be written:

$$\Phi_b = -\frac{1}{2}(\rho N_a/M)^2 \iint \frac{(f^3 dV_{1a})\,(f^3 dV_{2a})}{(f r_a)^6} \qquad 2.8$$

Note that the factor $f$ cancels out and the result is

$$\Phi_b = \Phi_a \qquad 2.9$$

Or the potential energy of attraction is identical in the two cases! This indicates that for $1/r^6$ attractions two molecules 3Å in diameter and 10 Å apart will interact with the same energy as two spheres of the same material 300Å in diameter and 1000Å apart. It is interesting to note that this is a direct consequence of the $1/r^6$ potential which appears in permanent or induced dipole interactions.

The choice of a diffusion model is difficult, as the process is not well understood. The model chosen, which allows movement of deposited discs to a position with a maximum number of neighbors, allows for minimization of surface energy over a short range. This works quite well for films with limited surface

diffusion, but for higher diffusion distances a long range minimization of surface area is necessary. This work will be limited to low temperature, limited diffusion film growth.

This completes the description of the model. The next step is to demonstrate how this model reproduces basic properties of thin films deposited at low temperature, and attempt to explain why it works. Only then will the model be applied to thin films deposited over topography, and be used to identify problems in VLSI metallization.

# Chapter 3: Simulating Basic Film Properties

The first test for a model such as this is in a study of basic film morphology and density. Since this work will ultimately deal with films deposited over topography, it is useful to study the change in film structure with deposition angle. This will also provide some guide to choosing parameters for the topography simulations. The agreement between simulated and real density and column angles will be demonstrated, and an explanation of the angular variation of these properties in ballistic deposition simulations will be presented.

## 3.1 Film Structure and Density

The parameter which has the largest effect on film morphology is the adatom diffusion distance.[16] Since the diffusion calculation is the most time-consuming part of the simulation, it is important to limit the distance to the minimum value which yields realistic results. For a simulation with no diffusion, the structure formed is very porous and is composed of tree-like chains of discs. As soon as diffusion is allowed, the structure becomes much more dense and columnar, beginning to resemble a real film. The change in structure with increasing diffusion distance is illustrated in Figure 3.1.

A more quantitative evaluation of the diffusion length at which the simulation begins to resemble a real film can be made by considering film density as a function of diffusion distance. Figure 3.2 illustrates how film density changes as a function of deposition angle and diffusion distance, for evaporation simulations. For a given diffusion length, the density is almost constant for deposition angles up to about 40°, and begins to drop rapidly at higher angles. This effect will be shown in a later chapter to cause a number of metallization problems. For the moment, it is more important to consider the effect of changing diffusion lengths. For short diffusion distances, the film density at low angles of incidence is well below the bulk density. As the distance is increased, the density increases and quickly approaches a limit. For diffusion lengths above about 4 disc diameters there is very little change in film density. Most simulations in this work were therefore executed using a maximum diffusion distance of 4 disc diameters.

Figure 3.3 is a similar plot for sputtering simulations. The wider angular distribution used for sputtering yields results similar to those obtained for evaporation. The angular distribution for deposition flux used in these simulations varied as the cosine of the deposition angle. This distribution is generally accepted as a good approximation for a sputtering source.[105] The importance of flux distributions in thin film deposition warrants a separate study. In this work a cosine or a measured distribution was used.

Figure 3.4 shows simulated densities for an evaporation distribution and values for evaporated aluminum and germanium. All values are normalized to the density at normal incidence since that is how the published data was available.

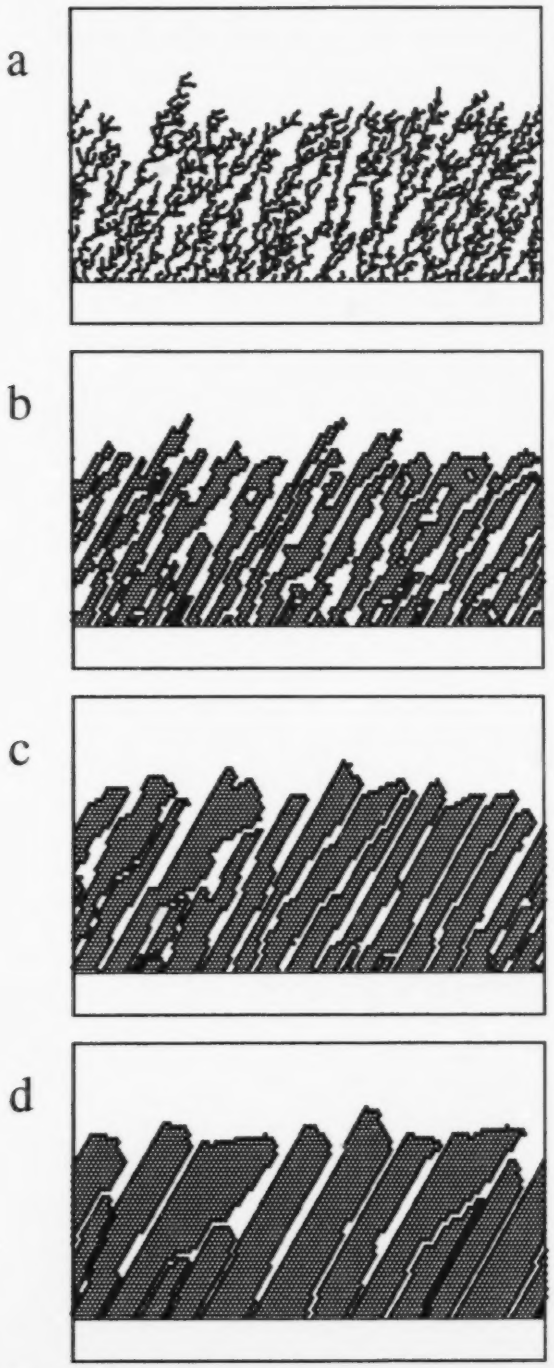


Figure 3.1. Change in column structure with increasing diffusion distance. Deposition angle was 50°. Diffusion distances are a) 0 disc diameters, b) 1 diameter, c) 2 diameters, d) 4 diameters.

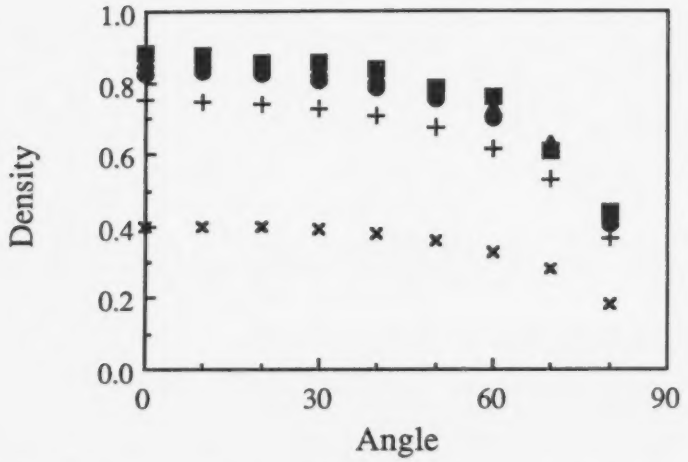


Figure 3.2. Density variation with deposition angle for evaporation simulations. diffusion distance: × 0 diameters; + 1 diameter; ● 2 diameters; ▲ 3 diameters; ■ 4 diameters.

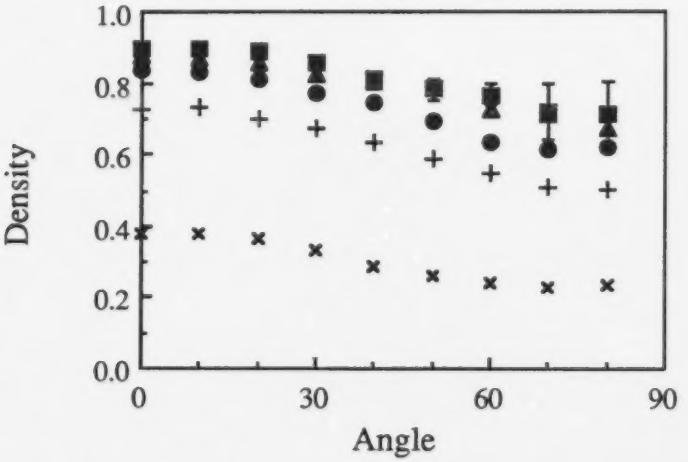


Figure 3.3. Density variation with deposition angle for sputtering simulations. diffusion distance: × 0 diameters; + 1 diameters; ● 2 diameters; ▲ 3 diameters; ■ 4 diameters. Uncertainties are the standard deviation of 5 simulations.

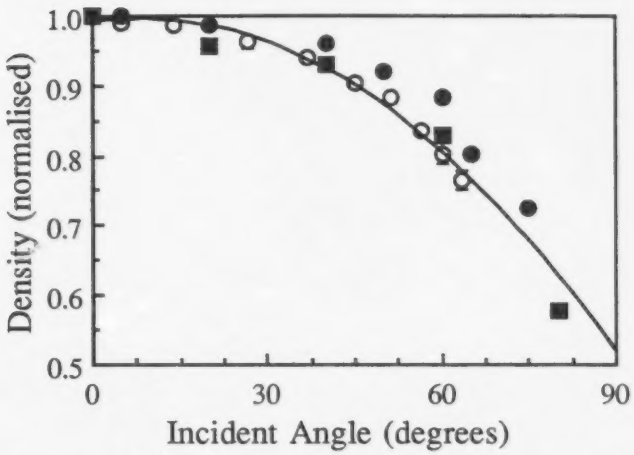


Figure 3.4. Density variation with deposition angle for ○ evaporation simulations and evaporated Ge ■ ref. 107, ● ref. 108. The line is a fit to SIMBAD data. Uncertainties are standard deviation of 10 runs.

Clearly SIMBAD provides a good representation of the trend. Sputtered data was not available, but measurements are provided in Chapter 5. The density variation shown here is a direct consequence of shadowing in the growing film, and is closely related to the column angles of the film structure.

## 3.2 Column Angles

A second quantitative measure of the correlation between simulations and real films is the measurement of column angles. The behavior of column angle as a function of film deposition angle is normally assumed to follow the tangent rule, previously discussed. A compilation of data shows that most data agrees with this empirical expression only for deposition angles less than about 60°. This discrepancy has been realized for some time, but the tangent rule persists as a handy expression for most oblique incidence films. Ballistic deposition models have been found to produce films with column angle behavior closely following that of real films, so it is of interest to derive a shadowing-based expression for column angle as a function of flux angle.

### 3.2.1 Column Angle Theory

An attempt was made to derive such an expression by Fiedler and Schirmer.[28] They assumed deposition of hard discs with shadowing and an average growth angle $\beta$ given by:

$$\beta = \frac{\int_{\gamma 1}^{\gamma 2} \gamma \cos(\gamma - \alpha) d\gamma}{\int_{\gamma 1}^{\gamma 2} \cos(\gamma - \alpha) d\gamma} \qquad 3.1$$

where $\alpha$ is the angle of vapour incidence and $\gamma 1$ and $\gamma 2$ define the surface of a column that receives flux. Here an expression will be derived for deposition onto an array of hemispherically topped columns, taking the center of the region receiving flux as the fastest growing direction. This results in an expression superior to the tangent rule in terms of high angle and asymptotic behavior, much simpler than that used by Fiedler and Schirmer, and without any parameter-fitting required.

### 3.2.1.1 Films with no Relaxation

To begin with, consider the sequential deposition of two-dimensional hard discs with no diffusion. We will start with a linear arrangement of discs at a spacing of $a \cdot d$ where $d$ is the disc diameter. Each of these discs will capture incident discs whose centers pass within a diameter $2 \cdot d$, unless shadowing occurs. Assuming a uniform incident distribution of discs at angle $\alpha$, each incident disc will contribute to the column growth at an angle $\gamma$, the angle between the surface normal and the line between the centers of the two interacting particles. The column orientation angle $\beta$, is then given by the average of $\gamma$, as shown in Figure 3.5.

An expression for $\beta$ in terms of $\alpha$ must be established. $\beta = f(\alpha, \gamma 1, \gamma 2)$ will first be found, and then $\gamma 1$ and $\gamma 2$ will be determined, depending on the shadowing conditions which are a function of $\alpha$ and $a$. This can be done by finding the width of the region in which each disc receives flux.

$$b = (D/2) \cdot (\sin(\alpha - \beta) + \sin(\gamma 2 - \alpha)) \qquad 3.2$$

also

$$b = (b1 + b2)/2 \qquad 3.3$$

so

$$\sin(\alpha - \beta) + \sin(\gamma 2 - \alpha) = (\sin(\alpha - \gamma 1) + \sin(\gamma 2 - \alpha))/2 \qquad 3.4$$

Notice all angles are measured from the vertical axis, so $\gamma 1 < 0$.

Thus $$\sin(\alpha - \beta) = (\sin(\alpha - \gamma 1) - \sin(\gamma 2 - \alpha))/2 \qquad 3.5$$

is the general expression relating the average growth angle to the other parameters. We must now consider three distinct cases.

(i) shadowing from both neighbors, $\gamma 1 > \alpha - 90$ ($\gamma 1 = -\gamma 2 = \gamma$), see Figure 3.6. In this case the range within which a given disc will capture incident discs is affected by the proximity of neighboring discs on both sides.

Expanding equation 3.5,

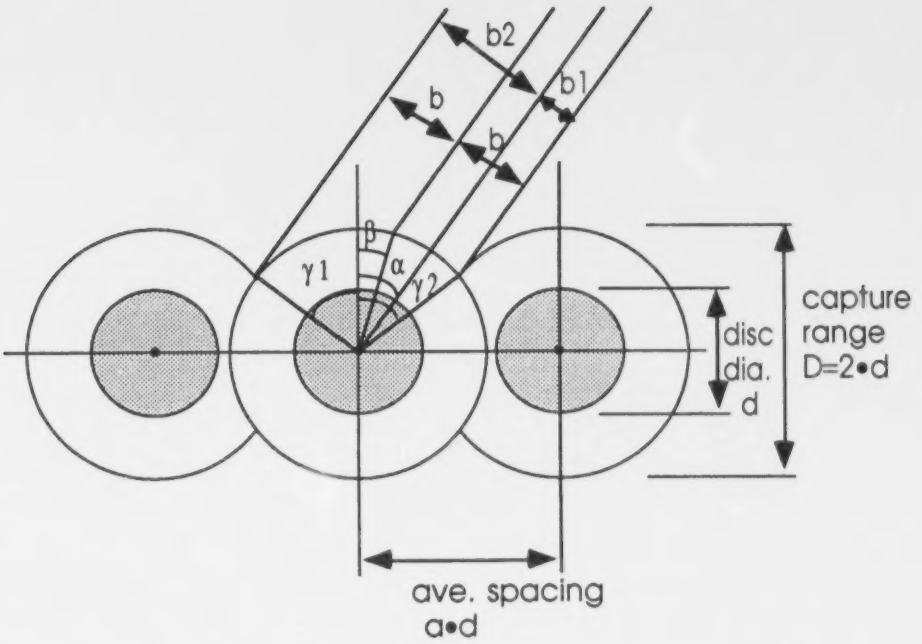


Figure 3.5. Geometry of the column growth problem.

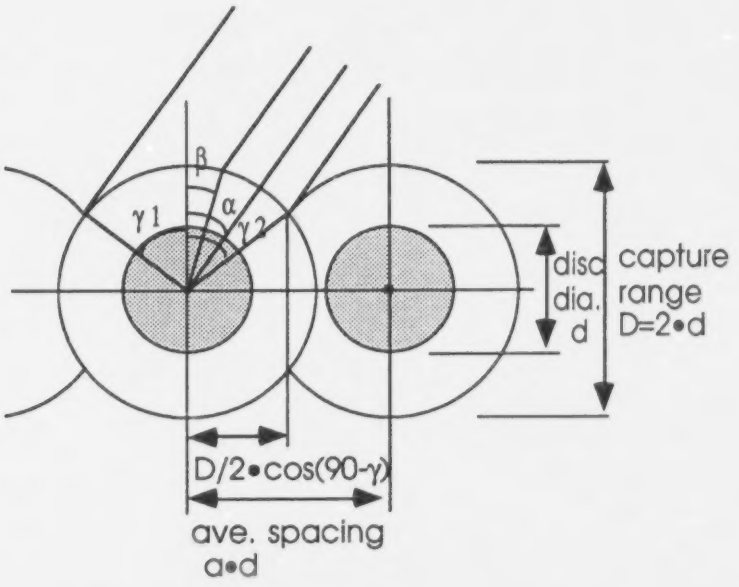


Figure 3.6. Growth with shadowing due to both neighbors.

$$\sin(\alpha-\beta) =$$
$$((\cos(\gamma 1)+\cos(\gamma 2))\ \sin(\alpha) - (\sin(\gamma 1)+\sin(\gamma 2))\ \cos(\alpha))/2 \qquad 3.6$$

or substituting for $\gamma 1$ and $\gamma 2$,

$$\sin(\alpha-\beta) = (2\ \cos(\gamma)\sin(\alpha))/2 \qquad 3.7$$

Writing this explicitly for $\beta$,

$$\beta = \alpha - \sin^{-1}(\cos(\gamma)\ \sin(\alpha)), \text{ where } D/2 \bullet \cos(90-\gamma) = a \bullet d/2 \qquad 3.8$$

$$\text{or } \sin(\gamma) = a/2 \qquad 3.9$$

**(ii)** shadowing from one neighbor, $\gamma 1 = \alpha - 90$ see Figure 3.7

$$\sin(\alpha-\beta) = (\sin(\alpha-\gamma 1) - \sin(\gamma 2-\alpha))/2 \qquad 3.10$$

now becomes

$$\sin(\alpha-\beta) = (1 - a \bullet \cos(\alpha) + 1)/2 \qquad 3.11$$

or

$$\beta = \alpha - \sin^{-1}(1 - a/2\ \cos(\alpha)) \qquad 3.12$$

**(iii)** no shadowing, $\gamma 1 = \alpha - 90$, $\gamma 2 = \alpha + 90$

$$\sin(\alpha-\beta) = (\sin(\alpha-\gamma 1) - \sin(\gamma 2-\alpha))/2 \qquad 3.13$$

now becomes

$$\sin(\alpha-\beta) = (\sin(90) - \sin(90))/2 \qquad 3.14$$

$$\sin(\alpha-\beta) = 0 \qquad 3.15$$

or

$$\alpha = \beta \qquad 3.16$$

Note that case (i) is most likely for small angles while case (ii) will probably control the structure for higher angles.

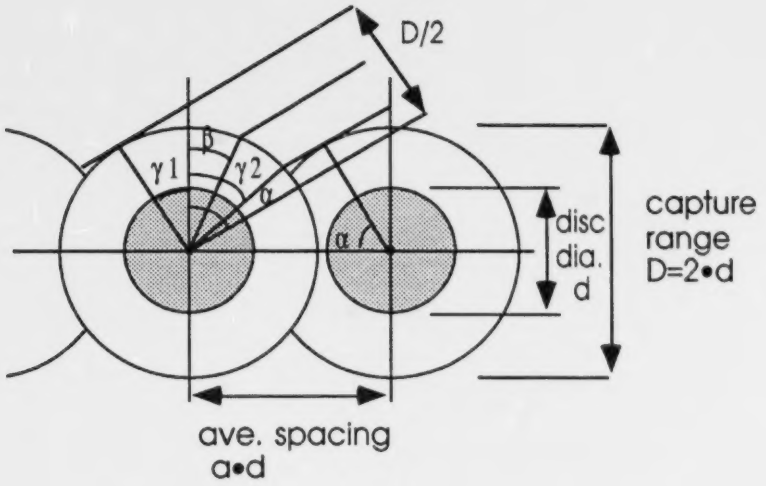


Figure 3.7. Growth with shadowing from one neighbor.

### 3.2.1.2 Films with Relaxation

We now consider the case of sequential deposition of hard discs where the discs diffuse over some range after initial contact with the film, but are constrained to diffusion on a single column. If the diffusion length is large enough, this results in column structures where the column diameters are significantly larger than the disc diameters.

To represent this process, consider the approach presented above, but now consider incident discs ( diameter $\delta$) much smaller than the discs in the initial array (diameter $d$), which makes $D=d+\delta$. This is similar to a case of 2 dimensional columns with circular tops. With the assumption that the relaxation is isotropic, the analysis above in terms of the angles is valid. We must consider the same 3 cases.

**(i)** Shadowing from both neighbors, $\beta = \alpha - \sin^{-1}(\cos(\gamma)\sin(\alpha))$

Now $(d+\delta)/2 \cos(90-\gamma)=a \bullet d/2,$ 3.17

or $\sin(\gamma)=a$ where $\delta \ll d$ 3.18

**(ii)** Shadowing from one neighbor,

in this case,

$$(d+\delta)/2 \sin(\alpha-\beta) = ( (d+\delta)/2 - a \bullet d \bullet \cos(\alpha) + (d+\delta)/2)/2 \quad 3.19$$

or $\sin(\alpha-\beta) = ( 1 - a \bullet d \bullet \cos(\alpha)/(d+\delta))$ 3.20

so $\beta = \alpha - \sin^{-1}(1 - a\cos(\alpha))$ where $\delta \ll d$ 3.21

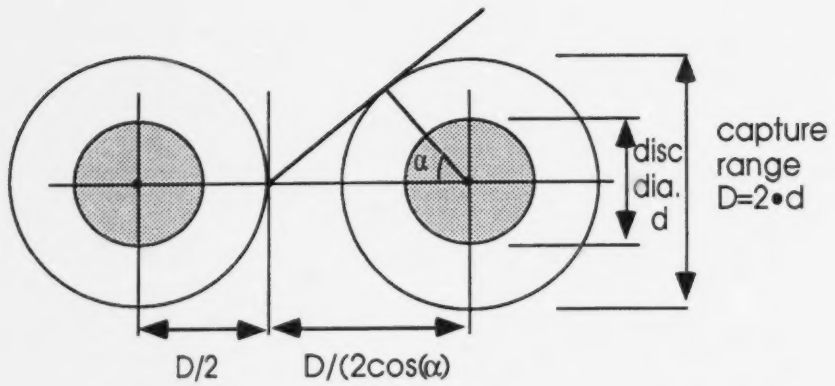


Figure 3.8. Determining column spacing $a$.

**(iii)** No shadowing, $\alpha = \beta$ as before

The only change from the expressions with no relaxation is the replacement of $a/2$ with $a$. Of course $a$ will be dependent on the stochastic nature of the deposition, but we can make some estimates of its value.

### 3.2.1.3 Column Spacing $a$

Obviously column spacing has limits. On average it will be determined by the shadow length $D/(2\cos(\alpha))$ plus the capture radius $D/2$, as shown in Figure 3.8. This implies $a$ will take the form

$$a \bullet d = (D+D/\cos(\alpha))/2 \qquad 3.22$$

First consider discs with no relaxation, so $D=2 \bullet d$. This means

$$a = (1+1/\cos(\alpha)) \qquad 3.23$$

At normal incidence only about half of a smooth surface will be covered with discs, since after this the incident discs are almost certain to be captured by those already deposited. This implies that at $\alpha=0$ we expect $a=2$ in agreement with this expression. Measurements from simulations support this expression, as shown in Figure 3.9.

For the case where the incident discs are small compared with the columns, $D=d+\delta$ or $D \approx d$, and we expect only a small spacing between columns. In this case we expect

$$a=(1+1/\cos(\alpha))/2 \qquad 3.24$$

Note that the expression for $a$ with no relaxation is twice that for $a$ with relaxation. This means that the expressions for column angle will give identical results for the two problems!

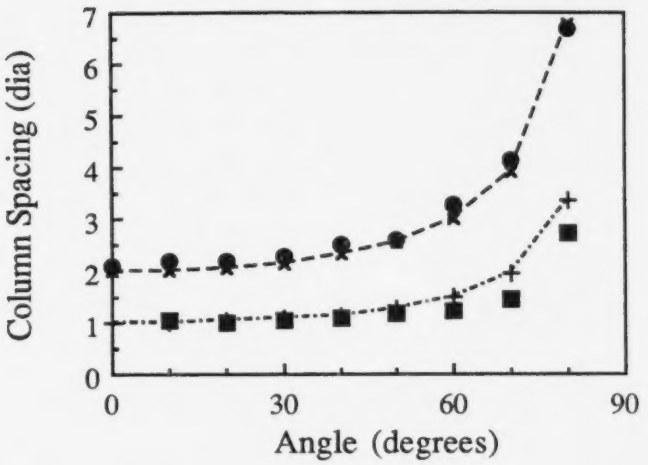


Figure 3.9. Column spacing from simulations with ● 0 diameter diffusion length, ■ 4 diameter diffusion length, and from the expression × 3.23 and + 3.24.

**(i)** shadowing from both neighbors

$$\beta = \alpha - \sin^{-1}(\cos(\gamma)\sin(\alpha)) \qquad 3.25$$

$$\sin(\gamma)=(1+1/\cos(\alpha))/2 \qquad 3.26$$

This will never occur for the given ɑ and $\alpha>0$, since $\sin(\gamma)>1$!

**(ii)** shadowing from one neighbor

$$\beta = \alpha - \sin^{-1}((1-\cos(\alpha))/2) \qquad 3.27$$

**(iii)** no shadowing

$$\beta = \alpha \qquad 3.28$$

### 3.2.1.4 Results

The expression 3.27 is most useful for describing the behavior of column angle as a function of deposition angle for ballistic deposition simulations. As can be seen from Figure 3.10, the function agrees reasonably well with simulated and experimental results for all angles. At low angles the discrepancy between experimental data and

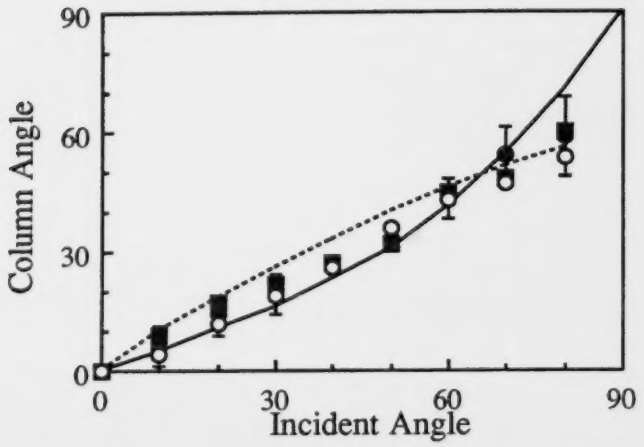


Figure 3.10. Simulation column angles for: ● 0 diameter diffusion length; ■ 4 diameter diffusion length. Experimental results O are for thermally evaporated $MgF_2$. Theoretical column angles predicted by the tangent rule (solid line) and the theory presented here (dashed line) are also shown. Typical uncertainties are shown for the 0 diffusion simulations as the standard deviation for 5 simulations.

the calculated curve is likely due to too high a value of $\alpha$. Results would be improved for these angles by the use of equation 3.8 and an appropriate value of $\alpha$. The tangent rule gives acceptable results for low angle of incidence, but at high angles the derived expression is superior. This expression also has the advantage that as the angle of incidence approaches 90°, the column angle reaches a limit of 60°. This is more reasonable than expecting the column angle to approach the incidence angle at oblique incidence.

The variation of column angle with angle of incidence, and the variation of density with angle of incidence are very similar for ballistic deposition simulations and real films deposited by physical vapour deposition at low temperature. This indicates that such simulations will be useful to study the microstructure of thin films deposited over topography. Before proceeding with simulation studies however, one important consideration in two dimensional simulation must be addressed. That consideration is the limitation of representing a three dimensional process in two dimensions.

## 3.3 Dimensionality

In order to make SIMBAD a tractable approach to the problem of simulating film deposition for interconnection, it has been limited to two dimensions. The aforementioned concerns about the loss of important three dimensional effects can be addressed by some preliminary work with a full three dimensional simulation.

A three dimensional version of the SIMBAD algorithm presents several problems. The first is that the number of particles used increases as $n^{3/2}$, where n is

the number of particles required for a 2-D simulation of some dimension. This limits the size of a 3-D simulation due to computer memory constraints. Perhaps more important is the problem of calculating final disk locations, which becomes very computationally intensive and is susceptible to round off errors. To avoid these problems a lattice type of simulation can be used. This permits particles to occupy only pre-determined locations forming a regular lattice.

The use of an lattice type of simulation promotes epitaxial film growth, which is unrealistic in most situations. In three dimensions epitaxy is reduced due to the number of possible packing arrangements. For a hexagonal closest packed structure, there are three possible arrangements for any layer. Since these are all permitted in this simulation, there are many situations where groups of discs cannot join, and discrete columns form. The problem of epitaxial film growth is therefore reduced. A description and listing of the code is provided in appendix II.

Using this simple 3-D model, some comparisons between 3-D and 2-D simulations can be made. Direct comparison of microstructure is difficult to make since the 3-D structure is not easily viewed. Density profiles for films deposited over topography, and density as a function of angle are much easier to compare.

The density was calculated for films deposited at angles from 0° to 80°. The diffusion lengths for 3-D simulations are effectively longer than those used for 2-D simulations. The extra degree of freedom provided by the 3-D simulation results in denser films than 2-D simulation with an equivalent diffusion distance. The variation of density with deposition angle, however, is very similar for both types of simulation. This variation is shown in Figure 3.11.

Of course the topic of interest is films deposited over topography. Initial comparisons of a 3-D simulation of a film deposited on a trench with an equivalent off-lattice 2-D simulation shows different density variations on the trench sidewalls. These density plots are shown in Figure 3.12 and 3.13. A small number of disks was used in the 2-D simulation to give disk size comparable with the 3-D simulation. While the 2-D off-lattice simulation shows a decrease in density right down the sidewall, the 3-D simulation shows a fairly high density in this bottom corner. This can be explained by the difference between lattice and off-lattice simulations. The 2-D simulation does not constrain discs to lattice points, and therefore there is little probability that columns growing from the base and the sidewall of the trench can ever join. The result is the observed low density extending to the corner where these columns intersect. With the 3-D simulation, there is an increased probability that these columns will join when they meet, and as a result high density in the bottom corner is observed.

To compare 3-D and 2-D simulations, it is then necessary to compare on-lattice simulations only. If the 2-D simulation is altered to result in on-lattice growth, the density plot resembles the 3-D result quite closely, as shown in Figure 3.13. The fact that the results agree indicates that very little information is lost by restricting simulations to two dimensions.

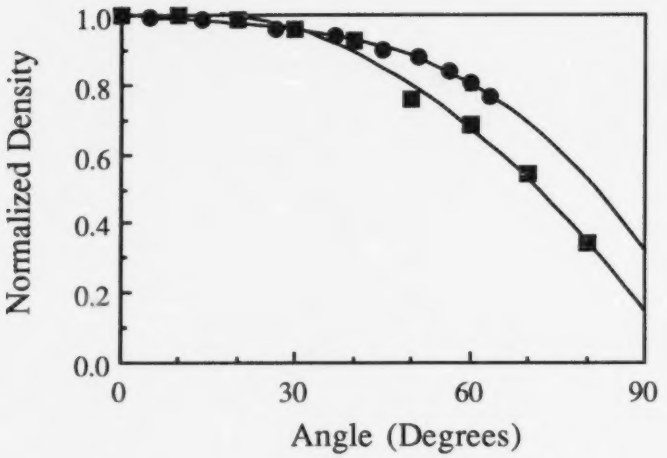


Figure 3.11. Simulated density variation with deposition angle for 2-D ● and 3-D ■ models.

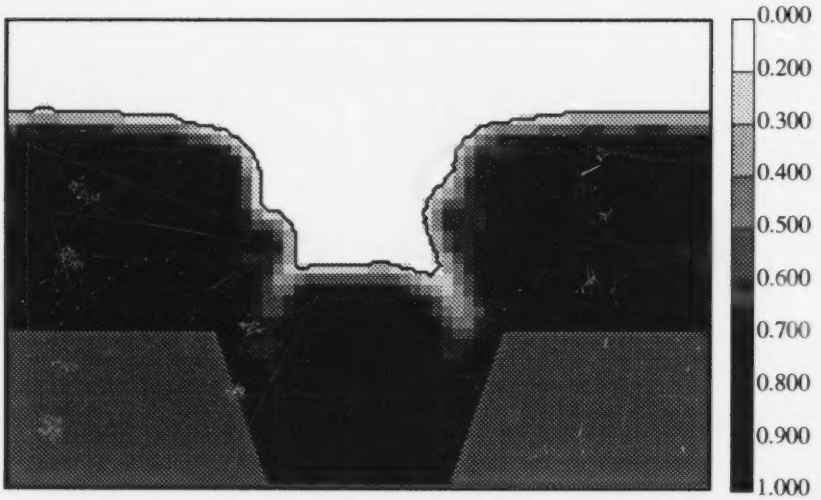


Figure 3.12. Density plot of a film deposited over a trench using a 3-D on-lattice simulation.

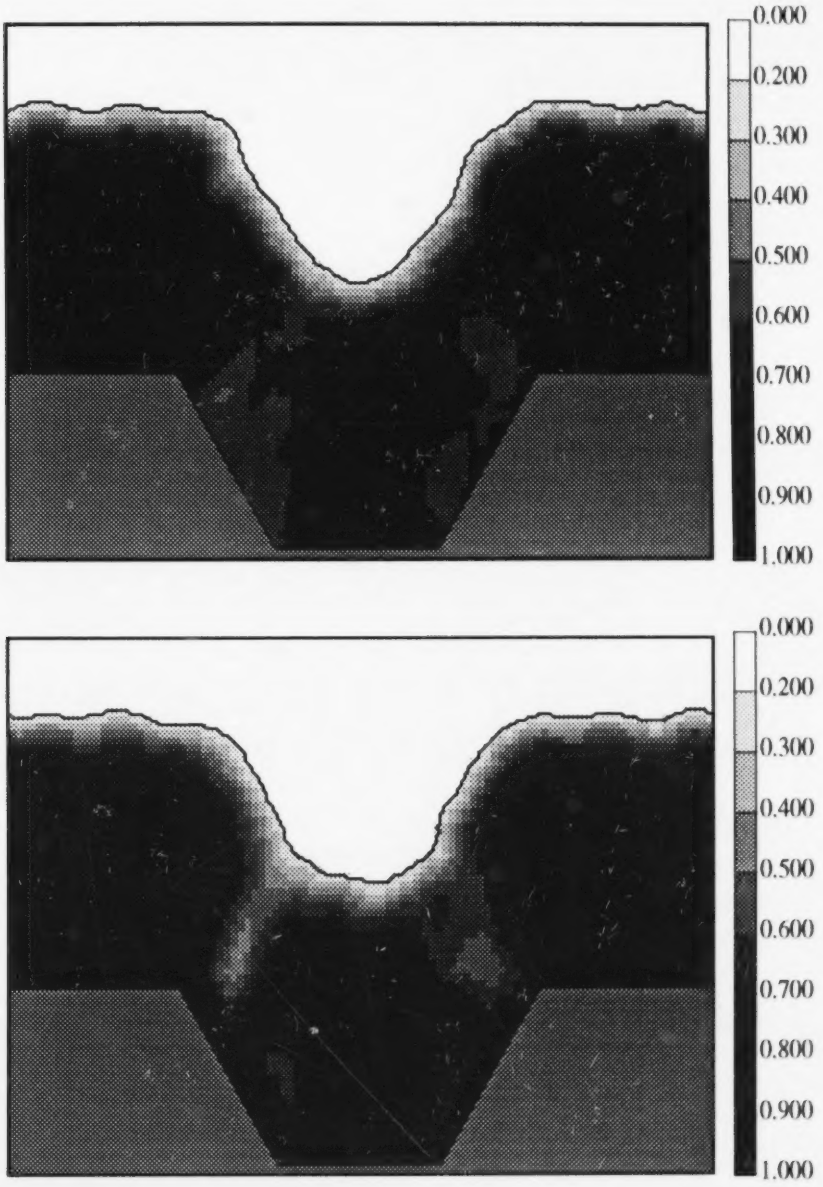


Figure 3.13. Density plots of films deposited over trenches using the 2-D off-lattice simulation (top), and the 2-D on-lattice simulation.

## 3.4 Column Anisotropy†

An interesting result of the three dimensional simulation, and further evidence of the importance of shadowing and limited relaxation in the formation of thin film structure, is the anisotropy of column shape in the plane of the film. The anisotropy has been attributed to a variety of effects; however the simulations presented here are the first evidence that the anisotropy can be attributed largely to shadowing effects. Column structure in the film cross-section has already been described in some detail. In the film plane, the column structures are found to be symmetric or equiaxed for normal incidence, but for oblique incidence films, the columns become elongated in the direction perpendicular to the plane of incidence, as illustrated in Figure 3.14. Elongation of columns has been observed to switch from perpendicular to parallel to the plane of incidence when the deposition angle approaches grazing incidence.[91] These effects are therefore referred to as perpendicular and parallel anisotropy, and have attracted attention due to their effect on mechanical, optical, electrical, and magnetic properties of films.[26,92-94]

Most early reports of columnar microstructure are concerned with the effects of oblique vapour incidence upon anisotropies within the plane of the film. The observation that anisotropies were oriented either perpendicular or parallel to the plane of incidence led to the proposal that shadowing of incident atoms was responsible.[95] While this idea resulted in a qualitative explanation of the structure, other observations indicated that additional processes influenced the effect. The composition of alloy films was found to strongly affect the degree of anisotropy.[96] It was also noted that oxygen content of a film increases with the angle of deposition due to increased porosity and reduced deposition rate.[97] Momentum of incident atoms has also been considered as a factor in the formation of anisotropic columns.[98,99] From these studies no dominant mechanism has emerged which explains the formation of elongated nuclei and columns.

The key to understanding the origin of column formation was the computer simulation of Henderson, previously discussed.[61] Neither momentum nor oxygen adsorption are explicitly considered in the model, hence geometric shadowing of incident atoms by those within the film is responsible for the structure. A similar technique can be used to investigate the elongation of columns in the film plane. Using the 3-D ballistic deposition model to study column shapes, the behavior of titanium (Ti) films sputtered at oblique incidence can be reproduced by considering only shadowing and limited diffusion of incident atoms.

### 3.4.1 Anisotropy in Sputtered Titanium

Anisotropic properties of films deposited at oblique incidence have been studied most carefully for evaporated ferromagnetic materials.[92] However, most thin evaporated films have structure on too fine a scale to be easily observed with a scanning electron microscope (SEM). Sputtered films also exhibit anisotropic oblique incidence effects, frequently on a larger scale than evaporated films.[100] Ti sputtered at

---

† Material in this section has been accepted for publication as:

R.N. Tait, T. Smy, and M.J. Brett, J. Vac. Sci. Technol. A**10**(4), (1992).

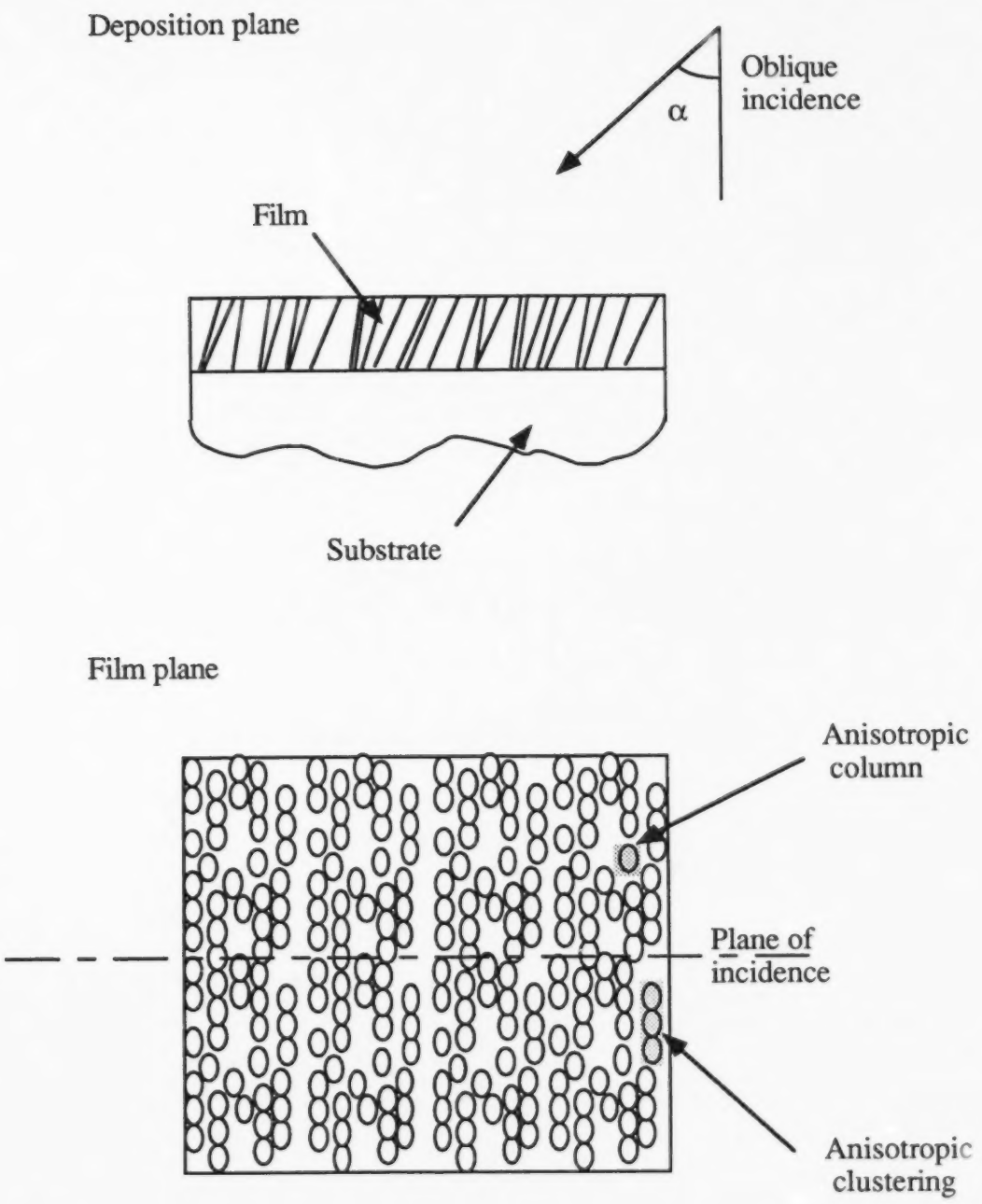


Figure 3.14. Anisotropies in film microstructure.

low pressure has been found to yield pronounced columnar structure easily viewed in a SEM, and is therefore the material chosen for this study.

Ti was sputtered from a 12.5 x 20 cm planar magnetron target onto substrates cut from a silicon wafer and held at angles from 0° to 80°. The silicon substrates have a smooth surface to an almost atomic level, and the surface structure of any film on such a substrate is a result of the deposition process, not the initial surface. Films approximately 4 μm thick were grown at 600 W DC power and 65 mPa argon pressure for a deposition rate of 16 Å/s at normal incidence. At this pressure, scattering of material between target and substrate is minimal. The target to substrate distance was 10 cm and the axis of rotation for the angled substrates was parallel to the long axis of the target.

The resulting films show anisotropic or oval cross section columnar structures above 20°, as observed viewing the film surface in a SEM. At lower angles neutral bombardment appears to have caused denser films.[15] The anisotropy increases until the deposition angle reaches 60°, and then decreases slightly. Films do not show the reversal of anisotropy observed in evaporated films deposited at angles greater than 70°. These results will be shown in detail; simulated films closely resemble this behavior.

### 3.4.2 Anisotropy Results

Sputtered Ti films deposited at 60°,70°and 80° are shown in Figure 3.15. The photographs are taken normal to the substrate. Manipulating the samples to view parallel to the column direction is difficult, and the view provided here is sufficient to determine the column shape. There are several qualitative observations to be made from the photographs. All three films show oval shaped columns oriented with their long axes perpendicular to the plane of incidence. This is most obvious with the 80° film because the reduced density results in a photograph with greater contrast than the other two. A close inspection reveals that the anisotropy is due to not only the elliptical column shape, but also the formation of chains of columns. This chain formation is not obvious at the lower angles due to the closer packing of the columns.

The simulations of these films are shown in Figure 3.16. Some basic features of the photographs are reproduced; the simulated columns show elongated tops. The formation of chains of columns also occurs, and in many cases the columns touch but do not join due to the different packing orientations. The 80° simulation shows a much lower density of columns than the other two, and the columns appear more equiaxed. To quantify these effects some measurements of column shape are necessary.

Because of insufficient contrast in the photographs, image analysis software could not be employed to identify and measure columns. Measurements were therefore done directly from the pictures, with data averaged over 25 columns for each simulation. Only individual columns were studied, as the objective measurement of column chains is difficult. Individual simulated columns were identified as clusters of closest packed spheres separated by voids or packing dislocations. Real columns were defined by regions of uniform brightness in the photographs.

The results of the measurement are shown in Figure 3.17. Both the real films and the simulations show similar trends, with a peak in column anisotropy at about 60°. The anisotropy drops off slightly above this angle, with the simulation showing a more dramatic drop than the real films. Neither simulations nor real films show the

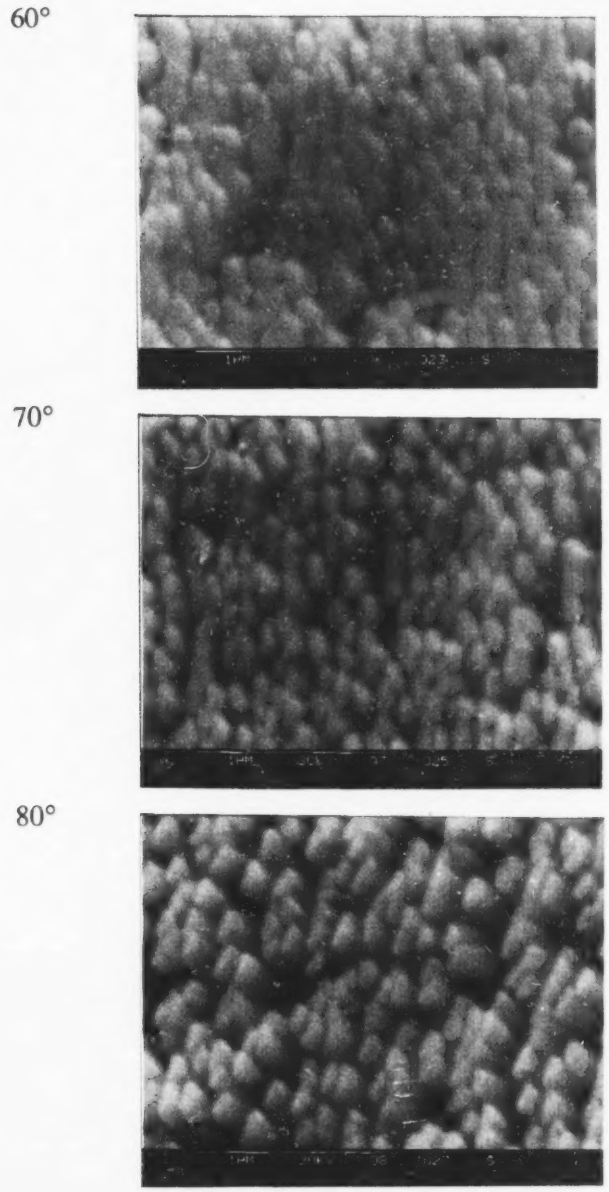


Figure 3.15. Film plane anisotropy in sputtered Ti.

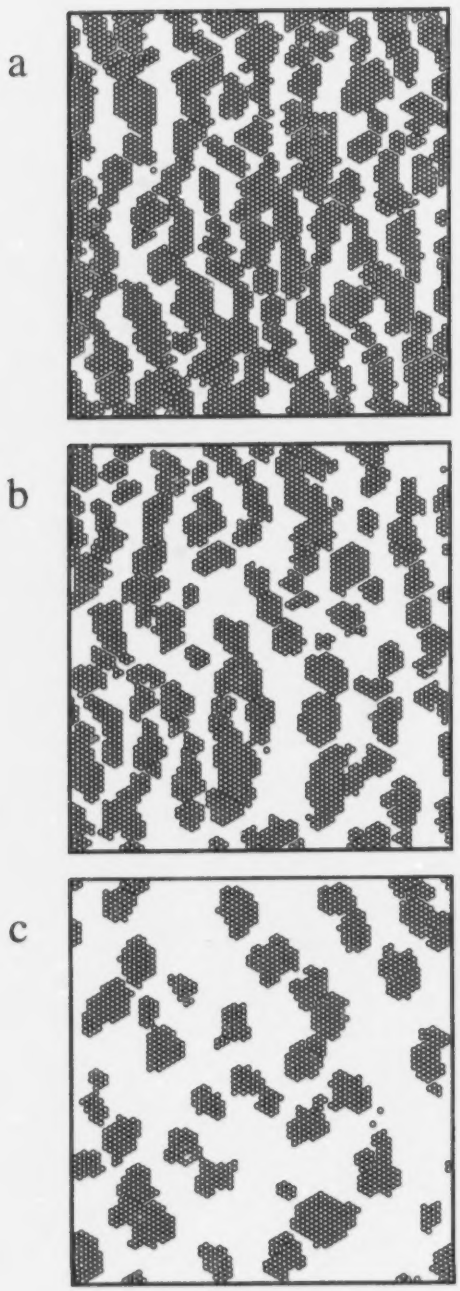


Figure 3.16. Film plane anisotropy simulations. Deposition angles are a) 60°, b) 70°, c) 80°.

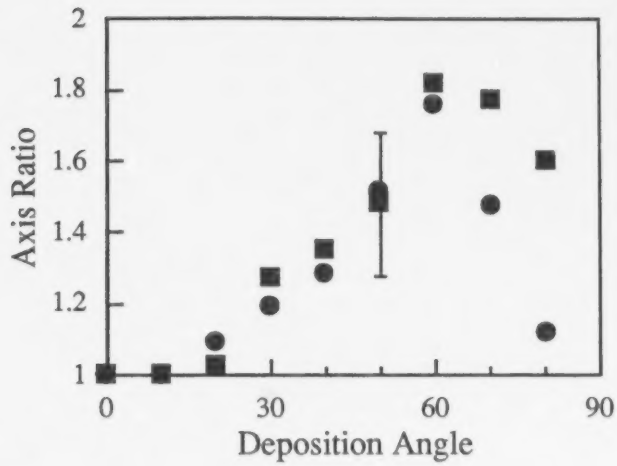


Figure 3.17. Column shape measurements: ■ sputtered titanium and ● simulations. A typical uncertainty is shown as the standard deviation of 25 measurements. Axis ratio is the ratio of column axis perpendicular to the deposition plane to column axis parallel to the plane.

reversal of the direction of anisotropy observed in other studies at angles greater than 70°. The reversal is likely due to factors other than diffusion or shadowing since it does not occur in the simulation. The difference in the anisotropy between the simulation and the real films could be due to a number of factors. The angular distribution of deposition flux used is an approximation, and deposition rate, which varies with angle of deposition, is not a factor in the simulation. Also, the degree of anisotropy is dependent on substrate temperature, which will influence the diffusion distance of incident material.[101]

The correlation between these shape measurements and film properties can be seen in the published data. For example, the measurement of magnetization directions for Ni-Fe films by Cohen shows an increase in magnetic anisotropy with angle of incidence which peaks at 60° and drops rapidly above this value. This effect is attributed to the film structure, and therefore agrees with the shape measurements presented here, as well as with measurements of resistance and optical dispersion anisotropy.[91,18] The anisotropy in these properties can be large due to the chains of columns which were observed but not quantified here. It appears that for incidence angles up to about 70°, anisotropic structure and film properties are due mainly to shadowing effects in the growing film.

An explanation of how anisotropy can occur can be postulated based on Smith's description of formation of chains of columns due to shadowing.[102] Starting with a random distribution of nucleation sites, and assuming the growth of circular islands, many nucleation sites will be shadowed from receiving material. The shadowing occurs in only one direction, so that the unshadowed nucleation sites grow into islands. These tend to join into chains perpendicular to the plane of incidence, or

in the direction of no shadowing, as graphically illustrated by Smith.[102] If islands are allowed to join together to form a single elongated column seed, this mechanism could be used to explain the formation of elongated columns as well as column chains. A weakness of this interpretation is the uniformity of column shape seen in Figure 3.15.

Based on this shadowing mechanism, a crude estimate of the angular dependence of column shape can be made by considering the simulation growth process. In simulations with diffusion distance $d$, the column width in the plane of incidence has been found to be about twice the diffusion distance, or $2d$. If an island is considered to be a hemispherical region with a diameter $d$, it will cast a shadow $d/\cos\alpha$. When this shadow length becomes longer than the diffusion distance, islands cannot join in this direction. This occurs for

$$d/\cos\alpha > 2d \qquad 3.36$$

$$\alpha > 60° \qquad 3.37$$

which is about the angle at which the observed anisotropy reaches a peak. As the angle of incidence is further increased, the number of growing islands drops due to the extreme shadowing. At some point the average spacing of the islands becomes large enough that islands do not join in any direction, and as this happens the anisotropy begins to disappear. At these extreme angles, effects other than the geometric shadowing become dominant in determining column shape. The result is the parallel anisotropy which was not observed in these simple simulations.

## 3.5 Conclusion

SIMBAD has now been shown to provide good predictions of film density and morphology, and has been useful in explaining microstructural features using the mechanisms of shadowing and surface diffusion. It now remains to be demonstrated how this can be applied to simulation of the VLSI metallization process. That is, how it can be used to gain useful information on films deposited over topography by physical vapour deposition.

# Chapter 4: Deposition over Topography

This chapter demonstrates the key to the success of SIMBAD as a tool for the simulation of metallization processes. That is , its ability to generate microstructure, density, and surface profiles in agreement with experimental results. This will be shown starting with the simplest deposition process, thermal evaporation. Sputtered films will be discussed in some detail, as sputtering is preferred over evaporation for metallization due to improved step coverage. Comparison of experimental and simulation results will be discussed for each process.

## 4.1 Evaporated Films†

### 4.1.1 Film Structure

Evaporation studies were carried out using magnesium flouride, a material commonly used for antireflection coatings. This material was chosen due to availability and ease of preparation and handling. The observed results can be generalized to elemental metals, as $MgF_2$ evaporates as a compound, with essentially no dissociation.

To form a substrate for the evaporation, oxide lines of nominal width and height of 1.5 μm were fabricated on a silicon wafer using standard photolithographic techniques. Subsequently, a $MgF_2$ film 0.75 μm thick was evaporated onto the wafers from a molybdenum boat. The base pressure of the system was approximately $3x10^{-4}$ Pa and the deposition rate was 4 nm $s^{-1}$. During the deposition the wafer was held stationary above the source at a prescribed angle of either 5° or 40°. The lines on the wafer were oriented perpendicular to the plane defined by the normal of the wafer and the vertical from the source. Cross-sections of the wafer for scanning electron microscopy were prepared by cleaving the wafer immediately after deposition, and coating with a very thin layer of gold.

A scanning electron cross-section micrograph of a coated step is shown in Figure 4.1. The direction of deposition was 5° from the left of vertical, creating a shadowed uncoated void region to the right of the step. The $MgF_2$ film on the planar silicon surface shows a faint, nearly vertical columnar morphology attributed to a zone 1 structure. The ratio of substrate temperature during deposition to $MgF_2$ melting temperature was estimated to be 0.26 and is thus consistent with the observed structure. Of particular interest is the columnar structure on the left wall of the step. It is oriented at approximately 30° from the vertical and shows evidence of pores or void regions that are not apparent on the planar film segment. All steps observed (approximately 30) showed similar porous regions on the left step wall.

---

† The material in this section has been published as:

R.N. Tait, T. Smy, and M.J. Brett, Thin Solid Films **187**, pp. 375-384 (1990).

Figure 4.1. $MgF_2$ evaporated at 5° onto an oxide line

Figure 4.2. $MgF_2$ evaporated at 40° onto an oxide line

The orientations of the columns on the step wall should obey the expression derived in the previous chapter. Direct measurement of column angle $\beta$ from Figure 4.1 gives $\beta$=53° from the side wall normal. The tangent rule with $\alpha$=78° gives a value $\beta$=67° while the derived expression Equation 3.27 gives a prediction of $\beta$=55°. This confirms the inaccuracy of the tangent rule at high angles of incidence.

A simulated film grown over an identical step is shown in Figure 4.3. This simulation consists of about 30 000 discs deposited at a fixed angle of 5° and allowed to relax within four disc diameters. The step coverage, surface profile and shape of the shadow region agree with the real film in Figure 4.1. The simulated film has a nearly vertical columnar microstructure on the horizontal substrate surface but also exhibits a less dense region on the left step wall. The orientation of the simulated columns on the left step wall is approximately 57°±4° from the surface normal, in agreement with the value for the real film.

Figure 4.2 shows a $MgF_2$ film evaporated onto a similar step at an angle of 40° to the wafer normal. Substantial shadowing has occurred to the right of the step, caused by this oblique angle of vapour incidence. The $MgF_2$ film has separated slightly from the substrate as a result of cleaving or film stress. Evaporated $MgF_2$ coatings are known to have a large internal tensile stress. A faintly visible columnar structure is oriented towards the the incident flux direction, as expected. Of significance in this micrograph is the absence of any obvious low density or porous region on the left step wall. At this angle of incidence the side wall receives flux at about the same angle as the horizontal section of substrate, so the film is uniform over this region. The simulation of the 40° film in Figure 4.2 is shown in Figure 4.4. As was the case for the 5° film, the step coverage, surface profile and shape of the shadowed region agree well with the real film.

### 4.1.2 Film Density

For real films, it has been observed that the film density decreases with increasing angle of incidence, as shadowing increases and voids between columns widen. SIMBAD simulations of films evaporated at various angles have shown a similar density variation with angle.

Due to this agreement, calculation of density from simulation of films evaporated over topography is expected to agree well with real films. The gray scale density plots corresponding to the 5° and 40° simulated films are shown in Figures 4.3 and 4.4. Lower density regions near the surface of the film are an artefact due to averaging across the surface. In Figure 4.3, SIMBAD predicts a significant decrease in density of the left side wall coating due to the oblique angle at which vapour strikes the side wall. This low density region correlates with the porous film region seen beside the wall in Figure 4.1. Figure 4.4 predicts a relatively constant film density over the step, since the angle of incidence on the horizontal substrate is 40° and the angle of incidence on the side wall (relative to the side wall normal) is similar at 41°. These results concur with the apparent homogeneity of the film seen in Figure 4.2.

SIMBAD is thus successful in simulating properties of $MgF_2$ films evaporated over oxide lines on a silicon wafer. The simulations give surface profiles of the deposited film and provide an indication of trends in microstructure and local film density, in agreement with experimental results. With this success it is logical to

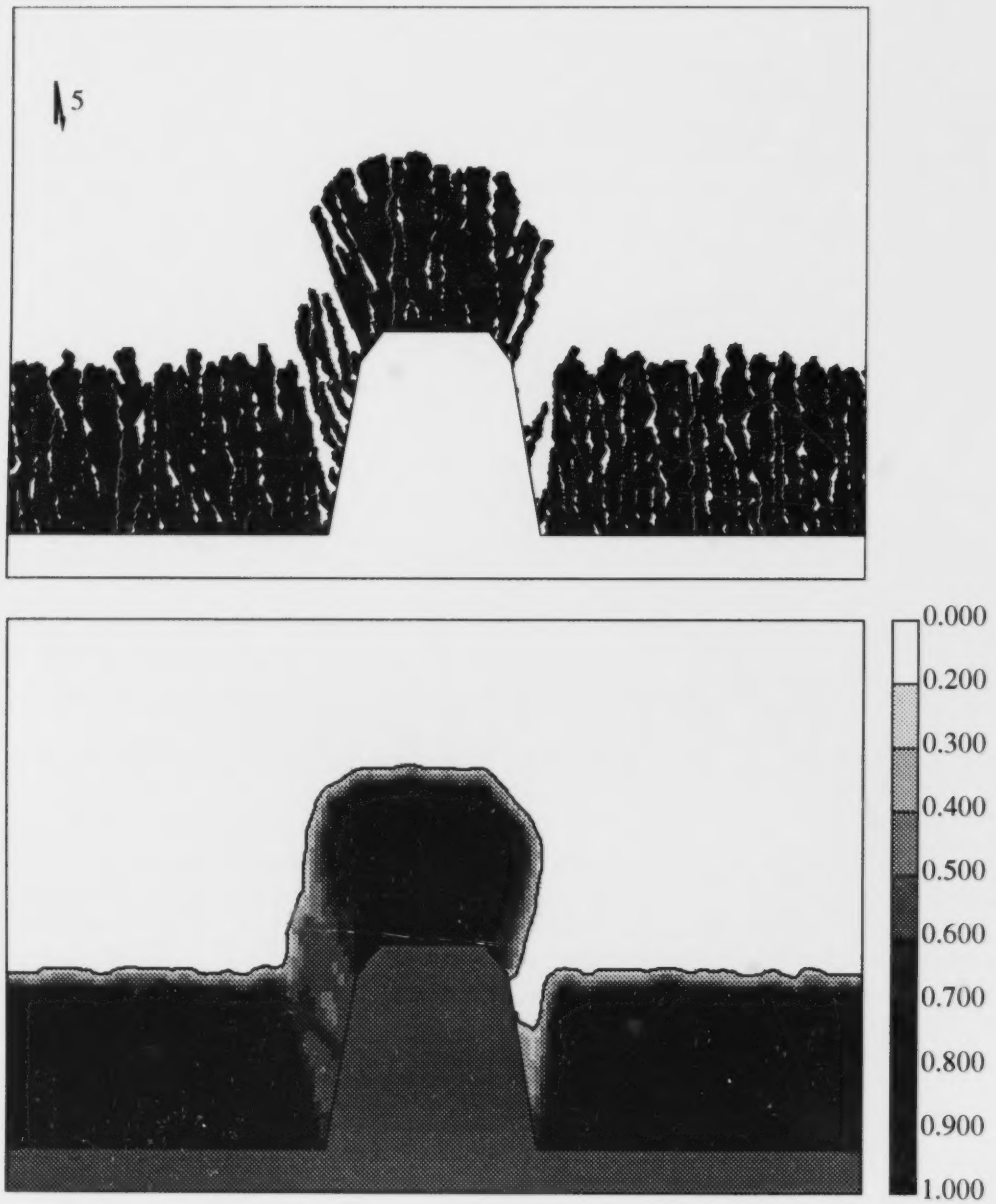


Figure 4.3. SIMBAD simulation of a film evaporated at 5°. A disc plot is shown at the top, and a density average for 10 simulations is shown at the bottom.

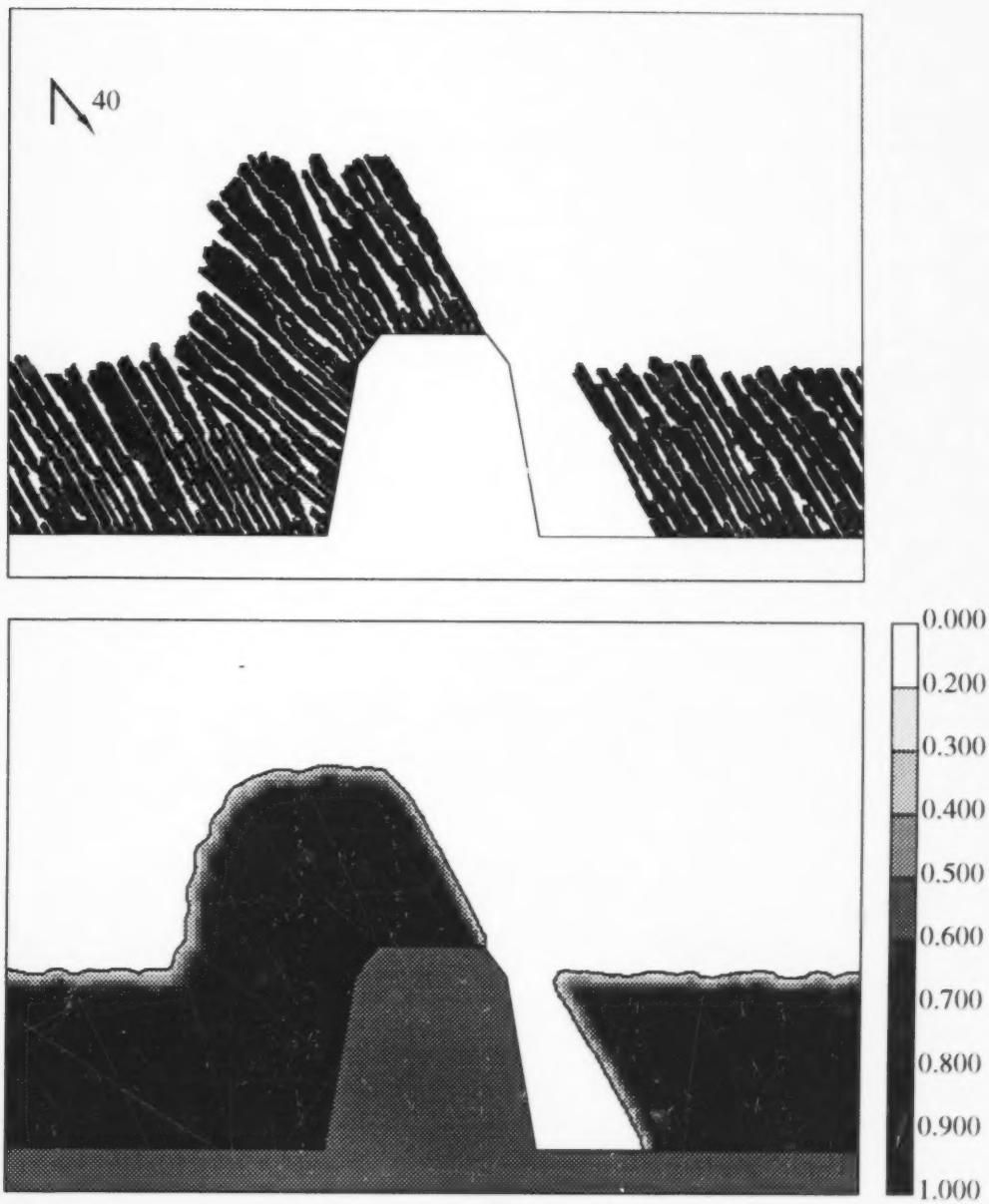


Figure 4.4. SIMBAD simulation of a film evaporated at 40°. A disc plot is shown at the top, and a density average for 10 simulations is shown at the bottom.

move on to metals sputtered over topography, as these films will be of more technological interest for VLSI circuits.

## 4.2 Sputtered Films†

In this section the validity of the SIMBAD results is further confirmed by preliminary etching studies of molybdenum films deposited over oxide steps. The etching procedure used allows for the determination of low density regions in the deposited films and indicates that SIMBAD gives a good representation of trends in film density for sputtered as well as evaporated films. More quantitative discussion of the etching process will be delayed until the next chapter.

### 4.2.1 Film Deposition and Etching

Oxide lines of nominal width and height 1.5 μm were fabricated on a silicon wafer using standard photolithographic methods. A molybdenum film approximately 1.7 μm thick was then deposited by DC sputtering with a 2 inch planar magnetron source. Molybdenum was chosen for the metal film since its high melting point and refractory nature promote the growth of a columnar microstructure at low substrate temperatures (<500 K). Base pressure of the cryopumped chamber was $2.7 \times 10^{-4}$ Pa and sputtering was performed at an argon pressure of 1.63 Pa and a target power of 220 W at 0.75 A. A high pressure was chosen for sputter deposition to inhibit the growth of a dense bombardment-induced zone T structure, and to improve adhesion of the metal film to the oxide. Films deposited at lower pressures were found to delaminate from the substrate. The resulting deposition rate was 0.7 nm/s.

Following film deposition, the wafer was cleaved to smaller samples for etching. A common purpose of etching of metals is that of revealing the general microstructure. Etching reagents are normally chosen to reveal grain boundaries along with some contrast between adjoining grains or phases. For a thin metal film deposited at low substrate temperature, grains are readily identified as discrete columns in a cross-sectional photograph. There is some evidence that etch rate is inversely proportional to density [103,104] which implies that longer etch times can be used and highly-voided (low density) regions will etch away more quickly than dense regions. Very low density regions of a metal film should vanish quickly, and the etch rate should slow as only more uniformly dense regions remain.

The etching solution chosen was a standard molybdenum etch used for grain boundary definition. It consisted of 15 g $K_3Fe(CN)_6$ and 2 g NaOH in 100 ml of water. Etching was done by simple immersion at room temperature for times between 0 and 2.5 minutes, and samples were then rinsed in water and methanol. Preparation of samples for SEM analysis consisted of only a thin coating of sputtered gold.

---

† The material in this section has been published as:

R.N. Tait, T. Smy, and M.J. Brett, J. Vac. Sci. Technol. A8(3), pp. 1593-1596 (1990).

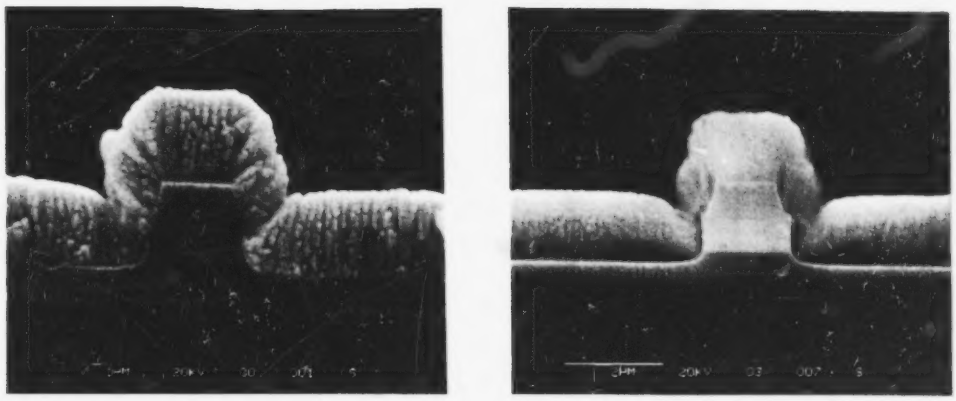

a) unetched

b) 30 second etch

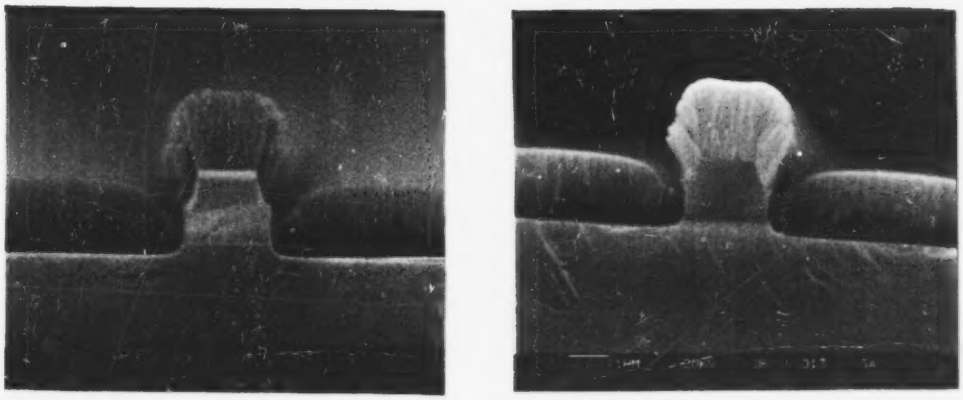

c) 60 second etch

d) 150 second etch

Figure 4.5. Confirmation of density predictions in sputtered Mo.

### 4.2.2 Film Structure and Density

A scanning electron micrograph of a cross section of the unetched film is shown in Figure 4.5 a). Over-etching of the oxide in production of the step caused erosion of the upper corners of the step. The grainy surface is attributable to a surplus of gold deposited to prevent sample charging in the SEM. In spite of the gold coating, the photograph shows the columnar microstructure for a film sputtered on an unheated substrate. Since the ratio of substrate temperature during deposition to melting temperature of molybdenum is approximately $T_s/T_m = 0.15$, columnar zone 1 structure is expected. As has been previously noted, continuous voids can be discerned angling upwards from the lower corners of the step. This is the region an etchant is expected to remove first.

Figure 4.5 b) shows the same film after 30 seconds of immersion in the potassium ferricyanide solution. The film on the side walls shows some initial etching, but the image is unfocused due to etching of the film back from the edge of the sample. This etch back also causes poor definition of the top surface of the film.

The sample in Figure 4.5 c) is clearer than that in Figure 4.5 b). After 1 minute of etching there are definite trenches etched to the sidewalls, etching back from the edge is minor, and gold decoration is not as noticable. At this etch time it appears that the porous regions of the film have been removed and the etch rate has dropped, as only dense regions remain. After 2.5 minutes the etched trenches are slightly cleaner but no larger, as shown in Figure 4.5 d).

For simulation of sputter deposition, a cosine distribution compressed to $\pm 60°$ from the vertical was chosen for the angular distribution of particle flux, based on the result of Blech[105] and widened slightly to account for the high sputter pressure used. Simulations used approximately 40,000 discs, taking about 15 minutes on a SUN sparcstation 1+ computer.

A gray scale density profile of a simulated film generated by SIMBAD is shown in Figure 4.6. Through comparison with the photographs, it appears that the low density regions on the sidewalls of the step are accurately predicted. Since etch rate inceases with decreasing density (§4.2.1), this density plot indicates that etching will be most rapid along the low density cracks towards the lower corners of the step. It should then proceed up the step sidewalls which are not as low in density. The last film regions to etch will be on the horizontal surfaces; the substrate and the top of the step. The photographs confirm that such a progression in etching did occur.

The result of a single simulation is also shown in Figure 4.6. This is a plot of the full 40,000 discs used in a simulation. The simulation demonstrates microstructure very similar to that of the real film. Comparing this with the unetched film of Figure 4.5 a), some minor differences are noticeable. Step coverage was measured at about 0.40 for the simulation, and 0.50 for the real film. Step coverage depends on the angular flux distribution used, and the discrepancy may be due to the fact that a 5 cm sputter gun was used rather than the larger target used for distribution measurements.[105]. Angular distribution measurements for a 12.5 cm sputter gun have shown a distribution peaked at about 25° from the target normal and varying more than 20% from a cosine distribution.[106] However, the most significant features of the simulations appear regardless of the angular flux distribution used, namely the low density regions on the sidewalls of the step.

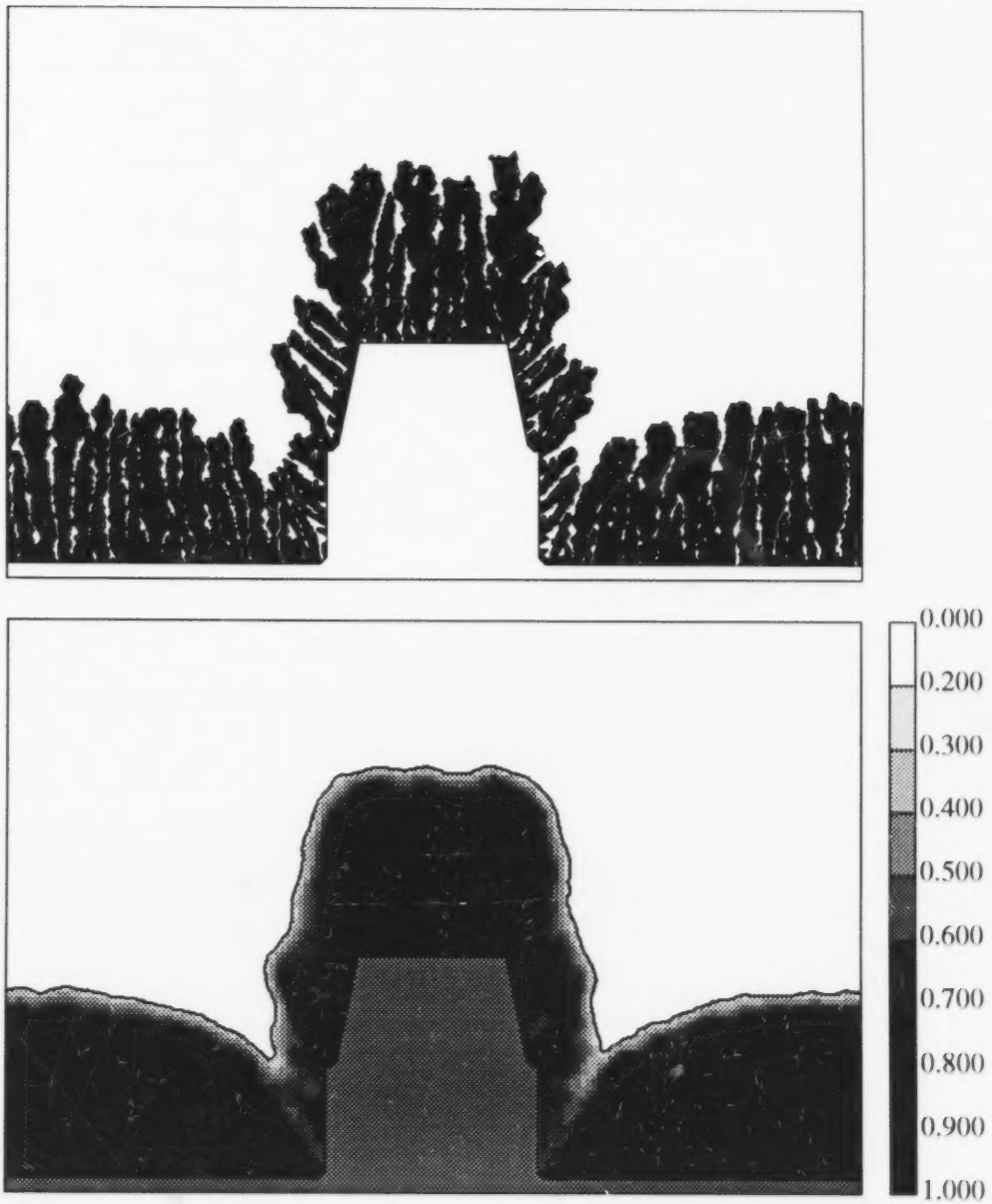


Figure 4.6. SIMBAD simulation and density plot of a sputtered film. A disc plot is shown at the top, and a density average for 10 simulations is shown at the bottom.

With this result, the thin film growth simulation program SIMBAD has been shown to provide good predictions of step coverage and film microstructure for both evaporated and sputtered materials. By studying the etching of molybdenum films on oxide steps, the local film density predictions of SIMBAD have been qualitatively verified. Not only does etching proceed into very low density cracks in the lower corners of the steps, it also occurs on the slightly higher density sidewall, eventually leaving only high density sections on the substrate and the top of the step. A more quantitative study of this etching process is necessary, which leads to the extension of SIMBAD to simulation of common etching processes. These etching processes are discussed in the next chapter.

# Chapter 5: Etching

Results presented up to this point have been descriptive and qualitative. Data is presented in this chapter which quantitatively confirms the density variation of sputtered tungsten as a function of deposition angle as predicted by SIMBAD. Once the density variation is established, etch rate can be measured as a function of density. With a relationship between density and etch rate, density of real and simulated films deposited over topography can be compared by observing their etching behavior. The plasma etching process is also introduced to demonstrate the potential for expansion of SIMBAD to simulation of other processes. This is a more relevant etching method for silicon processing technology, and the success of the model demonstrates the usefulness of geometrical models for processes involving complicated reaction kinetics, provided the rates are limited by the transport process.

## 5.1 Wet Etching†

Following the success of the preliminary etching result shown in Chapter 4, a more careful and complete experiment was done. This included measurements of density and etch rate for sputtered tungsten, and the development of a density-based wet etching algorithm for SIMBAD.

### 5.1.1 Density Measurements

In order to obtain some quantitative evidence of agreement between the densities predicted by SIMBAD for sputtered films and the densities of real films, it was necessary to measure the variation of density as a function of deposition angle for a planar magnetron sputtering source. Measurements such as this have been done previously for a variety of evaporated materials[107,108], showing good agreement with SIMBAD predictions, as shown in Figure 3.4. Data for sputtered materials is more difficult to find; hence measurements were made.

Tungsten is an excellent material for this type of measurement. It has a high atomic mass which allows accurate measurement of film mass even with the use of small substrates. This reduces problems with deposition rate and thickness gradients across films deposited at high angles. As it is a refractory metal it tends to form pronounced zone 1 microstructure on room temperature substrates, and the porosity results in the density decrease observed at high deposition angles.

The density measurement was done by sputtering tungsten on flat silicon substrates. The substrate wafer was sawed into 1.1 cm squares which were then cleaned and

---

† The material in this section has been published as:

R.N. Tait, S.K. Dew, T. Smy, and M.J. Brett, J. Appl. Phys. **70** (8), pp. 4295-4300 (1991).

weighed on a Mettler H51 balance accurate to 10 μg. They were placed in holders with 1 cm square windows exposed to the sputtering source. This size compromises between accurate mass measurement and thickness uniformity. Angles between the source normal and the substrate normal were varied in 10° increments from 0° to 80°. Approximately 0.5 μm of tungsten was DC sputtered from the 12.5 by 20 cm magnetron at 250W constant power, 1.6 Pa argon pressure, and a 10 cm target-to-substrate distance. High pressure and low power were used to inhibit neutral bombardment and to improve adhesion of the film to the substrate.[109-111] Following the deposition, substrates were again weighed to obtain the mass of the deposited film. The thickness was found using a Tencor Alpha-Step 200 profilometer to measure the height of the step formed at the edge of the film by the window in the substrate holder. Using the mass and volume of the film, the density as a function of deposition angle was calculated.

The density measurement as a function of deposition angle is shown in Figure 5.1, for four different sets of data. Not all angles show four points as stress in the thicker films caused some to delaminate from the substrate. The scatter can be accounted for by small changes in positioning of samples in the sputter system and by inaccuracies in the measurement. Film mass was on the order of 1 mg and could be measured easily with only a few percent uncertainty. Thickness measurements were slightly less accurate. Density is calculated from these measured values, hence the uncertainty in density is larger than the uncertainty in mass or thickness. The density was observed to stay close to bulk density until the substrate angle reached about 50°, when it began to drop off rapidly to about 60% of bulk density at 80°. SIMBAD density results for planar films using a cosine distribution for incident vapour flux are included and follow the measured trend quite well. The density predictions using the distribution $|\sin(4\theta)|$, explained later, also agrees with the density simulations but shows a slight dip in density at intermediate angles due to the zero flux predicted at normal incidence. The real distribution is not expected to produce zero flux at low angles of incidence.

Once the density measurement was complete a four point probe was used to measure sheet resistance as a function of deposition angle. Results were converted to resistivity using the measured film thickness.

The sheet resistance measurements for a set of these films are shown in Figure 5.2. Four point probe measurements were made with the probe tips parallel to the deposition plane (formed by the source normal and substrate normal) and perpendicular to it, with very similar results in both cases. Only the measurement made parallel to the deposition plane is shown. The sheet resistance stays low until the film becomes very porous, at about 60°, when it begins to increase rapidly. The effect is most likely due to porosity of films produced at high deposition angles, although residual gas incorporation due to decreased deposition rate should also be considered. Obviously the resistivity increase could cause problems in contact vias with steep sidewalls.

In order to demonstrate the relevance of the measured density and resistivity variation with angle of vapour incidence, tungsten films deposited over topography were studied. Wet etching was chosen as a technique for revealing porous regions in these films. However, before proceeding with films on topography, it was first necessary to demonstrate the dependence of etch rate on density using sputtered films on planar substrates.

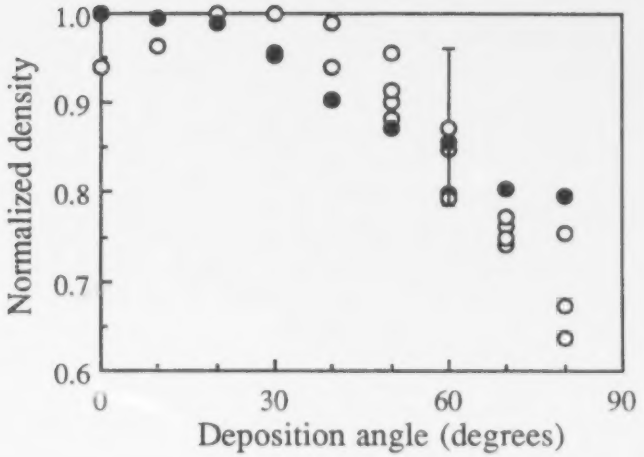


Figure 5.1. Density of sputtered tungsten; measured O simulated ●.

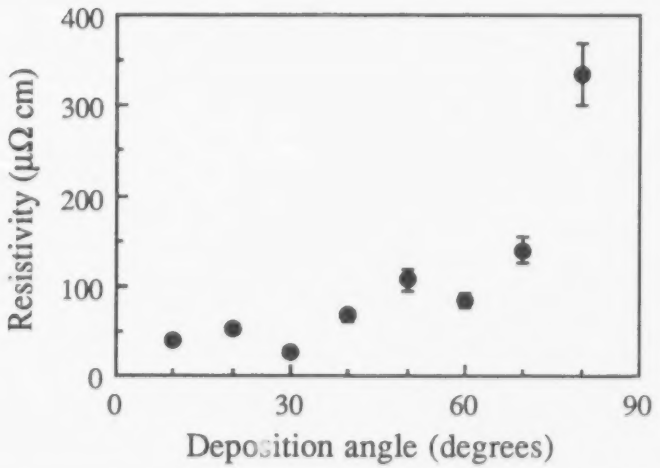


Figure 5.2.. Resistivity of sputtered tungsten.

### 5.1.2 Etch Rate Measurements

As with the Mo films described in Chapter 4, a common grain boundary definition etch was chosen to define the porous regions of the deposited film. Etching is frequently used in metallurgy to reveal general microstructure by etching grain boundaries and providing contrast between adjoining grains or phases.[112] For thin metal films deposited at low substrate temperature, grains are readily identified as discrete columns in a cross-sectional photograph. Films will then etch rapidly where the film is porous and the etchant has access to a large surface area, which is in regions where the substrate normal forms a large angle with the vapour source normal.

Because the etching proceeds along boundaries and pores, rather than from the top surface only, the etch rate is difficult to measure. Attempts to measure change in film thickness with etch time showed no discernible change in thickness up to the time when the film was removed. Measurements were therefore made of the clearing time, $t_r$ ,or time per unit thickness to remove films with previously determined density and thickness. Density change with time is then given approximately by considering density as a function of $t_{ro}$-$t_r$ where $t_{ro}$ is the time per unit thickness to clear a normal incidence or maximum density film. Time measurements were made for different film thicknesses to verify clearing time per unit thickness is approximately constant for a given film density. The quantity $t_{ro}$-$t_r$ is referred to as time per unit thickness rather than inverse etch rate since this work relates etch time to density rather than thickness. From the density-time plot the functional form of the density etching algorithm and the density etch rate can be obtained.

To obtain an expression for etch rate, $\ln(\rho_o-\rho)$ was plotted against time $t_{ro}$-$t_r$, where $\rho_o$ is the maximum density. This is shown in Figure 5.3. The plot indicates the expected behavior, with the density deviation from the maximum density growing as the time increases. The resulting trend is fairly linear, indicating an exponential expression is reasonably accurate as well as being mathematically convenient for a difference equation. The resulting expression is

$$\rho(t)=\rho_o-ce^{rt} \qquad 5.1$$

The curve fit shown gives $c\approx0.03$ and $r\approx294$. The very small value for c indicates that a reasonable approximation for the simulation is to replace $\rho_o$ by $\rho_o+c$, which gives the desired behavior at t=0, without significantly deviating from the experimental data. This gives a difference equation for the etch rate simulation

$$\rho_{i,j,k+1} = \rho_{i,j,k} - r\,(\rho_o+c-\rho_{i,j,k}) \qquad 5.2$$

where i,j is the location in the density array and k is the iteration number. The expression found here indicates that low density regions of a film will etch most rapidly, as expected.

This behavior was used to demonstrate the density variation in films sputtered over topography. Trenches approximately 1 μm deep, 1.5 μm wide, and several millimeters long were fabricated in oxide on a silicon wafer. A tungsten film 1 μm thick was then deposited using sputtering conditions identical to those used for the earlier films. Samples were cleaved following deposition to expose a cross-section of the

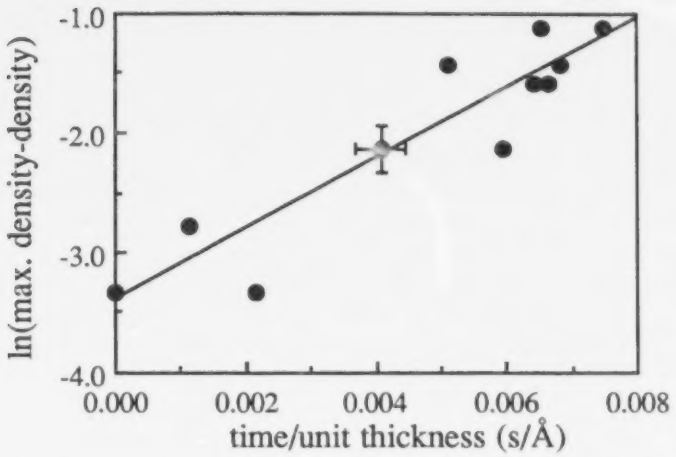


Figure 5.3. Etch rate for obliquely deposited W in $K_3Fe(CN)_6$ and NaOH. A typical uncertainty is shown.

trench structure. The films were etched in a solution of $K_3Fe(CN)_6$ and NaOH using ultrasonic agitation to prevent the trench from filling with residue. The resulting etch times were short due to the intense agitation, and samples were rinsed in water following etching. A thin coating of sputtered gold was applied prior to cross-sectional scanning electron microscope (SEM) photography.

Via sidewall problems are clearly shown in Figure 5.4 a), a SEM photograph of a W film deposited over a trench in $SiO_2$. Since the ratio of substrate temperature during deposition to melting temperature for tungsten is small, $T_s/T_m<0.1$, columnar zone 1 structure was expected and can easily be seen. It is most obvious on the steep 80° sidewalls where the structure shows definite voids between coarse columns. The horizontal sections of the film appear much more dense and finely structured. An etchant will contact a much larger film surface area on the sidewalls and should etch more rapidly than on the horizontal surfaces.

Figure 5.4 b) shows a similar film after only 2 seconds of immersion in the etching solution with ultrasonic agitation. The film on the sidewalls appears to have been mostly removed, with some material remaining beyond the depth of field and therefore out of focus. The other regions of the film appear largely unaffected by the etching. Figure 5.4 c) shows a film after 10 seconds of etching, and the sidewalls of the trench have been completely cleared of metal. The remaining film shows some deep void formation, but very little change in thickness, supporting the earlier comment that etching proceeds in voids and along grain boundaries until the film is free from the substrate.

a) as deposited

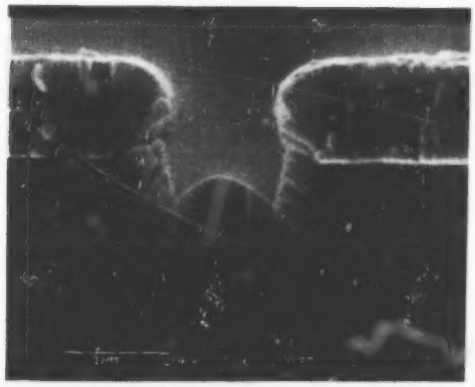

b) 2 s etch

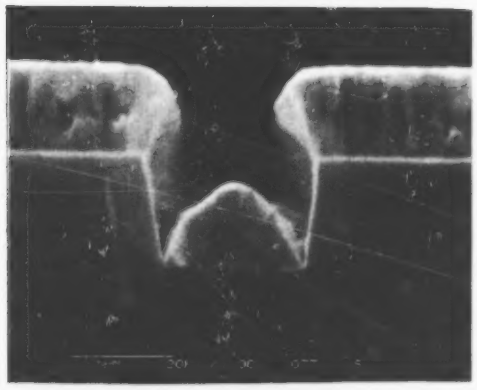

c) 10 s etch

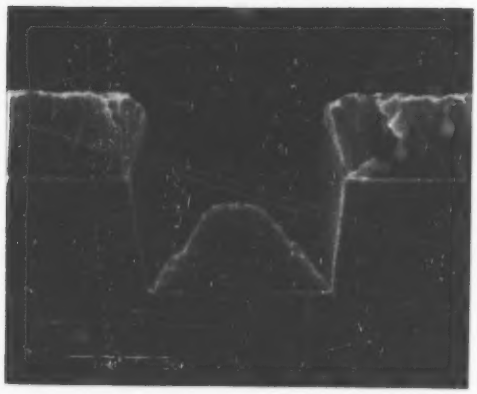

Figure 5.4. Wet etching of W deposited over a trench.

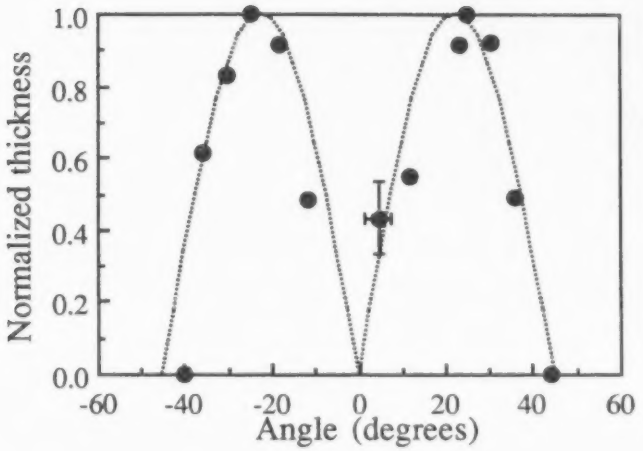


Figure 5.5. Angular distribution used for sputtering simulations. Points are measured with a typical uncertainty given. The dotted curve is $|\sin(4\theta)|$ between $\pm$ 45°.

### 5.1.2 Simulation Results

To generate an accurate simulation of this film using SIMBAD, a realistic angular distribution for the material flux from the magnetron source was required. Film profiles have been found to be quite sensitive to the distribution used. The distribution was found to resemble an image of the erosion track on the magnetron target surface. The technique for measuring this distribution was to place a mask with a small hole at a normal target substrate spacing from the source. A substrate was placed behind this at a distance of 2 cm which allowed reasonable resolution and adequate deposition rate. The substrate was masked with photoresist lines prior to deposition. The photoresist was removed after the film was deposited, leaving a step for profilometry, which provided the distribution information. The distribution measured in a direction perpendicular to the trench orientation is shown in Figure 5.5. No measurement was possible at 0° since a photoresist line interrupted the film at this location. As illustrated in the figure, $|\sin(4\theta)|$ between $\pm$ 45° was found to be an excellent approximation to the measurements except at normal incidence, and this is the distribution used for the simulations. More realistically for a long trench in the substrate a three-dimensional distribution compressed into two dimensions should be used, but the simple function used here provides good results and is certainly an improvement on the cosine distribution previously assumed for sputtering simulations.[113]

The disc plot consisting of 45 000 discs, generated using this distribution, is shown in Figure 5.6 a). Microstructural details in plots such as this have previously been discussed.[114] It is sufficient to note the general similarity to the real films and

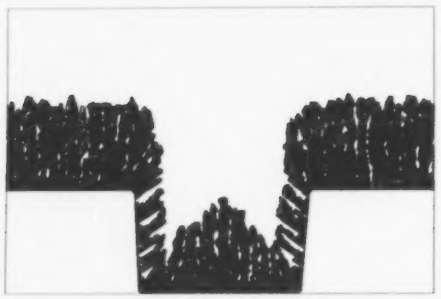

a) film plot

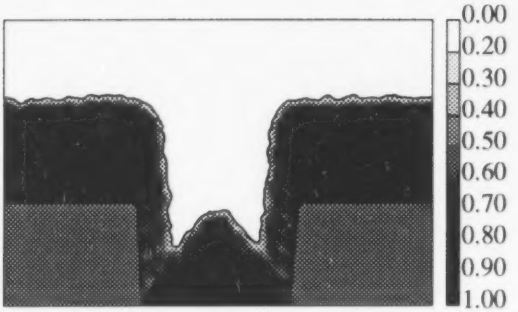


b) density plot

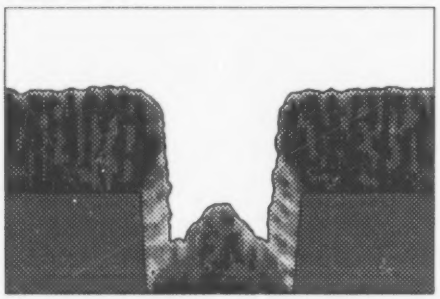

c) partly etched

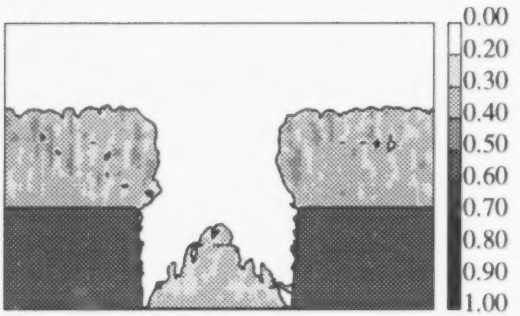


d) etched to removal of sidewall coverage

Figure 5.6. SIMBAD simulation of deposition and wet etching of sputtered W.

the increased void size on the via sidewalls. If we define step coverage as the ratio of the thinnest film coverage on the sidewall to the thickness on a horizontal section, we find both the simulation and real film give a value of about 0.4. Since step coverage is sensitive to incident angular distribution, this indicates that the chosen distribution is fairly accurate.[105] Of course the etching experiment described here has shown that surface profiles and step coverage are not the only factors determining interconnect quality. While this step coverage would normally be acceptable, the porous quality of the film can lead to resistivity an order of magnitude higher than in the rest of the film. This is emphasized by a SIMBAD density plot, as in Figure 5.6 b).

Figure 5.6 b) is a gray scale density profile calculated from 10 films similar to the one shown in Figure 5.6 a). It shows the porous regions on the sidewalls of the via as lighter gray regions, and the more dense regions as a fairly uniform dark gray. Using this profile, the etching expression Equation 5.2 was applied, where the etch rate in any cell is proportional to the deviation from maximum density. The results are printed at each step and are shown in Figure 5.6 c) and 5.6 d). Even in the 10 film average there is some evidence of the columnar structure in the density plot, and the etching algorithm reveals this structure on the via sidewalls. As etching continues, portions of film become disconnected from the substrate and these are removed. After only a few steps the density profile resembles the etched tungsten film of Figure 5.4. Direct comparisons of etching time are not possible since different etchant concentrations were used in the etch rate measurement and the etching of the films over vias. While the algorithm used is very basic, it reproduces both the film profile and the etching process quite well. Notice that the etching simulation, like the real etching experiment, does not greatly affect film thickness until portions are actually removed.

A demonstration of the variation of density in films deposited over vias has been presented by post-deposition wet etching to reveal low density regions. SIMBAD simulations of the via shape, combined with a simple density-based etching algorithm agree well with the results. Although the film shows reasonable step coverage, it represents a poor interconnect due to the high resistivity expected in the porous sidewall region. This investigation into the wet etching process suggests the possibility that a model such as SIMBAD may be useful for the study of a variety of microelectronics processing techniques. As an example we will consider the common method of etching using a flourine-based plasma.

## 5.2 Plasma Etching†

Many steps in integrated circuit (IC) manufacture require precise control of etching profiles. Wafers are covered with a layer of material which is selectively removed by etching through a mask, leaving, for example, holes in a thermal oxide for diffusions or lines of metal for interconnects between devices. Demands for reduced device size require high quality deposited films and control over etching to ensure adequate performance.[115]

---

† The material in this section has been accepted for publication as:

R.N. Tait, S.K. Dew, T. Smy, and M.J. Brett, J. Vac. Sci. Technol. A**10**(4), (1992).

Several types of etching are commonly used. Wet chemical etching using aqueous solutions is used because it is economical when applicable, however plasma etching and reactive ion etching (RIE) are used for fine geometry (<3μm) applications. Most IC etching requires material removal in selected regions, etching completely through thin amorphous or fine-grained polycrystalline films. Wet and plasma etching processes are generally isotropic in these materials. Etching proceeds at the same rate in all directions provided the material to be removed is also isotropic. RIE etching is anisotropic, as reactive ions arrive in a beam normal to the substrate surface, and scattering is limited due to low operating pressures. The anisotropy is due to both sputtering and chemical removal of material stimulated by the ion energy. Both processes are localized to regions receiving ion flux.[19]

Because these etching processes depend on the incident flux of reaction precursors, they can be simulated from a geometric perspective. The string model algorithm has been very successful in representing both film deposition and etching as geometric processes.[33,116,117] This model represents a film surface as a series of points joined by straight line segments. The final film profile is determined by the motion of these points which is a function of local variables. For example, an isotropic etch advances all points at a constant rate in a direction perpendicular to the surface, while an anisotropic etch advances points at a rate proportional to the cosine of the angle between the flux and the surface normal. Rates and selectivity are empirical, and the film material is assumed to be isotropic. Empirical rates work quite well, but simulation is limited to simple geometries[118] and the assumption about film isotropy is questionable. Thin films, in particular those deposited by physical vapour deposition, exhibit microstructure which changes properties from those of the bulk material.[5] Because of this, metallization layers and other films deposited over topography are known to exhibit local variations in density at via sidewalls and corners.[113] These variations can adversely affect important properties such as resistivity, and result in unexpected etch profiles. The consideration of microstucture effects is essential to improving simulation results.

Because of the similarity between deposition and etching processes, SIMBAD can be extended to include plasma and ion-assisted etching based on geometrical factors. This section demonstrates that the microstructure of films deposited in vias or trenches results in anisotropic etching predictions from SIMBAD using a model for pure plasma etching. Confirmation of these results is demonstrated using tungsten (W) films sputtered over trenches in silicon dioxide and etched in a $CF_4/O_2$ plasma.

### 5.2.1 Experimental work

To form films for etching studies, tungsten was DC sputtered from a 12.5 by 20 cm planar magnetron source at 250 W and 1.5 Pa argon pressure. Adhesion and stress characteristics of the films were found to improve at high pressure and low power, most likely due to reduced neutral bombardment of the substrate.[110] Substrates included trenches 1.8 μm wide with 80° sidewalls and an aspect ratio of 0.6. The pattern was formed in thermal oxide on a silicon wafer, and was covered by the sputtered high purity (99.95%) tungsten to a thickness of 0.9 μm. Tungsten was used because of its pronounced columnar structure and its relevance to VLSI processing. High melting point, electromigration resistance, and stability on oxides and nitrides make this a desirable metallization material.

In addition to these properties, refractory metals such as tungsten are easily etched in flourine-based plasmas.[119] Following the sputter deposition, films were cleaved and then etched in a TEGAL 915 barrel-style plasma etcher using $CF_4$ with 8% $O_2$ at 50 Pa and 200 W RF power. This resulted in an etch rate of about 180 nm/min for planar films. Etch times were increased in 10 second steps to show the etching progression. By viewing cross-sections of the trenches with a scanning electron microscope (SEM), the effect of film microstructure on an isotropic etching process was observed.

### 5.2.2 Simulation

A model of the plasma etching process can be developed based on the existing film deposition model. The model has been extended to include the effects of ion bombardment such as film resputtering and redeposition, ion reflection, and ion-induced diffusion. This allows simulation of more complicated deposition processes such as RF bias sputtering,[120] and also provides the tools to develop a plasma etching model.

To model plasma etching from a geometric standpoint, a representation of transport of the active gas components to the film surface must be developed. Using SIMBAD, the active gas species are represented by discs which are referred to as etchant discs. To be consistent with the film discs, each etchant disc represents an average of a number of etchant species. Even at common etching pressures of around 50 Pa, the mean free path of a gas molecule will be significantly larger than the simulation dimensions; hence gas phase collisions in the simulation can be neglected.[121] In a plasma etch such as this, removal of film material is attributed to the presence of free reactive atoms which reach the substrate by diffusion. The flux of reactive species can therefore be represented by a cosine distribution near the substrate. Etchant discs are released from the top of the simulation space with this angular distribution and follow linear, collision-free trajectories until contact is made with a film disc. Upon reaching the film surface the etchant disc has a fixed probability of reacting and removing a film disc, a parameter referred to as the reaction coefficient. If the etchant disc fails to react, it is desorbed from the surface according to a thermal cosine distribution[18] and proceeds in a linear trajectory until it once again contacts the film surface, or it exits the simulation space. This model ignores local effects on the reaction probability such as multiple etchant species and reaction paths. Diffusion of etching products away from the substrate is not modeled.

Clearly the reaction coefficient is an essential parameter in this model. It can be estimated within an order of magnitude based on etch rate measurements in a plasma with a known concentration of active gas species. For W in a $CF_4/O_2$ plasma, the etching is considered to be mainly due to free F atoms. While plasma properties will depend on the reactor geometry, some general estimates of the concentration [F] can be made. Using gas phase titration methods, [F] has been found to be about $10^{15}/cm^3$ for a 200 W discharge at 45 Pa of $CF_4$ with 8% $O_2$.[122] This corresponds to an impingement rate on a substrate of about $4x10^{19}/cm^2s$ using the kinetic theory of gases. In the etching experiment described above, the number of W atoms removed from the horizontal substrate sections, based on a film close to bulk density, was about $2x10^{16}/cm^2s$. Using this information and assuming simple reaction paths, the

a) as deposited

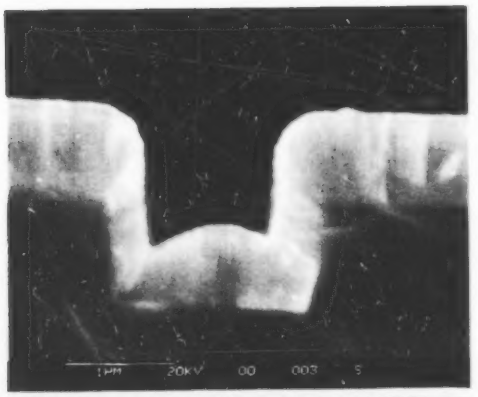


b) 30 s etch

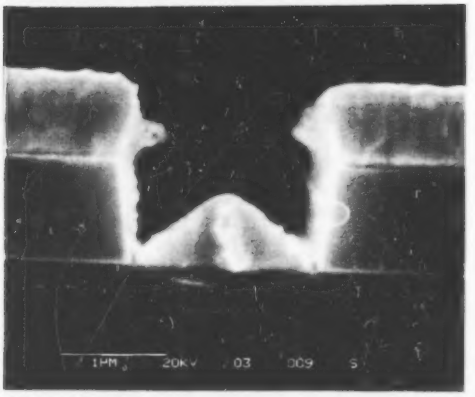


c) 60 s etch

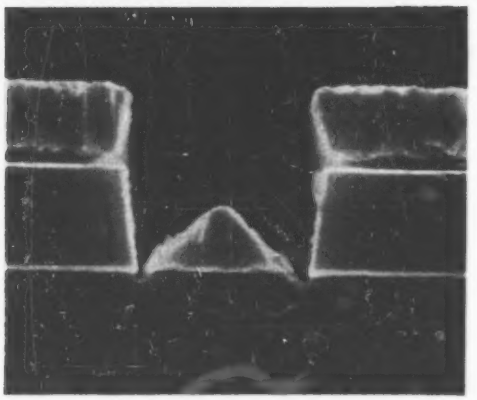

Figure 5.7. Plasma etching of W deposited over a trench.

probability that an etchant disc removes a film disc should be about $10^{-3}$. An etchant disc therefore will pause at many sites before reaction actually occurs, and this results in an isotropic etching process. With this value of reaction coefficient, a viable model of plasma etching can be implemented and tested.

### 5.2.3 Results and Discussion

To demonstrate the application of this model to plasma etching of metal films deposited over topography, the W films are shown at various stages in the etching process and are compared with the simulation results. Figure 5.7 a) shows the W film as deposited, and the columnar microstructure is just visible. For the sputtering conditions, $T_s/T_m$ = 0.1 and P = 1.5 Pa, the film is expected to be voided and columnar.[15] The void structure is enhanced on the via sidewalls as the average angle of incident flux is large, and shadowing is significant. The shadowing effect and competition of columns growing from the trench base and sidewalls combine to create reduced film density regions on the sidewalls.[85]

These reduced density regions cause anisotropic etching of the film profile when an isotropic etching process is used. Figure 5.7 b) and c) show W films after 30 seconds and 60 seconds of etching. The etch rate on the sidewalls is much higher than on the horizontal film sections. A rough measurement of the etch rate from the photographs indicates that the sidewalls etch about twice as fast as the rest of the film. The increased etch rate and reduced coverage on the sidewall cause the film to almost clear from this region after only 30 seconds of etching. After 60 seconds the sides are clear and etching in the trench corners has begun to advance into the substrate. The etching has also started to penetrate the interface between the W and the $SiO_2$, and the film is likely to delaminate with longer etch times.

This etching behavior is successfully predicted by the SIMBAD simulations. Figure 5.8 a) shows a film composed of about 40 000 discs deposited using the experimentally measured angular distribution described in §5.1 for the planar magnetron source.[123] The general features of the sputtered W film are well reproduced, including the step coverage and the increased porosity on the trench sidewalls. This film is used as a starting point for the etching simulation.

To compare the etching simulation with the real films, the etch rate of the horizontal film sections was used to calibrate times. Figure 5.8 b) shows the simulated film after 30 seconds of etching. As with the real film, the most noticeable changes are on the trench sidewalls. After 60 seconds the film is removed from the sidewall region except at the lower corners,as shown in Figure 5.8 c) and shows good general agreement with the experimental results. The lack of etching in the corners differs from the experimental result, but it can be attributed to two aspects of the etching simulation related to the penetration of etchant into these regions. The first problem is with surface diffusion of the etchant. There is little known about the motion of an etchant once it has been adsorbed on a surface, and for the simulation, etching was assumed to occur near the point of adsorption. If diffusion of the etchant over some distance occurs, it can penetrate between columns and reach regions isolated from direct flux. The second possibility is that etching of the bottom corners is a three-dimensional phenomenon, while the simulation is only two-dimensional. The extra dimension could provide access for the etchant to regions which are closed off to flux in

a) as deposited

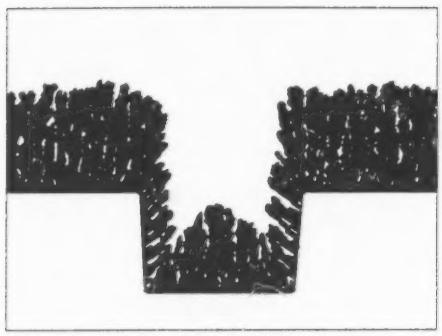

b) 30 s etch

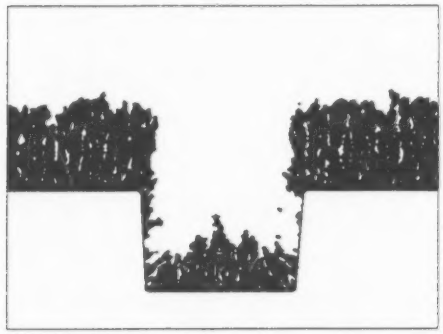

c) 60 s etch

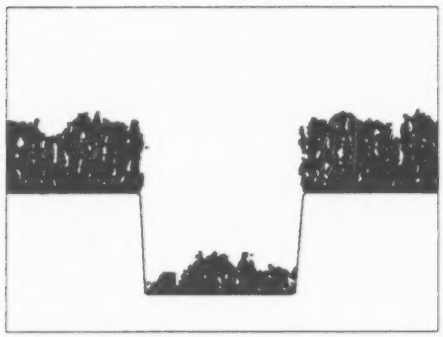

Figure 5.8. Plasma etching simulation of W deposited over a trench.

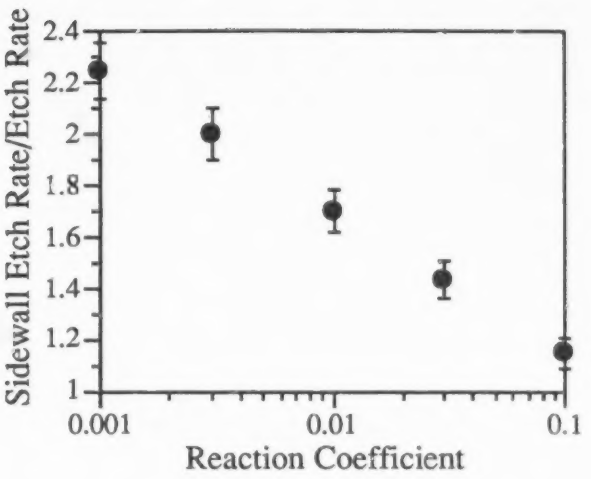


Figure 5.9. Effect of reaction coefficient on etch rates.

the simulation. Another apparently anomalous feature of the etching simulation is the production of islands of discs isolated from the rest of the film. This is not physically unreasonable, as etching may free sections of film which will subsequently be removed.

In addition to the good general agreement of etching profiles between simulated and experimental data, there is good agreement of relative etch rate results. Figure 5.9 shows the effect of increasing reaction coefficient on etch anisotropy. The ratio of etch rate on the sidewalls to etch rate on the horizontal film sections is close to the experimentally observed value only for a reaction coefficient near 0.001. The process is actually quite isotropic at this value, but the reduced film density on the via sidewall makes the resulting rates anisotropic. As the reaction coefficient is increased, computation speeds up significantly but the anisotropy is reduced, and the etching process begins to resemble a reverse deposition as the coefficient approaches unity. The most accurate practical simulations therefore utilize a low reaction coefficient and are restricted to two dimensions to control simulation time.

The etching simulations presented here have provided several interesting results. Both the wet and plasma etching processes are classified as isotropic, and both give very similar results. The wet etching was used to demonstrate that the the predictions provided by the deposition simulations were accurate in their prediction of low density regions, and that these predictions are important in anticipating the performance of metallization. The plasma etching results indicate that a model like SIMBAD can provide information on processes involving complicated chemical mechanisms, provided material transport is a limiting factor. This implies SIMBAD can be used to model many processes other than physical vapour deposition, particularly if it can be linked to other specialized simulators.

# Chapter 6: Conclusions

This thesis has now presented ballistic deposition modeling of thin film growth and its use in the simulation of thin films for metallization applications. The work has progressed from a brief survey of approaches to thin film modeling to describe how ballistic deposition accurately reproduces the essential properties of thin film microstructure. A derivation of the expected functional form for column structure angle as a function of deposition angle was used to show the shortcomings of the empirically derived tangent rule, and an explanation of structural anisotropy in the film plane was given based on a 3-D ballistic deposition simulation. Most importantly, films deposited over topography have been studied, and the predictions of density variation provided by SIMBAD have been verified through measurements of density and etch rate for these films. Finally, the potential for expansion of SIMBAD to model a variety of processes has been demonstrated by modeling the plasma etching process. Three things now remain to be clarified in order to summarize the work. First of all, the importance of this simulation work to the microelectronics industry must be explained. The originality of the technique must be clearly defined. Finally, the direction of this work in the future should be predicted.

## 6.1 Application

The use of thin film technology continues to grow in many areas of manufacturing. With this growth has come the realization that an understanding of film microstructure is essential to predicting the optical, magnetic and electrical characteristics of films. Some examples of the many applications of simulation of non-equilibrium growth processes are provided in the Appendices 3-5.

Of course, the application of interest here is the use of thin metal films in microelectronics. The model presented here predicts features of such films deposited within a limited range of deposition parameters commonly used. This is of great interest to the metallization engineer mainly for economic reasons. IC production is a large and competitive business, and any small increase in yield or decrease in feature size can translate to substantial production cost savings for a manufacturer. What SIMBAD does is help the engineer in locating the most likely problem regions in his metallization geometry.

Clearly SIMBAD covers only a small part of the manufacturing process, but integration with simulation software covering other aspects of processing could produce a powerful design tool.[124] The real test for the usefulness of this technique will come with the distribution of the software to industrial users.

## 6.2 Originality

This project is the result of the work of many individuals, and their work must be differentiated from the results presented here. It has already been pointed out that the basic concepts for SIMBAD had been established prior to the commencement of work for this thesis. Of course, software development was undertaken in the course

of research, but the software is constantly changing and developing and programming should not be the focus of this thesis. I will point out however, that my contribution to code writing includes not just general input during development, but specifically: i) the algorithm for generating the hailstone growth in Appendix 5, including the first attempts at including a variable diffusion length (although not the recursive method), ii) the on-lattice 3-D growth algorithm described in Chapter 3, and the associated plotting programs, and iii) the density-based etching algorithm in Chapter 5. Much more important than these achievements are the experimental verifications provided by this work, which are laid out as follows.

SIMBAD has been shown to effectively predict several basic properties of thin films, which have been experimentally observed. Column angle predictions have been explained by a simple theory, which has been shown to be equal or superior to the empirical tangent rule in its agreement with experimental results. By extending the model to three dimensions, film-plane anisotropy has been shown to be at least partially due to simple shadowing effects. Finally, density predictions of SIMBAD for planar films have been shown to agree with experimentally evaporated and sputtered films even for fairly short diffusion lengths.

It is the density predictions that make this model useful for applications involving films deposited over topography. This work presents the first comparisons of SIMBAD density results with real evaporated and sputtered films deposited over topography. More importantly, the wet etching of metal films provides clear evidence that the density variation due to topographical features is a real and significant factor in determining the quality of interconnections in VLSI circuits.

The extension of the model to study both wet and plasma etching demonstrates the potential of this approach for extension to modeling of other VLSI manufacturing processes. Of course it also reveals the importance of microstructure on etching profiles of polycrystalline films. This is a fairly obvious effect of film microstructure that is overlooked by those used to etching single crystal or bulk material.

This thesis thus demonstrates for the first time how a simple ballistic deposition model can provide surface, microstructure, and density profiles of films deposited by physical vapor deposition over topography. It shows how the results of this model compare favorably with observable properties of real films, and how these predictions can have important consequences for VLSI processing.

## 6.3 Future Work

The individuals working on this project are exceptional in their ability to generate ideas and quickly attack the associated problems. As a result, many of the logical extensions of this work have been proceeding in parallel with this research. To name a few of the projects, work has now been done on bias sputtering, chemical vapor deposition, high temperature sputtering, and current and temperature distributions in interconnections. Also, studies are proceeding on a variety of related projects which will not be mentioned here.

In spite of this large number of SIMBAD projects currently complete or underway, there are still avenues open for further research. Fundamental projects include an improved 3-D SIMBAD which will become more feasible as computing

abilities expand. As discussed in Chapter 3, an off-lattice 3-D simulation would be useful but it is difficult to efficiently execute. A more applied project would involve modeling of reactive ion etching, an important process for VLSI processing.

More generally, this simulation technique would benefit greatly from a better relationship to physical parameters of both the deposition process and the resulting films. Work has already been undertaken by others to relate the incident angular distribution to deposition parameters. Most film properties, such as resistivity, are related to the order in the film, in many cases to the density. One approach is to empirically relate density to the property of interest. With these additions, SIMBAD will become tremendously useful as a metallization process simulation program.

## References

1 M. Faraday, Phil. Trans. **147**, p. 145 (1857).

2 H.A. Macleod, *Thin Film Optical Filters*, McGraw-Hill, New York, (1989).

3 C.R.M. Grovenor, *Microelectronic Materials*, IOP Publishing Ltd., Bristol, (1989).

4 J.M. Nieuwenhuizen and H. B. Haanstra, "Microfractography of thin films", Philips Technical Review **27** (3), p. 87 (1966).

5 H.J. Leamy, G.H. Gilmer, and A.G. Dirks, "The microstructure of vapor deposited thin films", Curr. Top. Mater. Sci. 6, p. 309 (1980).

6 B.A. Movchan and A.V. Demchishin, "Study of the structure and properties of thick vacuum condensates of nickel, titanium, tungsten, aluminum oxide, and zirconium dioxide", Fiz. Metal. Metalloved. **28** (4), p. 653 (1969).

7 J.P. Krusius, "Process modeling for submicron complementary metal-oxide-semiconductor very large scale integrated circuits", J. Vac. Sci. Tech. A **4** (3), p. 905 (1986).

8 S.P. Murarka, "Interactions in metallization systems for integrated circuits", J.Vac. Sci. Technol. B **2** (4), p. 693 (1984).

9 J.E. Sanchez, L.T. McKnelly, and J.W. Morris, "Morphology of electromigration-induced damage and failure in Al alloy thin film conductors", J. Elect. Mater. **19** (11), p. 1213 (1990).

10 J.R. Lloyd, "Role of copper in electromigration lifetimes of aluminum alloy conductors", Appl. Phys. Lett. **57** (11), p. 1167 (1990)

11 R. Kirchheim and U. Kaeber, "Atomistic and computer modeling of metallization failure of integrated circuits by electromigration", J. Appl. Phys. **70** (1), p. 172 (1991).

12 S.M. Sze,ed., *VLSI Technology*, McGraw-Hill, New York, (1983).

13 H.P. Bader and M.A. Lardon, "Planarization by radio-frequency bias sputtering of aluminum as studied experimentally and by computer simulation", J. Vac. Sci. Tech. A **3** (6), p. 2167 (1985).

14 D. Culver and G. Klein, "Modeling of metal step coverage for minimum feature size contacts and vias", 1985 VLSI Multilevel Interconnection Conference, p. 399 (1985).

15 J.A. Thornton, "Influence of apparatus geometry and deposition conditions on the structure and topography of thick sputtered coatings", J. Vac. Sci. Technol. **11** (4), p. 666, (1974).

16 J.A. Thornton, "The microstructure of sputter-deposited coatings", J. Vac. Sci. Technol. A **4** (6), p. 3059 (1986).

17 J.A. Thornton, "High rate thick film growth", Ann. Rev. Mater. Sci. **7**, p. 239 (1977).

18 L.I. Maissel and R. Glang, *Handbook of Thin Film Technology*, McGraw-Hill, New York, (1983).

19 S.M. Rossnagel, J.J. Cuomo, and W.D. Westwood eds., *Handbook of Plasma Processing Technology* Noyes Publications, Park Ridge, New Jersey, (1990).

20 W.R. Runyan and K.E. Bean, *Semiconductor Integrated Circuit Processing Technology*, Addison-Wesley,New York, (1990).

21 K.W. Harper and R.E. Jones Jr., "A comparison of three-dimensional and two-dimensional simulations of contact step coverage", J. Vac. Sci. Technol. A **5** (3), p. 333 (1987).

22 S. Mehta, S. Mittal, A. Haranahalli, and D. Ranadive, "Blanket CVD tungsten interconnection for VLSI technologies", 1986 Proc. IEEE VLSI Multilevel Interconnection Conf., p. 418 (1987).

23 K. Hieber and M. Stolz, "Tungsten contact hole filling in a high vacuum CVD system", 1987 Proc. IEEE VLSI Multilevel Interconnection Conf., p. 216 (1988).

24 G. Mbise, G.B. Smith, and C.G. Granquist, " High resolution studies of columnar growth in obliquely deposited metal films on glass", Thin Solid Films **174**, p. L123 (1989).

25 I.J. Hodgkinson and P.W. Wilson, "Microstructural-induced anisotropy in thin films for optical applications", CRC Crit. Rev. Sol. State Mat. Sci. **15** (1), p. 27 (1988).

26 J.G.W. van de Waterbeemd and G.W. van Oosterhout, "Effect of the mobility of metal atoms on the structure of thin films deposited at oblique incidence", Philips Res. Repts. **22**, p. 375 (1967).

27 S. Lichter and J. Chen, "Model for columnar microstructure of thin solid films", Phys. Rev. Lett. **56** (13), p. 1396 (1986).

28 R. Fiedler and G. Schirmer, "Sauelenwachstum bei aufgedampften Schichten", Thin Solid Films 167, p. 281 (1988).

29 K. Kinosita and M. Nishibori, "Porosity of $MgF_2$ films-evaluation based on changes in refractive index due to adsorption of vapors", J. Vac. Sci. Tech. **6**, p. 730 (1969).

30 W.L. Bragg and A.B. Pippard, " The form birefringence of macromolecules", Acta Crystallogr. 6, p. 865 (1953).

31 H.A. Macleod, "Structure related optical properties of thin films", J. Vac. Sci. Technol. A **4** (3), p. 418 (1986).

32 A.R. Neureuther, "Process modeling and simulation tools", J. Vac. Sci. Technol. A **4** (3), p. 912 (1986).

33 W.G. Oldham, A.R. Neureuther, C. Sung, J.L. Reynolds, S.N. Nandgaonkar, "A general simulator for VLSI lithography and etching processes: Part II - application to deposition and etching", IEEE Trans. Elect. Dev. ED-**27** (8), p. 1455 (1980).

34 C.H. Ting and A.R. Neureuther, "Applications of profile simulation for thin film deposition and etching processes", Sol. State Technol. **25** (2), p. 115 Feb. (1982).

35 E.W. Scheckler, "Algorithms for Three-Dimensional Simulation of Etching and Deposition Processes in Integrated Circuit Fabrication", Ph.D. Dissertation, Electronics Research Laboratory, University of California, Berkeley, Memorandum No. UCB/ERL M91/99 (1991)

36 J. Ignacio Ulacia F. and J.P. McVittie, "A two-dimensional computer simulation for dry etching using Monte-Carlo techniques", J. Appl. Phys. **65** (4), p. 1484 (1989).

37 T. Thurgate, "Segment Based Etch Algorithm and Modeling", IEEE Trans. Computer-Aided Design of IC's and Systems, CAD-**10** (9), p. 1101 (1991).

38 G.S. Bales and A. Zangwill, "Macroscopic model for columnar growth of amorphous films by sputter deposition", J. Vac. Sci. Technol. A **9** (1), p. 145 (1991).

39 D.J. Srolovitz, A. Mazor, and B.G. Bukiet, "Analytical and numerical modeling of columnar evolution in thin films", J. Vac. Sci. Technol. A **6** (4), p. 2371 (1988).

40 A. Mazor, B.G. Bukiet, and D.J. Srolovitz, " The effect of vapor incidence angle upon thin-film columnar growth", J. Vac. Sci. Technol. A **7** (3), p. 1386 (1989).

41 C. Tang, S. Alexander, and R. Bruinsma, "Scaling theory for the growth of amorphous films", Phys. Rev. Lett. **64** (7), p. 772 (1990).

42 J. Salik, "Computer simulation of thin film nucleation and growth.", J. Appl. Phys. **59** (10), p. 3454 (1986).

43 J. Salik, "Computer simulation of thin film nucleation and growth", J. Appl. Phys. **57** (11), p. 5017 (1985).

44 B.J. Bartholomeusz, K.H. Müller, and M.R. Jacobson, "Computer simulation of the nucleation and growth of optical coatings", SPIE **821** (1987).

45 B. Yang, L.J. Pilion, J.E. Yehoda, K. Vedam, and R. Messier, Phys. Rev. **36**, p. 6206 (1987).

46 K.H. Müller, "Stress and microstructure of sputter-deposited thin films: Molecular dynamics investigations", J. Appl. Phys. **62** (5), p. 1796 (1987).

47 K.H. Müller, "Dependence of thin-film microstructure on deposition rate by means of a computer simulation", J. Appl. Phys. **58** (7), p. 2573 (1985).

48 K.H. Müller, "Role of incident kinetic energy of adatoms in thin film growth", Surf. Sci. Lett. **185**, p. L375 (1987).

49 K.H. Müller, "A computer model for postdeposition annealing of porous thin films", J. Vac. Sci. Technol. A**3** (6), p. 2089 (1985).

50 K.H. Müller, "Monte Carlo calculation for structural modifications in ion-assisted thin film deposition due to thermal spikes", J. Vac. Sci. Technol. A**4** (2), p. 184 (1986).

51 K.H. Müller, "Model for ion-assisted thin-film densification", J. Appl. Phys. **59** (8), p. 2803 (1986).

52 K.H. Müller, "Modelling ion-assisted deposition of $CeO_2$ films", Appl. Phys. A **40**, p. 209 (1986).

53 K.H. Müller, "Ion-beam-induced epitaxial vapor-phase growth: A molecular-dynamics study", Phys. Rev. B **35** (15), p. 7906 (1987).

54 K.H. Müller, R.P. Netterfield, and P.J. Martin, "Dynamics of zirconium oxide thin-film growth and ion-beam etching", Phys. Rev. B **35** (6), p. 2934 (1986).

55 K.H. Müller, "Cluster-beam deposition of thin films: A molecular dynamics simulation", J. Appl. Phys. **61** (7), p. 2516 (1987).

56 P.A. Deymier and R.B. Sargent, "Molecular-dynamics simulation of thin-film growth and relaxation", Proc. SPIE **1324**, p. 120 (1990).

57 W.D. Luedtke and U. Landman, "Preparation, structure, dynamics, and energetics of amorphous silicon: a molecular-dynamics study", Phys. Rev. B **40** (2), p. 1164 (1989).

58 P.A. Taylor and B.W. Dodson, "Simulation of atomistic crystal growth from the vapour phase", Mat. Res. Soc. Symp. Proc. **77**, p. 175 (1987).

59 M.J. Vold, "Computer simulation of floc formation in a colloidal suspension", J. Colloid Sci. **18**, p 684 (1963).

60 D.N. Sutherland, "Comments on Vold's simulation of floc formation", J. Colloid Sci. **22**, p 300 (1966).

61 D. Henderson, M.H. Brodsky, and P. Chaudhari, "Simulation of structural anisotropy and void formation in amorphous thin films", Appl. Phys. Lett. **25** (11), p. 641 (1974).

62 S. Kim, D.J. Henderson, and P. Chaudhari, "Computer simulation of amorphous thin films of hard spheres", Thin Solid Films **47**, p. 155 (1977).

63 M. Sikkens, I.J. Hodgkinson, F. Horowitz, H.A. Macleod, and J.J. Wharton, "Computer simulation of thin film growth: applying the results to optical coatings", Opt. Eng. **25** (1), p. 142 (1986).

64 R.B. Sargent, "Effects of surface diffusion on thin-film morphology: a computer study", Proc. SPIE **1324**, p. 13 (1990).

65 B.J. Bartholomeusz and T.K. Hatwar, "Modeling studies of rare earth-transition metal optical recording media in relation to experiment", Thin Solid Films **181**, p. 115 (1989).

66 P. Meakin, "Ballistic deposition onto inclined surfaces", Phys. Rev. A **38** (2), p. 994 (1988).

67 P. Meakin, P. Ramanlal, L.M. Sander, and R.C. Ball, "Ballistic deposition on surfaces", Phys Rev. A **34** (6), p. 5091 (1986).

68 P. Ramanlal and L.M. Sander, "Theory of ballistic aggregation", Phys. Rev. Lett. **54** (16), p. 1828 (1985).

69 D. Bensimon, B. Shraiman, and L.P. Kadanoff, "Mean field theory for a ballistic model of aggregation", in *Kinetics of Aggregation and Gelation*, F. Family and D.P Landau editors, p. 75, (Elsevier, 1984).

70 D. Bensimon, B. Shraiman, and S. Liang, "On the ballistic model of aggregation", Phys. Lett. **102**A (5,6), p. 238 (1984).

71 P. Meakin, "Noise reduced diffusion-limited aggregation", Phys. Rev. A **36** (1), p. 332 (1986).

72 R. Tao, M.A. Novotny, and K. Kaski, "Diffusion-limited aggregation with surface tension", Phys. Rev. A **38** (2), p. 1019 (1988).

73 J.E. Yehoda and R. Messier, "Are thin film physical structures fractals?", Appl. Surf. Sci. **22/23**, p. 590 (1985).

74 P. Meakin, "Fractal scaling in thin film condensation and material surfaces", CRC Crit. Rev. Sol. State. and Mat. Sci. **13** (2), p. 143 (1987).

75 L.M. Sander "Fractal growth", Sci. Amer., p. 94 Jan. (1987).

76 J.M. Kim and J.M. Kosterlitz, "Growth in a restricted solid-on-solid model", Phys. Rev. Lett. **62** (19), p. 2289 (1989).

77 S, Chesters, H.Y. Wen, M. Lundin, and G. Kasper, "Fractal-based characterization of surface texture", Appl. Surf. Sci. **40**, p. 185 (1989).

78 A. Bunde, "Physics on fractal surfaces", Festkörperprobleme XXVI, p. 113 (1986).

79 T. Hepel, "Effect of surface diffusion in electrodeposition of fractal structures", J. Electrochem. Soc. **134** (11), p. 2685 (1987).

80 M.J. Brett, "Structural transitions in ballistic aggregation simulation of thin-film growth", J. Vac. Sci. Technol. A **6** (3), p. 1749 (1988).

81 M.J. Brett, "Simulation of structural transitions in thin films", J. Mater. Sci. **24**, p. 623 (1989).

82 M.J. Brett, "Thin film deposition profiles using a ballistic aggregation model", J. Mater. Sci. Lett. **8**, p. 415 (1989).

83 M.J. Brett, K.L. Westra, and T. Smy, "Simulation of thin film step coverage and microstructure", Can. J. Phys. **67** (4), p. 347 (1989).

84 K.L. Westra, T. Smy, and M.J. Brett, "Simulation by ballistic deposition of local density variation and step coverage for via metallization", IEEE Elect. Dev. Lett. **10** (5), p. 198 (1989).

85 T. Smy, K.L. Westra, and M.J. Brett, "Simulation of density variation and step coverage for a variety of via/contact geometries using SIMBAD", IEEE Trans. Elect. Dev. **37** (3), p. 591 (1990).

86 T. Smy, R.N. Tait, and M.J. Brett, " Ballistic deposition simulation of via metallization using a quasi-three dimensional model", IEEE Trans. Computer-Aided Design 1[illegible] (1), p. 130 (1991).

87 L.L. Levenson, H. Usui, I. Yamada, T. Takagi, and A.B. Swartzlander, "Anisotropic surface mobility of aluminum on Si(111) during the initial stage of vapor deposition", J. Vac. Sci. Technol. A **7** (3), p. 1206 (1989).

88 L.L. Levenson, A.B. Swartzlander, H. Usui, and I. Yamada, "Aluminum surface mobility on two types of silicon dioxide during ionized cluster beam deposition", Surf. Inter. Anal. **15**, (1989).

89 S.K. Dew, unpublished

90 P.C. Hiemenz, *Principles of colloid and surface chemistry*, Marcel Dekker Inc., New York, (1977).

91 M.S. Cohen, "Anisotropy in permalloy films evaporated at grazing incidence", J. Appl. Phys. **32**, p. 87S (1961).

92 K. Ozawa, T. Yanada, H. Masuya, M. Sato, S. Ishio, and M. Takahashi, "Oblique incidence effects in evaporated iron thin films", J. Mag. Magn. Mater. **35**, 289 (1983).

93 D. O. Smith, "Anisotropy in parmalloy films", J. Appl. Phys. **30**, p. 264S (1959).

94 T.G. Knorr and R.W. Hoffman, "Dependence of geometric magnetic anisotropy in thin iron films", Phys. Rev. **113**, p. 1039 (1959).

95 H. König and G. Helwig, "Über die Struktur schräg aufgedampfter Schichten und ihr Einfluß auf die Entwicklung submikroskopischer Oberflächenrauhigkeiten", Optik **6**, p. 111 (1950).

96 E.W. Pugh, E.L. Boyd, and J. F. Freedman, "Angle-of-incidence anisotropy in evaporated nickel-iron films", IBM J. Res. Dev. **4**, p. 163 (1960).

97 D.E. Speliotis, G. Bate, J. Kalstad, and J.R. Morrison, "Hard magnetic films of iron, cobalt, and nickel", J. Appl. Phys. **36**, p. 972 (1965).

98 V. Kamberski, Z. Malek, Z. Frait, and M. Ondris, Czechoslovak J. Phys. B**11**, p. 171 (1961).

99 K. Okamoto, T. Hashimoto, K. Hara, M. Kamiya, and H. Fujiwara, "Columnar structure and texture of iron films prepared at various evaporation rates", Thin Solid Films **147**, p. 299 (1987).

100 K. Itoh, M. Kamiya, K. Hara, T. Hashimoto, K. Okamoto, and H. Fujiwara, "Argon gas pressure dependence of the columnar grain structure in iron films deposited obliquely by sputtering", Thin Solid Films **195**, p. 245 (1991).

101 T. Hashimoto, K. Okamoto, K. Hara, M. Kamiya, and H. Fujiwara, "Alignment of columnar grains in obliquely deposited aluminium films", Thin Solid Films **182**, p. 197 (1989).

102 D.O. Smith, M.S. Cohen, and G.P. Weiss, "Oblique-incidence anisotropy in evaporated permalloy films", J. App. Phys. **31** (10), p. 1755 (1960).

103 H. Siefarth, "Hysteresis effect in reactive rf sputtering and the adjustment of the set point for stoichiometric film deposition", Thin Solid Films **172**, p. 61 (1989).

104 J.C. Mitchener and I. Mahawili, "LPCVD: forced-convection flow and the deposition of LTO, PSG, and BPSG dielectric films", Sol. State Technol. **30**, p. 109 (1987).

105 I.A. Blech and H.A. Vanderplas, "Step-coverage simulation and measurement in a dc planar magnetron sputtering system", J. Appl. Phys. **54**, p. 3489 (1983).

106 J.L. Vossen and W. Kern, *Thin Film Processes*, Academic Press, New York, p. 126 (1978).

107 N.G. Nakhodkin and A.I. Shaldervan, "Effect of vapour incidence angles on profile and properties of condensed films", Thin Solid Films **10**, p. 109 (1972).

108 D.K. Pandya, A.C. Rastogi, and K.L. Chopra, "Obliquely deposited amorphous Ge films. I. Growth and structure", J. Appl. Phys. **46** (7), p. 2966 (1975).

109 D.W. Hoffman and J.A. Thornton, "Compressive stress and inert gas in Mo films sputtered from a cylindrical-post magnetron with Ne, Ar, Kr, and Xe", J. Vac. Sci. Technol. **17** (1), p. 380 (1980).

110 A.M. Haghiri-Gosnet, F.R. Ladan, C. Mayeux, H. Launois, and M.C. Joncour, "Stress and microstructure in tungsten sputtered thin films", J. Vac. Sci. Technol. A **7** (4), p. 2663 (1989).

111 M. Itoh, M. Hori, and S. Nadahara, "The origin of stress in sputter deposited tungsten films for x-ray masks", J. Vac. Sci. Technol. B **9** (1), p. 149 (1991).

112 Metals Handbook 9th edition, Vol. **9**, *Metallography and Microstructure*, American Society for Metals, Metals Park, Ohio, (1985).

113 R.N. Tait, T. Smy, and M.J. Brett, "Simulation and measurement of density variation in Mo films sputter deposited over oxide steps", J. Vac. Sci. Technol. A **8** (3), p. 1593 (1990).

114 R.N. Tait, T. Smy, and M.J. Brett, "A ballistic deposition model for films evaporated over topography",Thin Solid Films **187**, p. 375 (1990).

115 J.P. Chow, A.N. Saxena, L.M. Ephrath, and R. S. Bennett, *Dry Etching For Microelectronics*, R.A. Powell ed., North-Holland, Amsterdam, p. 39 (1984).

116 Y. Sakai, J.L. Reynolds, and A.R. Neureuther, J. Electrochem. Soc. **129** (3), PC101 (1982).

117 S. Yamamota, T. Kure, M. Ohgo, K. Matsuzama, S. Tachi, and H. Sunami, IEEE Trans. Computer-Aided Des. **6** (3), p. 417 (1987).

118 J. Pelka, K.P. Müller and H. Mader, IEEE Trans. Computer-Aided Des. **7**(2), p. 154 (1988).

119 R.G. Poulsen, "Plasma etching in integrated circuit manufacture-A review", J. Vac. Sci. Technol. **14**, p. 266 (1977).

120 S.K. Dew, T. Smy, R.N. Tait, and M.J. Brett, "Modeling bias sputter planarization of metal films using SIMBAD", J. Vac. Sci. Technol. A **9** (3), p. 519 (1991).

121 J.I. Ulacia and J.P. McVittie, "A two-dimensional computer simulation for dry etching using Monte Carlo techniques", J. Appl. Phys. **65** (4), p. 1484 (1989).

122 C.J. Mogab, A.C. Adams, and D.L. Flamm, J. Appl. Phys. **49** (7), p. 3796 (1978).

123 R.N. Tait, S.K. Dew, T. Smy, and M.J. Brett, "Density variation of tungsten films sputtered over topography", J. Appl. Phys. **70** (8), p. 4295 (1991).

124 A.J. Strojwas and S.W. Director, "VLSI: linking design and manufacturing", IEEE Spectrum **25** (10), p. 24 (1988).

125 L.D. Hutcheson, ed., *Integrated Optical Circuits and Components*, Marcel Dekker, (1987).

126 G. Mbise, G.B. Smith, G.A. Niklasson, and C.G. Granquist, "Angular selective window coatings: theory and experiment", Proc. SPIE **1149**, p. 179 (1989).

127 H. Nishihara, M. Haruna, and T. Suhara, *Optical Integrated Circuits*, McGraw-Hill, (1989).

128 S. Valette, S. Renard, H. Denis, J.P. Jadot, A. Fournier, P. Phillipe, P. Gidon, A.M. Grouillet, and E. Desgranges, "Si-based integrated optics technologies", Sol. State Technol., pp. 69-75 Feb. (1989).

129 G. Mak, D.M. Bruce, P.E. Jessop, "Waveguide-detector couplers for integrated optics and monolithic optoelectronic switching arrays", Appl. Optics **28** (21), pp. 4629-4636 (1989).

130 J.W. Patten, "The influences of surface topography and angle of adatom incidence on growth structure in sputtered chromium", Thin Solid Films **63**, p. 121 (1979).

131 T. Spalvins, "Characterization of defect growth structures in ion plated films by scanning electron microscopy", Thin Solid Films **64**, p. 143 (1979).

132 K.H. Guenther, "Nodular defects in dielectric multilayers and thick single layers", Applied Optics **20**, p. 1034 (1981).

133 K.H. Guenther, SPIE **678**, Proc. Optical Thin Films II, San Diego, p. 2 (1986).

134 D.J. Smith, SPIE **821**, Proc. Modelling of Optical Thin Films, San Diego, p. 120 (1987).

# Appendix 1: SIMBAD rec4

This appendix includes a description of the version of SIMBAD used for 2-D simulations throughout this thesis. The original version was developed by M.J. Brett, and extensively modified by T. Smy and S.K. Dew, with input from R.N. Tait. This version is known as rec4, referring to the use of a recursive diffusion algorithm, version 4. No source code is provided due to the length of the listing and the fact that it is still being developed. A listing should be available in the thesis of S.K. Dew, a Ph.D. student in this department.

## A1.1 Use of rec4

This section describes the files necessary to run rec4, including input, output and executable files. Italics indicate a user-chosen name, plain text is used for I/O files, and bold type is used to indicate executable files.

Film growth:

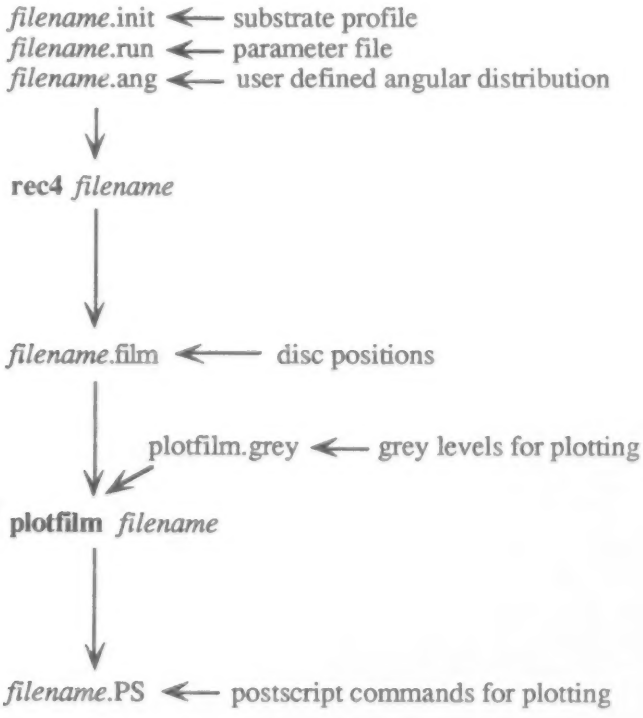
*filename*.init ← substrate profile
*filename*.run ← parameter file
*filename*.ang ← user defined angular distribution
**rec4** *filename*
*filename*.film ← disc positions
plotfilm.grey ← grey levels for plotting
**plotfilm** *filename*
*filename*.PS ← postscript commands for plotting

Density plotting:

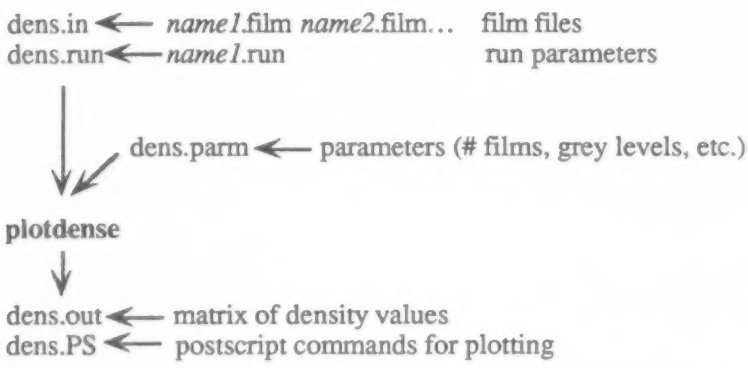
dens.in ← name1.film name2.film... film files
dens.run ← name1.run run parameters
dens.parm ← parameters (# films, grey levels, etc.)
plotdense
dens.out ← matrix of density values
dens.PS ← postscript commands for plotting

*filename*.init contains the substrate initialization in the form:

| | | | |
|---|---|---|---|
| line 1: | # of points | simulation x dimension | simulation y dimension |
| other lines: | x coordinate | y coordinate | type label |

*filename*.run contains the parameters for deposition mode, random seeds, simulation dimensions, diffusion distance, deposition angle and spread, and stopping conditions.

*filename*.ang contains an angular distribution in the form of a list of points

angle probability

where the probability is the likelihood of generating a particle at the given angle relative to the most probable angle.

*filename*.film contains the final film in the form:

| | | | |
|---|---|---|---|
| line 1: | # of discs | simulation x dimension | simulation y dimension |
| other lines: | x coordinate | y coordinate | type label |

plotfilm.grey contains a list of grey levels used for plotting different disc types.

*filename*.PS is a plotting file using postscript® which must be displayed using a postscript® interpreter or postscript® printer.

dens.in is formed by combining film files using the unix command *cat*.
dens.run contains a file of run parameters which are displayed on the density plot.

dens.parm contains density plotting parameters including # of films to average, range over which to average, density threshold for drawing a surface, size of plot boxes, and density grey levels for plotting.

dens.out is a matrix of calculated density values, which avoids recalculating density when changing plot grey scales, and is used for input in the density based etching program.
dens.PS is the postscript® plotting file.

## A1.2 The rec4 Program

This section briefly describes the deposition program in terms of the main subroutines.

The deposition program is based on a grid with spacing such that only one disc can occupy a given cell. This requires that the disc diameter be slightly larger than a cell diagonal. A disc occupying cell *i,j* has its real position and type recorded in *disca(i,j)*, the main storage array for the program. A particle is generated in *GenP* with an appropriate type and trajectory for the process being modelled. *Proces* then follows the particle until it is lost or deposited. *Collid* follows the particle along the trajectory looking for a collision with the substrate or a previously deposited particle. Once contact is made, *Defate* determines if the particle is deposited, etches, or experiences some other process. For normal deposition, *mob* is called to determine a final cradle site. This is a recursive subroutine which searches for a site starting with those in contact with particles neighboring the initial impact point and going out from there. In the case of sites with equal numbers of neighbors, the site closest to the initial impact point is chosen. *Fill* is then used to update arrays. In the case of etching, only the impact disc can be removed, and no surface diffusion of the etchant is allowed. The deposition continues until a specified thickness is reached or a specified number of particles is generated.

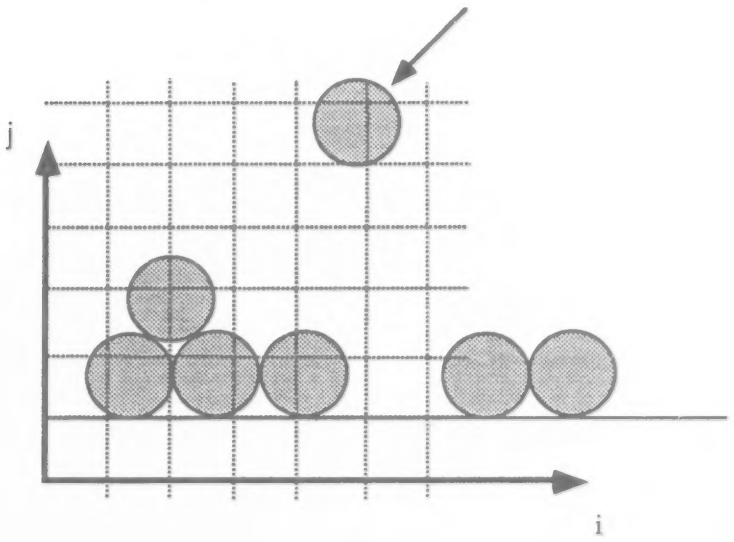


Figure A1.1. The simulation grid.

# Appendix 2: 3-D Simulation

This appendix includes a description of the 3-D simulation program structure and algorithm. This cannot be considered as 3-D SIMBAD since the diffusion and cradling algorithms are drastically different. Source code is included since this program is independent of the SIMBAD simulation project and was intended only for the purpose of preliminary investigations into 3-D film growth mechanisms.

## A2.1 Use of the 3-D Program

This section describes the files necessary to run the 3-D simulation, similar to the description in A1.1.

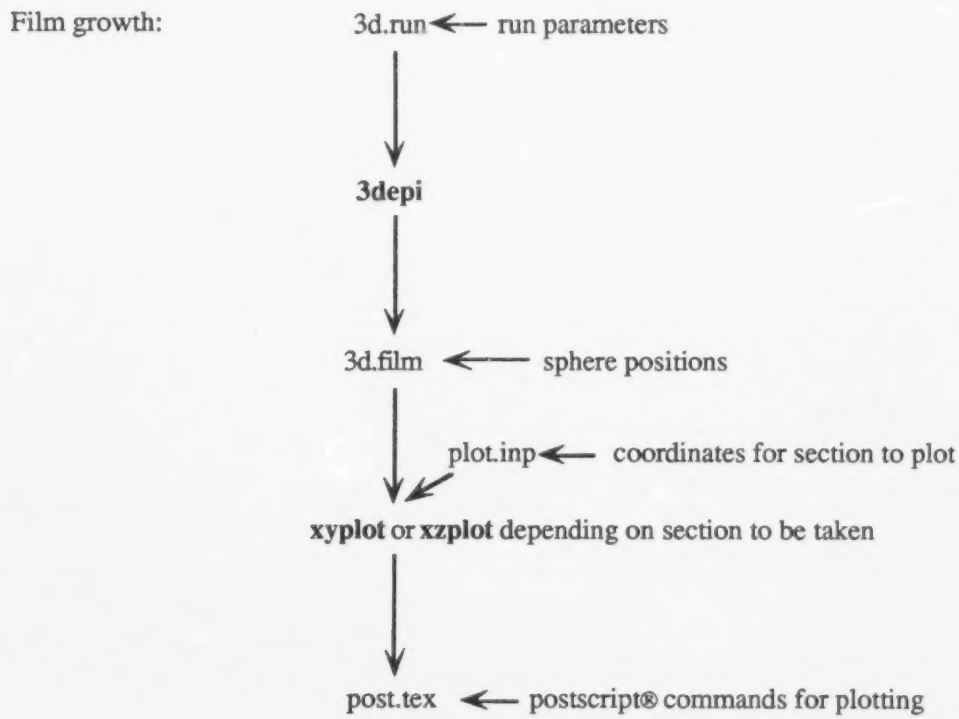

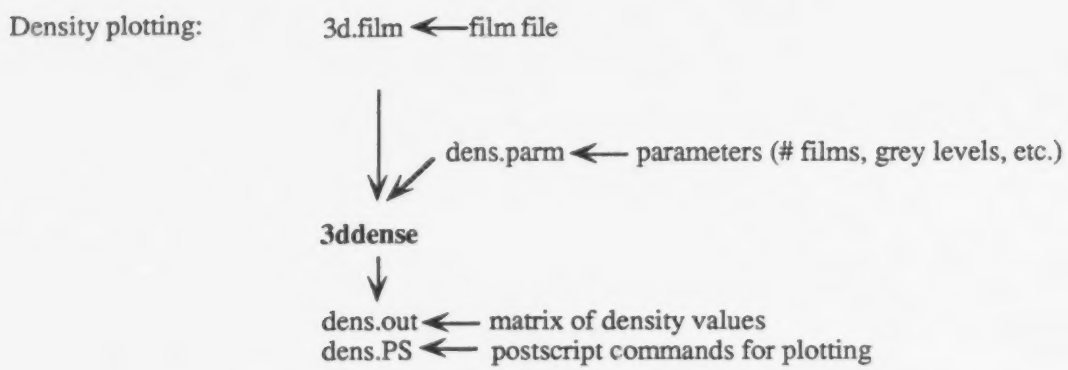


### A2.2 The 3-D Algorithm

While the code provided here is fairly straightforward and well-documented for research code, a description is provided here to clarify the algorithm.

The simulation space is divided into a rectangular array of points representing all possible lattice sites for a hexagonal closest-packed (hcp) arrangement of spheres. Since not all directions are equivalent in such a packing, array points are more closely spaced in some directions than in others, as shown in Figure A2.1. The program makes use of two main arrays. *full(i,j,k)* is a logical array which simply determines if there is a particle occupying a particular array point. *nbond(i,j,k)* records the number of occupied neighboring sites to an array point, updated as particles are deposited.

Within the program, a substrate is initialized in an hcp plane. This has not yet been set up to accept an arbitrary geometry due to the constraint that substrate particles must occupy lattice sites. The deposition mode is read from the *3d.run* file. For evaporation the polar angle is fixed at 90° while the azimuthal angle is given the value given in the run file. For sputtering, both angles are chosen at random to conform to a cosine distribution. Starting coordinates are chosen randomly for particles at a fixed distance above the substrate, and a linear trajectory is calculated.

The subroutine IMPACT follows this line looking for an occupied cell. Boundary conditions are periodic. The search range is a function of the angle of incidence, to account for the non-zero sphere radius. Following impact, FDMIN is used to locate an empty site with a maximum number of neighbors (coordination number) within a given region. If sites with equal coordination numbers are found, the one closest to the impact point is taken. If sites with identical characteristics are found, one is chosen randomly. Once a site is chosen, NEWDISC labels the site as occupied and updates the coordination number for neighboring sites. The presence of a disc in a site prohibits the occupation of certain neighboring points. These are given a zero bond number to inhibit subsequent occupation.

Of course there are a number of details which have not been mentioned which make the code more robust, but these are of little interest. The major drawback of this simulation is the colossal memory requirement. The largest reasonable simulation is about 40X40X40 spheres, requiring about 15 minutes on a Sparcstation 1+.

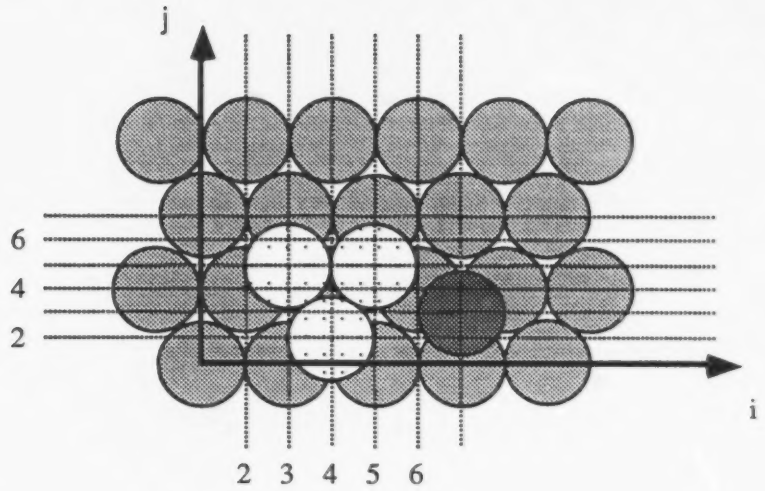


Figure A2.1. The array used for the 3-D simulation.

## A2.3 Program listing

```
      program epitaxy
C***  THIS IS THE MAIN FILM GROWTH PROGRAM
C***  USING FIXED LATTICE SITES
C***  STARTED NOV 21, 1989

C***  3D VERSION
C***  BY NIALL TAIT

      parameter(idim=40,jdim=400,kdim=100)
      integer thick
      integer nbond(idim,jdim,kdim)
      logical full(idim,jdim,kdim),evap,subst


C***  THICK KEEPS TRACK OF THE FILM THICKNESS
C***  FULL(I,J,K) INDICATES PRESENCE OF A DISC AT A LATTICE SITE
C***  NBOND(I,J,K) INDICATES NUMBER OF NEIGHBORS FOR A SITE

      common/scale/xscale,yscale,zscale,iaxis,jaxis,kaxis
      common/array/full,nbond
      common/count/ndepos
      common/subs/jc1,jc2,jc3,jc4

C***  DIRT.DAT IS THE INITIAL CONFIGURATION
C***  RUN.DAT HOLDS RUN PARAMETERS
C***  3D.FILM IS THE OUTPUT FILE


C***  READ PARAMETERS FROM RUN.DAT
C***  ISEED=RANDOM NUMBER SEED
C***  IAXIS,JAXIS,KAXIS ARE SIMULATION DIMENSIONS
C***  MOBIL=RANGE SEARCHED FOR BEST SITE

      open (unit=3,file='3d.run')

      read(3,10)  iseed,iaxis,jaxis,kaxis
10    format (10X,I3/10X,I3/10X,I3/10X,I3)
      write(6,*)  'seed:',iseed,'dimensions:',iaxis,jaxis,kaxis

C***  THIS EXITS THE PROGRAM IF AXES ARE INAPPROPRIATE

      if (iaxis.gt.idim) then
     write(6,*) '**WARNING** iaxis > idim'
      goto 4001
      endif
```

```
      if (jaxis.gt.jdim) then
     write(6,*) '**WARNING** jaxis > jdim'
      goto 4001
     endif
     if (kaxis.gt.kdim) then
     write(6,*) '**WARNING** kaxis > kdim'
      goto 4001
     endif

     read(3,30) mobil,evap,angle,spread
30   format (10X,I3/10X,L2/10X,F4.2/10X,F4.2)
    write(6,*) 'mobility:',mobil,'evap:',evap,angle,spread

     close(unit=3)

C*** ADJUST IAXIS,JAXIS TO BE PERIODIC

     if (iaxis/2*2.ne.iaxis) then
       iaxis=iaxis-1
       write(6,*) 'changed iaxis to',iaxis,' to make periodic'
     endif

     if (jaxis/6*6.ne.jaxis) then
       jaxis=jaxis-(jaxis/6.-jaxis/6)*6
       write(6,*) 'changed jaxis to',jaxis,' to make periodic'
     endif

     xscale=sqrt(3.)/2.
     yscale=.5
     zscale=sqrt(2.)

     xaxis=xscale*(iaxis)
     yaxis=yscale*(jaxis)
     zaxis=zscale*(kaxis)
     write(6,*) 'xaxis:',xaxis,'yaxis:',yaxis,'zaxis:',zaxis

C*** INITIALIZE MATRICES
     do 98 k=1,kdim
     do 97 j=1,jdim
     do 96 i=1,idim
       full(i,j,k)=.false.
       nbond(i,j,k)=0
 96  continue
 97  continue
 98  continue
     write(6,*) 'initialized matrices'

C*** INITIALIZE SUBSTRATE
C**  these points define step corners
```

```
      jc1=120
      jc2=150
      jc3=250
      jc4=280

      call substrate(thick)

      write(6,*) 'initialized substrate',ndepos,'pts',thick


C***  THE MAIN LOOP BEGINS HERE.
C***  IT CONTINUES WHILE THICK<KAXIS
 1000 CONTINUE

      if (thick.ge.kaxis) go to 10000
      loop=loop+1

C***  CHOOSE AZIMUTHAL AND POLAR ANGLES
C***  DEPENDENT ON TYPE OF DEPOSITION

      if (evap) then
       aran=spread*(random(iseed)-0.5)
       alpha=3.14159/180.*(angle+aran)
       theta=3.14159/2.
      else
       aran=random(iseed)
      alpha=asin(aran)*75./90.
      if (random(iseed).lt.0.5) alpha=-alpha
       aran=random(iseed)
       theta=2.*3.14159*aran
      endif

      cosa=cos(alpha)
      sina=sin(alpha)
      cost=cos(theta)
      sint=sin(theta)

C***  CHOOSE A RANDOM STARTING POSITION

      xran=random(iseed)
      xran=xran*xaxis
      yran=random(iseed)
      yran=yran*yaxis

C***  CHOOSE THE PARAMETERS OF THE LINE DX/DZ and DY/DZ

      xslope=cost*sina/cosa
      yslope=sint*sina/cosa
```

```
C***  LOOK FOR A COLLISION

      call impact(thick,icr,jcr,kcr,xslope,yslope,xran,yran)

C***  LOOK FOR THE BEST SITE IN THAT REGION

      call fdmin(icr,jcr,kcr,im,jm,km,cm,mobil)

C***  UPDATE THE ARRAYS

      subst=.false.
      call newdisc(im,jm,km,thick,subst)

      if(ndepos/100*100.eq.ndepos) then
      write(6,*) ndepos,thick
      endif

C***  GO BACK AND GET ANOTHER ATOM


      go to 1000

10000 continue

C***  NOW WRITE POSITIONS TO 3D.FILM
      write(6,*) 'writing final positions',loop,'loops'
      open (unit=4,file='3d.film')
      write(4,*) ndepos,iaxis,jaxis,kaxis
      ntot=0

      do 4000 j=jaxis,1,-1
      do 3000 i=1,iaxis
      do 2000 k=1,kaxis

      if ((k.gt..1*kaxis).and.(k.lt..9*kaxis)) ntot=ntot+1

      if (full(i,j,k)) then
      if ((k.gt..1*kaxis).and.(k.lt..9*kaxis)) nden=nden+1
       x=i*xscale
       y=j*yscale
       z=k*zscale
       write(4,*) x,y,z
       nwrit=nwrit+1
      endif

2000  continue
3000  continue
4000  continue
```

```
      close (unit=4)
4001  continue
      write(6,*) 'ndepos=',ndepos,'# written=',nwrit
      open (unit=3, file='den')
      write(3,*) 'angle = ',angle,'density = ',nden*12./2./ntot
      close (unit=3)
      stop
      end


C***
      subroutine newdisc(ifin,jfin,kfin,thick,subst)

      parameter(idim=40,jdim=400,kdim=100)
      integer thick
      integer nbond(idim,jdim,kdim)
      logical full(idim,jdim,kdim),over,subst

      common/scale/xscale,yscale,zscale,iaxis,jaxis,kaxis
      common/array/full,nbond
      common/count/ndepos
      common/subs/jc1,jc2,jc3,jc4

C***  CHECK IF AN OVERWRITE HAS OCCURRED

      call overlap(ifin,jfin,kfin,io,jo,ko,over)
      if (over) then
      write(6,*) 'overwrite!',ifin,jfin,kfin,nbond(ifin,jfin,kfin)
        nbond(ifin,jfin,kfin)=0
        go to 503
      endif

C***  IF THE SITE IS GOOD, RECORD THE DISC

      full(ifin,jfin,kfin)=.true.
      nbond(ifin,jfin,kfin)=0
      ndepos=ndepos+1

C***  AND UPDATE NEIGHBORING SITES

      k1=kfin-1
      k2=kfin+1
      j1=jfin-3
      j2=jfin+3
      i1=ifin-2
      i2=ifin+2

      do 502 k=k1,k2
      do 501 j=j1,j2
```

```
      do 500 i=i1,i2

      it=i
      jt=j

      if (k.lt.1) k=1
      if (k.gt.kaxis) k=kaxis
      if (j.lt.1) jt=j+jaxis
      if (j.gt.jaxis) jt=j-jaxis
      if (i.lt.1) it=i+iaxis
      if (i.gt.iaxis) it=i-iaxis

      if (k.eq.kfin) then
        if (((abs(i-ifin).eq.1).and.(abs(j-jfin).eq.3)).or.
     +    ((abs(i-ifin).eq.2).and.(j.eq.jfin))) then
          nbond(it,jt,k)=nbond(it,jt,k)+1

        elseif((abs(i-ifin)+abs(j-jfin).le.2).and.
     +       (abs(i-ifin).ne.2)) then
         nbond(it,jt,k)=0
       endif

      else

       if((abs(i-ifin)+abs(j-jfin).eq.2).and.(j.ne.jfin)) then
        nbond(it,jt,k)=nbond(it,jt,k)+1
      elseif(abs(i-ifin)+abs(j-jfin).le.1) then
      nbond(it,jt,k)=0
     endif

      endif

      if (subst) then
       if (((jfin.lt.jc1).or.(jfin.gt.jc4))
     +   .and.(k.lt.kfin)) nbond(it,jt,k)=0
       if (((jfin.gt.jc2).and.(jfin.lt.jc3))
     +   .and.(k.lt.kfin)) nbond(it,jt,k)=0
       if (((jfin.gt.jc1).and.(jfin.lt.jc2))
     +   .and.(jt.lt.jfin)) nbond(it,jt,k)=0
       if (((jfin.gt.jc3).and.(jfin.lt.jc4))
     +   .and.(jt.gt.jfin)) nbond(it,jt,k)=0
      endif

C***  SET BOND NUMBER=0 IN OVERLAPPING SITES

      call overlap(it,jt,k,io,jo,ko,over)

        if (over) then
         nbond(it,jt,k)=0
```

```
        endif

500   continue
501   continue
502   continue

      if (kfin.gt.thick) thick=kfin
503   continue
      subst=.false.
      return
      end



      subroutine impact(thick,ihit,jhit,khit,xslope,yslope,xran,yran)
C***  THIS SUBROUTINE LOOKS FOR THE POINT WHERE THE
C***  INCIDENT DISC STRIKES A PREVIOUSLY DEPOSITED DISC

      parameter(idim=40,jdim=400,kdim=100)
      integer thick
      integer nbond(idim,jdim,kdim)
      logical full(idim,jdim,kdim),imp,over

      common/scale/xscale,yscale,zscale,iaxis,jaxis,kaxis
      common/array/full,nbond

C***  WORK IN X,Y COORDS FOR TRAJECTORY

      imp=.false.
      xaxis=xscale*(iaxis)
      yaxis=yscale*(jaxis)

      xnew=xran
      ynew=yran

      xshift=xaxis
      yshift=yaxis

      if (abs(xslope).gt.xaxis) xshift=2*xaxis
      if (abs(yslope).gt.yaxis) yshift=2*yaxis
      if (abs(xslope).gt.2*xaxis) xshift=3*xaxis
      if (abs(yslope).gt.2*yaxis) yshift=3*yaxis

      ihit=0
      jhit=0
      khit=0

      do 600 k=kaxis,1,-1
```

```
      z=zscale*k
      xnew=xnew-xslope*zscale
      ynew=ynew-yslope*zscale

C***  IF XNEW OR YNEW IS OUT OF RANGE, SHIFT BY THE APPROPRIATE
AMOUNT

      if (xnew.le.0.) xnew=xnew+xshift
      if (xnew.ge.xaxis) xnew=xnew-xshift
      if (ynew.le.0.) ynew=ynew+yshift
      if (ynew.ge.yaxis) ynew=ynew-yshift

      i=int((xnew)/xscale+1.)
      j=int((ynew)/yscale+1.)

      rmin=100.
C***  MAKE SEARCH RANGE A FUNCTION OF ANGLE OF INCIDENCE

      i1=i-abs(int(xslope*zscale))-1
      i2=i+abs(int(xslope*zscale))+1
      j1=j-abs(int(yslope*zscale))-2
      j2=j+abs(int(yslope*zscale))+2
      do 552 n=k+1,k-1,-1
      do 551 l=i1,i2
      do 550 m=j1,j2

      lt=l
      mt=m
      if (l.lt.1) lt=l+iaxis
      if (l.gt.iaxis) lt=l-iaxis
      if (m.lt.1) mt=m+jaxis
      if (m.gt.jaxis) mt=m-jaxis

C***  IF A DISC IS NEARBY, CHECK FOR IMPACT
C***  TAKE DISC NEAREST TO TRAJECTORY
      if (full(lt,mt,n)) then
      call touch(i,j,k,l,m,n,over)
      if (over) then
          rhit=(xscale*(l-i))**2+(yscale*(m-j))**2
     +     +(zscale*(n-k))**2
          imp=.true.
       if (abs(rhit-rmin).lt.0.01) then
        if (random(iseed).gt..5) then
            ihit=lt
            jhit=mt
            khit=n
       endif
       elseif (rhit.lt.rmin) then
```

```
            rmin=rhit
              ihit=lt
              jhit=mt
              khit=n
        endif
         endif

         endif

  550  continue
  551  continue
  552  continue
C*** IF IMPACT OCCURRED, EXIT
         if (imp) goto 700
  600    continue

  700    continue

         return
         end

         subroutine fdmin(ihit,jhit,khit,im,jm,km,cm,mobil)

         parameter(idim=40,jdim=400,kdim=100)
         integer nbond(idim,jdim,kdim)
         integer imax(20),jmax(20),kmax(20)
         logical full(idim,jdim,kdim)

         common/scale/xscale,yscale,zscale,iaxis,jaxis,kaxis
         common/array/full,nbond

         do 788 i=1,20
          imax(i)=1
          jmax(i)=1
          kmax(i)=1
  788    continue

         loop=0
         nmax=0
         max=0
         rmin=100.

C***  CHOOSE SITE WITH MAX NUMBER OF BONDS

         do 802 k=khit-1,khit+1
         do 801 j=jhit-3,jhit+3
         do 800 i=ihit-2,ihit+2

         it=i
```

```
      jt=j
      if (i.lt.1) it=i+iaxis
      if (i.gt.iaxis) it=i-iaxis
      if (j.lt.1) jt=j+jaxis
      if (j.gt.jaxis) jt=j-jaxis

      nb=nbond(it,jt,k)
C***  CHECK FOR MULTIPLE MAXIMA
      if (nb.eq.max) then
         rnew=(xscale*(i-ihit))**2+(yscale*(j-jhit))**2
     ++(zscale*(k-khit))**2
      if (rnew.eq.rmin) then
        nmax=nmax+1
        imax(nmax)=it
        jmax(nmax)=jt
        kmax(nmax)=k
      endif

C***  OR TAKE THE MAXIMUM CLOSEST TO THE IMPACT POINT
      if (rnew.lt.rmin) then
       nmax=1
        imax(nmax)=it
        jmax(nmax)=jt
        kmax(nmax)=k
       rmin=rnew
      endif
      endif
      if (nb.gt.max) then
          nmax=1
          imax(nmax)=it
          jmax(nmax)=jt
          kmax(nmax)=k
            max=nb
          rmin=(xscale*(i-ihit))**2+(yscale*(j-jhit))**2
     +       +(zscale*(k-khit))**2
      endif

  800 continue
  801 continue
  802 continue

      if (nmax.eq.0) then
     write(6,*) 'nomax'
    endif

C***  CHOOSE A MINIMUM RANDOMLY

      l=int(random(iseed)*nmax)+1
      im=imax(l)
```

```
      jm=jmax(l)
      km=kmax(l)
      cm=max

      return
      end



C***
C***  RANDOM NUMBER GENERATOR ON (0,1)
C***

      real function random(iseed)
      iseed=mod(25173*iseed+13849,65536)
      random=float(iseed)/65536
      return
      end
C***
C***  PERIODIC BOUNDARY CONDITION
C***

      subroutine bound(i,iaxis)
      if (i.lt.1) i=i+iaxis
      if (i.gt.iaxis) i=i-iaxis
      return
      end

C***
C***  CHECK IF DISC AT I1,J1,K1 IS TOUCHING DISC AT I2,J2,K2
C***

      subroutine touch(i1,j1,k1,i2,j2,k2,over)
      logical over
      over=.false.
      r=sqrt((xscale*(i2-i1))**2+(yscale*(j2-j1))**2
     +    +(zscale*(k2-k1))**2)
      if (r.le.sqrt(3.)) over=.true.
      return
      end

C***
C***  CHECK FOR OVERLAPPING DISCS
C***

      subroutine overlap(i,j,k,io,jo,ko,over)

      parameter(idim=40,jdim=400,kdim=100)
```

```
      integer nbond(idim,jdim,kdim)
      logical full(idim,jdim,kdim),over

      common/scale/xscale,yscale,zscale,iaxis,jaxis,kaxis
      common/array/full,nbond

      ip=i+1
      jp=j+1
      im=i-1
      jm=j-1
      jmm=j-2
      jpp=j+2
      if (ip.gt.iaxis) ip=ip-iaxis
      if (jp.gt.jaxis) jp=jp-jaxis
      if (im.lt.1) im=im+iaxis
      if (jm.lt.1) jm=jm+jaxis
      if (jpp.gt.jaxis) jpp=jpp-jaxis
      if (jmm.lt.1) jmm=jmm+jaxis

      over=.false.

      if (full(i,j,k).or.full(ip,jp,k)
     + .or.full(im,jm,k).or.full(ip,jm,k)
     + .or.full(im,jp,k).or.full(i,jpp,k)
     + .or.full(i,jmm,k)) over=.true.

      return
      end

C***
C***  THIS IS THE SUBSTRATE INITIALIZATION
C***    FOR A STEP
C***
      subroutine  substrate(thick)

      parameter(idim=40,jdim=400,kdim=100)
      integer nbond(idim,jdim,kdim)
      integer thick
      logical full(idim,jdim,kdim),subst

      common/scale/xscale,yscale,zscale,iaxis,jaxis,kaxis
      common/array/full,nbond
      common/count/ndepos
      common/subs/jc1,jc2,jc3,jc4

      write(6,*) 'subroutine  substrate'
C**   ks is the top of the step
      ks=(jc2-jc1)+1
      j=1
```

```
      inn=0
      jinc=3
      kinc=0
      thick=ks
c     do 101 j=1,jaxis,jinc
 91   continue
      inn=inn+1
      j=j+jinc
      ks=ks+kinc
      is=1+(2*(float(inn)/2.-inn/2)/1)

      if (j.gt.jc1) then
       jinc=1
       kinc=-1
      endif
      if (j.gt.jc2) then
       jinc=3
       kinc=0
      endif
      if (j.gt.jc3) then
       jinc=1
       kinc=1
      endif
      if (j.gt.jc4) then
       jinc=3
       kinc=0
      endif

      do 100 i=is,iaxis,2
      subst=.true.
      call newdisc(i,j,ks,thick,subst)
      if (ndepos/50*50.eq.ndepos) write(6,*) ndepos
100   continue
101   continue
      if (j.lt.jaxis-3) goto 91

      return
      end
```

# Appendix 3: Optical Coatings†

With progress in integrated optics, both topographies and dimensions similar to those found in microelectronics are beginning to appear. The influence of microstructure on optical properties of films is widely known.[25,31] The inhomogeneity due to the microstructure of optical coatings deposited over topographies is important to the understanding of losses due to absorption and scattering in many devices.[125] SIMBAD is ideal for predicting these inhomogeneities.

SIMBAD has previously been shown to provide good qualitative information on films deposited over steps and vias, and density variation results have agreed well with experimental data.[113] By measuring both density[126] and refractive index of planar films as a function of deposition angle, we can relate SIMBAD predictions to refractive index variations in films sputtered or evaporated over topography.

## A3.1 Evaporated Films

The most common method of optical coating production is thermal evaporation in vacuum, and one of the most common coating materials is $MgF_2$. In order to relate the density information provided by SIMBAD to an optical property such as refractive index, it is necessary to find the refractive index as a function of density. This was done by depositing $MgF_2$ on planar silicon substrates at angles from 0° to 80° between source normal and substrate normal, and then measuring the properties of interest.

Silicon substrates were sawed to 1.1 cm squares, cleaned, and then weighed on a Mettler H51 balance accurate to 10 μg. They were then placed in angled holders with 1 cm square windows exposed to the evaporation source. Angles were in 10° increments from 0° to 80°. Approximately 0.5 μm of $MgF_2$ was then evaporated onto the substrates from a Mo boat.

Following deposition the substrates were once again weighed. The difference between the two measurements gives the film mass. The thickness was found using a Tencor Alpha-Step 200 profilometer to measure the height of the step formed at the edge of the film by the window in the substrate holder. Using the mass and volume of the film, the density as a function of deposition angle was calculated, and is displayed in Fig. A3.1.

Once the film densities were known, the sample refractive indices were measured using a Gaertner L125B ellipsometer at 633 nm. This also provided a check on the thickness measured using the profilometer. The index data is shown in Fig. A3.2. Combining the data, a plot of refractive index as a function of density is obtained, as shown in Fig. A3.3.

---

† The material in this appendix has been published as:

R.N. Tait, S.K. Dew, T. Smy, and M.J. Brett, SPIE **1324**, pp. 112-119 (1990).

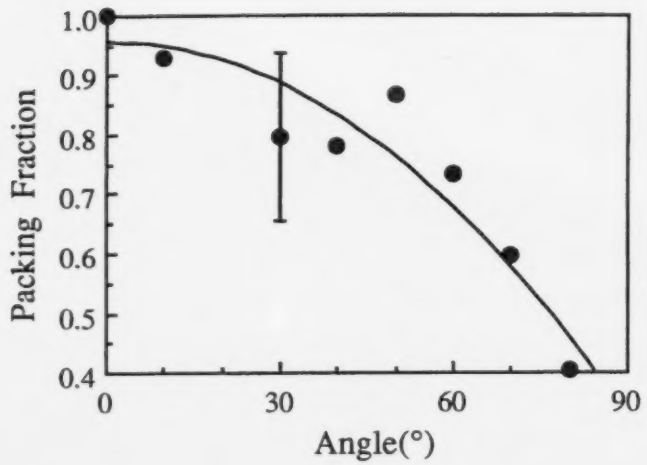


Figure A3.1. Density of evaporated $MgF_2$ films. A typical uncertainty is shown.

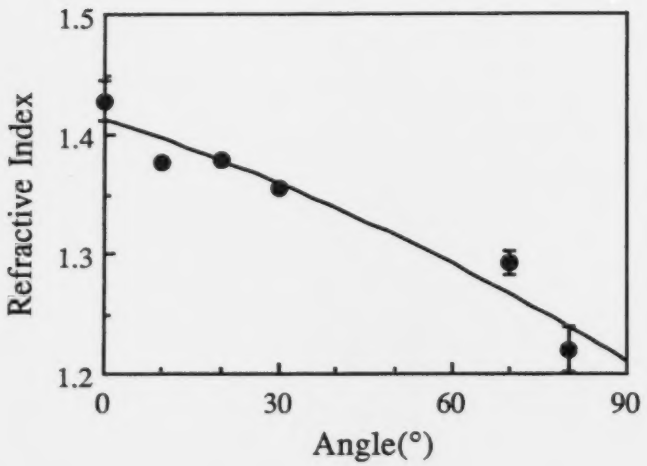


Figure A3.2. Refractive index of evaporated $MgF_2$ films.

The uncertainties in these data are significant. The errors in relative density are about 20% due to the low mass of the films relative to the balance accuracy. Substrate sizes were originally chosen for high density refractory metal films, and they are too small for good accuracy in the current application to optical coatings. In addition the two mass measurements were made several days apart, and the scale was zeroed each time a set of measurements was made. This introduced an offset in the density data due to the zeroing error, which could give an error in absolute density as high as 40%. Obviously this can be improved, but because the measurements are more accurate relative to each other, the measured trend is valid. It is possible to calculate relative density between films deposited under identical conditions without using the mass measurement, but this requires the assumption that the mass of material deposited on a substrate is proportional only to the area orthogonal to the flux direction. Uncertainty in the refractive index is the scatter in ellipsometer measurements at different points on the sample surface. This scatter is large enough to prevent accurate measurement of birefringence in these films.

The result of the measurements is an almost linear relationship between refractive index and density. The zero offset in the mass discussed earlier can be estimated to be the difference between the measured mass at normal incidence and the mass expected for bulk density in the film. After this correction, the data can then be converted to density. There is good agreement between experiment and a calculation of index variation based on a linear interpolation between the bulk index of the film and the void material,[29]

$$n_f = (1-p)\, n_v + p n_b \qquad \text{A3.1}$$

where $n_f$ is the film index, $n_v$ is the void index, $n_b$ is the bulk index of the film material, and p is the density in the film. The theoretical curve is indicated by a dotted line in Fig. A3.3. The theory of Bragg and Pippard[25,30] based on cylindrical columns also gives good agreement, particularly if some allowance is made for water absorption by the film.

These $MgF_2$ films behave much as expected, and demonstrate that film density predictions can be related to refractive index variations. $MgF_2$ is not, however, a common integrated optics material, and is seldom deposited over micron scale topography. $SiO_2$ is commonly used in optical devices, particularly with silicon based technologies. It is often sputtered and therefore is well-suited to the study outlined here.

## A3.2 Sputtered Films

Many glasses have been RF sputtered to form optical devices, with minor stoichiometric changes resulting from the process.[127] The target used here was a 5 cm diameter fused silica window 2 mm thick. Substrates were prepared and mounted in the same manner as previously described. About 1 μm of $SiO_2$ was RF sputtered from the planar magnetron source in 0.67 Pa of Argon. Density and refractive index measurements were made as with the evaporated films, and with the same problems in measurement accuracy.

Because of the broad angular distribution of material coming from a sputter target, the film homogeneity is less dependent on deposition angle. That is, the density and refractive index vary much less for $SiO_2$ than for the evaporated $MgF_2$

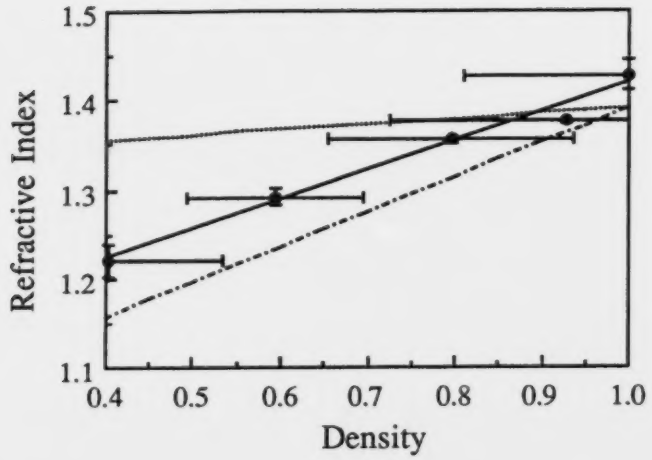


Figure A3.3. Refractive index vs. density for evaporated $MgF_2$ films. The lines are from equation A3.1. The upper line assumes water-filled voids, while the lower line assumes air-filled voids.

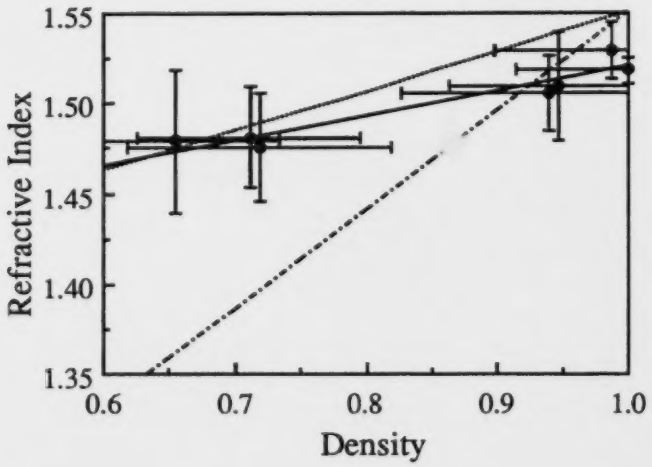


Figure A3.4. Refractive index vs. density for sputtered $SiO_2$ films. The lines are from equation A3.1. The upper line assumes water-filled voids, while the lower line assumes air-filled voids.

films. This makes scatter in the silica data more obvious, although the expected trend is still apparent. Again, the refractive index variation with density agrees with the linear theory, as shown in Fig. A3.4, although it appears the films have absorbed some water vapour. This index variation, although small, can still be of interest in the design of optical devices.

### A3.3 Applications

The refractive index variation discussed here is due to oblique incidence of material flux on a substrate. Therefore, any device requiring an optical coating deposited on a structure with vertical or sloped sidewalls will exhibit some reduction in index on these faces.

As an example, consider a silicon-based ridge waveguide structure. These are now designed to resemble optical fibers: they contain three layers of $SiO_2$ on a Si substrate, with the centre layer doped to control the index.[128] This centre guiding layer forms a rectangular step over which the final $SiO_2$ cladding layer must be deposited. The index variation in this cladding due to the film microstructure could easily be as large as the designed difference in index between core and cladding, $\Delta n$, which is normally about $5 \times 10^{-3}$. This discourages the use of sputtering for structures of this type.

Another structure in which sputtered glass is commonly used is a waveguide-detector coupler.[129] A silicon substrate is covered with a thick layer of $SiO_2$ which acts as a cladding. A layer of glass is sputtered on this to form the waveguide. Away from the detector coupling region the $SiO_2$ layer is thick enough that there is negligible optical interaction with the silicon. In the coupling region the $SiO_2$ layer is tapered to a thickness where the evanescent tail of the optical field extends into the silicon and results in some absorption. A photoconductive detector is formed in this region by depositing ohmic contacts on the silicon. The resulting structure is a groove with sloped sidewalls, over which the glass waveguide layer is sputtered.

The refractive index dependence on deposition angle for sputtered glass, which was described in section A3.2, becomes important in this structure as the taper angle increases. Taper losses should be kept small for accurate measurement of leaky waveguide losses in the coupling region. Scattering due to variations in the waveguide index, and corresponding variations in the propagation constant $k_o n$ will increase as the taper angle increases. The result is a limitation on the minimum taper length, and therefore the minimum device size.

A SIMBAD simulation of a structure similar to the waveguide-detector coupler described here is shown in Fig. A3.5. The topography shown represents a 2 μm wide trench about 0.5 μm deep, with 45° sidewalls. The disc plot, a simulation using about 60 000 discs, shows typical microstructure for a film of this type. Of more interest is the accompanying density plot, which is an average of ten films. There is a definite drop in density, and therefore refractive index, on the sidewalls, particularly at the bottom corners. The corner voids are caused by the intersection of columns growing from the bottom and the sidewall of the substrate. This inhomogeneity will be emphasized as sidewall angle is increased.

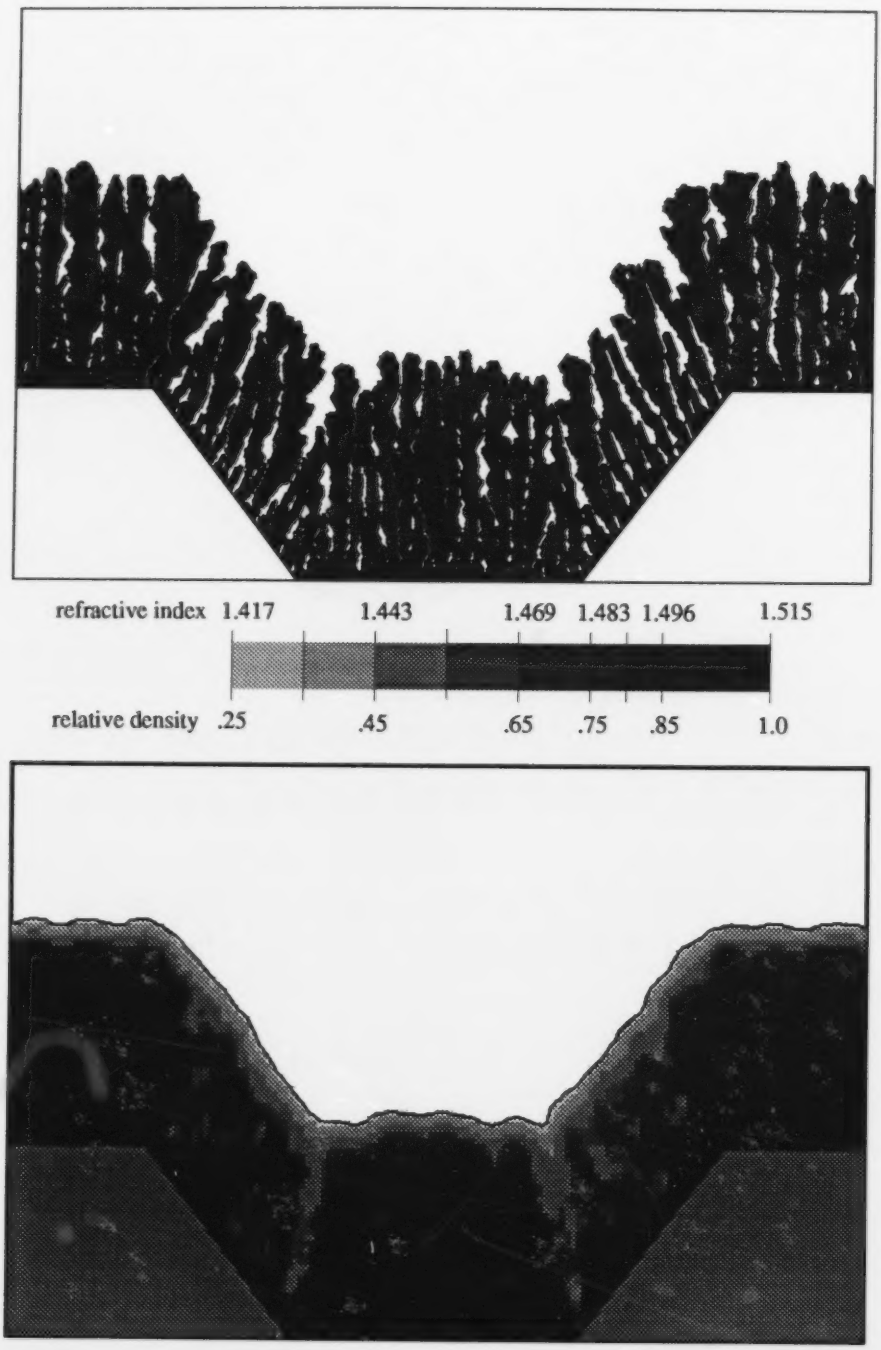


Figure A3.5. SIMBAD simulation and density plot of sputtered $SiO_2$ for a waveguide detector coupler.

For the density plot a gray scale legend is provided. The bins have been adjusted slightly to reduce noise and emphasize density variations at the upper end of the scale. The averaged density values are listed below the legend, and the refractive index values calculated from the experimental curve in Fig. A3.4 are listed above the legend. This predicts an index drop of about 3% in the low density regions at the bottom corners of the step. The density drop at the surface of the film is an artefact of surface roughness and the averaging of density at the boundary.

### A3.4 Conclusion

By experimentally relating density and refractive index, it is possible to use SIMBAD to identify inhomogeneities in integrated optical devices. Sputtered films have been shown to have properties less sensitive to oblique deposition than those of evaporated films. Some examples of devices for which such simulations are useful have been suggested.

# Appendix 4: Nodule Growth†

Nodular defects are commonly found in thin films deposited by evaporation or sputtering, originating from substrate surface irregularities or preferential nucleation sites. These nodules grow in the shape of an inverted cone with a domed top protruding above the surface of the film. Shadowing effects create a void region between the nodule and the film, and the nodule may separate from the film leaving a cavity. Such cavities can cause serious problems with optical or microelectronic coatings, hence an improved understanding of nodule nucleation, growth, and structure may be useful for inhibiting their formation.

The nodule growth mechanism and geometry has been studied in sputtered Cr,[130] ion plated Cu and Au,[131] and in a number of optical coatings.[132] The growth of nodules has been demonstrated using ballistic hard disc models, showing the growth is a physical process caused by shadowing and dependent on deposition geometry.[133,134] Shape is found to be conical for films grown with a narrow flux distribution (ie: evaporation) and parabolic for films receiving a broad distribution.[132] Clearly SIMBAD is well-suited to a study of the structure and density of nodular defects.

## A4.1 Nodule Growth

Polystyrene latex spheres, normally used for scanning electron microscope calibration, were used as seeds to initiate nodule growth. Spheres of diameters 91, 173, 300, and 482 nm were provided in a suspension and were applied to Si wafer substrates in diluted form to achieve a surface density of about $2 \times 10^7$ $cm^{-2}$. Subsequently $MgF_2$ was evaporated onto the wafers from an Mo boat to a thickness of about 1μm. System base pressure was $3 \times 10^{-4}$ Pa and the deposition rate was 4 nm/s. Film cross-sections were prepared by cleaving the wafer after deposition, mounting and then coating with a thin layer of gold.

## A4.2 Results

Nodule growth was observed from seeds of all sizes. Figures A4.1 and A4.2 show nodules grown from 300nm seeds. The seed in Figure A4.1 is not evident, probably due to the baking used to cure the epoxy used in mounting samples for the SEM. The sample in Figure A4.2 was not baked and the seed can be clearly seen. The circle of residue beneath the nodule may be due to the suspension used when applying the spheres to the substrate, or it could be a layer of $MgF_2$ deposited in this region by re-evaporation or reflection. The orientation of the nodule in Figure A4.2 is

---

† The material in this appendix has been accepted for publication as:

M.J. Brett, R.N. Tait, S.K. Dew, T. Smy, S. Kamasz, and A.H. Labun, J. Mater. Sci. (1992).

Figure A4.1. Nodule in $MgF_2$ grown from a 300 nm latex sphere. The seed appears to have melted and is not visible.

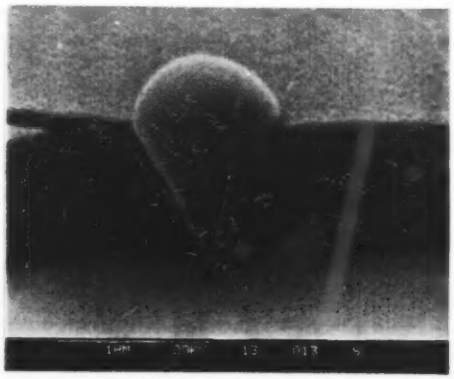

Figure A4.2. A nodular defect in $MgF_2$ grown from a latex sphere. The seed is visible beneath the nodule.

not quite vertical, probably due to its position near the edge of the substrate. This results in evaporant arriving at a slight angle to the substrate normal.

These particular nodules were chosen for study due to the clarity of the images. The nodules display straight sidewalls as expected for evaporation, and are separated from the rest of the film by a void region. Columnar structure is faintly visible in the film and nodule as expected for the relatively dense $MgF_2$ when deposited near zone 2 of the Thornton structure zone model. Evidence of the poor connection of the nodular defects to the film is shown in Figure A4.3, showing fracture due to intrinsic and cleaving stress which propagates from nodule to nodule.

SIMBAD simulations consisting of about 40 000 discs representing a region about 2 μm wide were used to demonstrate nodule growth. The cross-sectional density profile is shown in Figure A4.4. This profile shows good agreement of shape and size when compared with a real nodule such as the one in Figure A4.1. The void regions around the nodule are well defined, and the simulation cone angle of $44° \pm 2°$ agrees with the angle $42.5° \pm 1.5°$ measured from Figure A4.1. The most significant result of the simulation, however, is the density profile which clearly shows the cause of nodules breaking free from the film. This is, of course, a consequence of the angle between the evaporant flux and the nodule surface, which increases near the perimeter of the nodule.

Simulations have been performed to study the effects of diffusion on nodule growth, with little or no change in properties found with change of diffusion length by a factor of 2.5.[134] Using SIMBAD, diffusion distances or seed sizes can be varied by an order of magnitude. Series of simulations indicate that for seed radius equal to or less than the diffusion length, the perturbing influence of the seed is largely reduced. This implies that observation of nodule growth on various seed sizes may be able to provide an estimate of film diffusion lengths. The diffusion distance is an important parameter in many film simulations but has never been measured under realistic film growth situations.

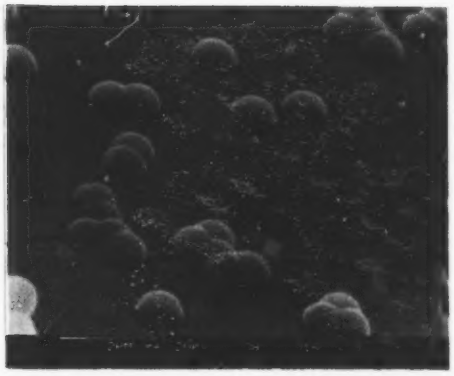

Figure A4.3. Fracture in a $MgF_2$ film containing nodular defects.

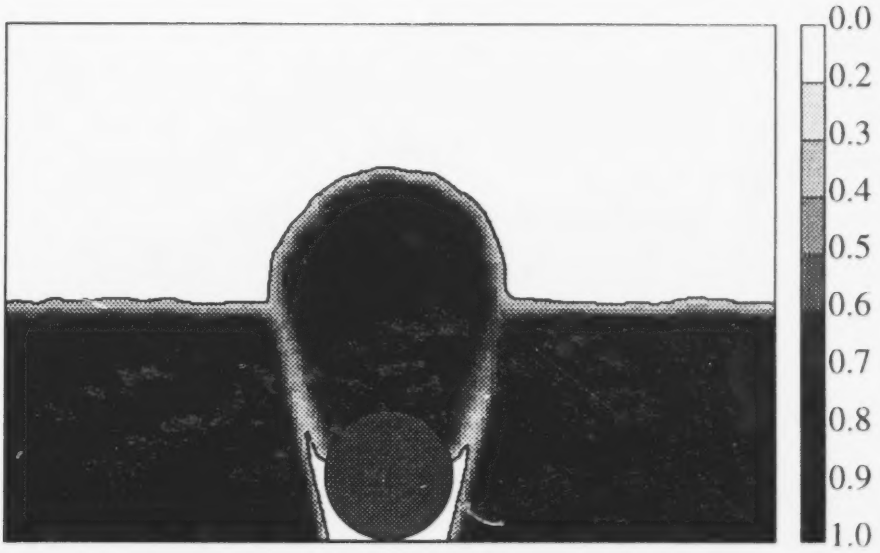


Figure A4.4. SIMBAD density profile of a nodular defect.

# Appendix 5: Simulating Giant Hailstone Structure†

Monte Carlo or ballistic aggregation models have found applications in simulation of rime ice growth, in addition to applications in thin film growth. While the growth of rime and formation of thin films by physical vapor deposition are very different processes, they share many common characteristics.

## A5.1 Hailstone Growth with SIMBAD

Since rime ice consists of an aggregation of frozen spherical cloud droplets, hard disc models have been successful in representing growth angle and density of ice formations. SIMBAD was the first such model which included relaxation of the deposited discs. This relaxation was a crude simulation of the spreading of droplets which occurs on impact at high speeds and at elevated temperatures.

To simulate the growth of a hailstone, a disc-shaped substrate was used. Discs were then deposited as in a normal simulation, from a random position along one side of the simulation space. To simulate the rotation of the hailstone, this starting line was rotated around the growing accretion with a constant angular velocity. At stages in the growth the diffusion length of the deposited discs was increased temporarily to simulate temperature changes during growth.

Using this technique a scaling problem arises similar to that found in thin film growth simulations. Large cloud droplets are seldom larger than about 50 μm, so a simulation of a 10 cm hailstone would require an unreasonable number of discs. It is therefore necessary to interpret discs as representing the average effect of many droplets. As with the thin film simulations, this works well provided discs are much smaller than column diameters.

A simulation using the method described is shown in Figure A5.1, along with a thin section of a real hailstone for comparison in Figure A5.2. Notice that both exhibit similar characteristics including a columnar lobed structure containing air voids and pockets. This similarity indicates that the the structure is in fact a result of the rotation of the hailstone during formation and shadowing effects in the growing structure.

A measurement of the number of lobes gives approximate agreement between the simulation and the real structure. This is further evidence that this model captures the essence of the growth process. The result gives support to the possibility that some giant hailstones may grow in part by fast rime growth with subsequent soaking. With further work this model may provide inferences about hailstone aerodynamics, and is of interest in the study of rime icing of power lines.

---

† The material in this appendix has been published as:

E.P. Lozowski, M. Brett, N. Tait, and T. Smy, Q.J.R. Meteorol. Soc. **117**, pp. 427-431 (1991).

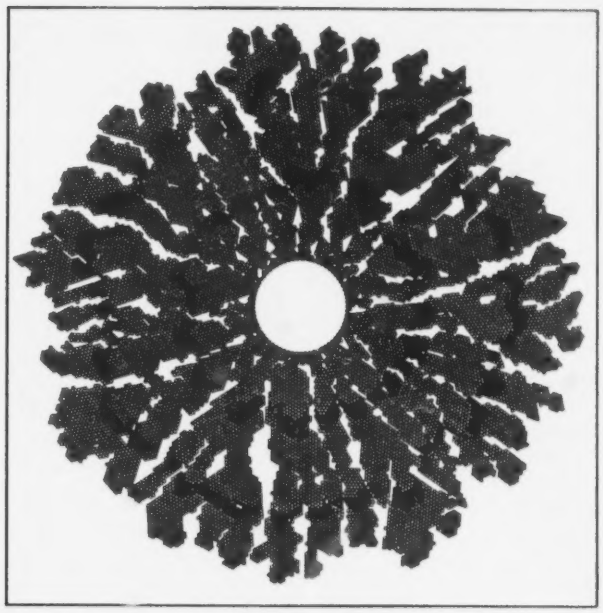

Figure A5.1. Simulation of giant hailstone. Layers of increased diffusion are shaded for emphasis.

Figure A5.2. Section of a giant hailstone. The scale is in centimeters.